U.PORTO
FEUP FACULDADE DE ENGENHARIA
UNIVERSIDADE DO PORTO

Dynamic Analysis of Structures with Viscoelastic Damping Treatments:

Complex Modulus Identification and Transient Response

Marta Cadete Maurício

Dissertation submitted to
Faculdade de Engenharia da Universidade do Porto
for the degree of:

Mestre em Engenharia Mecânica

Advisor:
Prof. José Dias Rodrigues
(Associate Professor)

Departamento de Engenharia Mecânica
Faculdade de Engenharia da Universidade do Porto

Porto, 2017

The work presented in this dissertation was performed at the
Laboratory of Vibrations of Mechanical Systems
Department of Mechanical Engineering
Faculty of Engineering
University of Porto
Porto, Portugal.

Marta Cadete Maurício
E-mail: em12045@fe.up.pt

Faculdade de Engenharia da Universidade do Porto
Departamento de Engenharia Mecânica
Laboratório de Vibrações de Sistemas Mecânicos
Rua Dr. Roberto Frias s/n, Sala M206
4200-465 Porto
Portugal

Resumo

O controlo de ruído e de vibração é um aspeto com crescente importância no desenvolvimento de estruturas e mecanismos. Na presente dissertação é efetuada a análise de estruturas com tratamentos viscoelásticos para controlo passivo de vibração. Para tal, são implementados dois métodos distintos de identificação das propriedades dinâmicas do material viscoelástico, bem como a análise da resposta transiente de estruturas com tratamentos viscoelásticos superficiais e integrados com configuração total e parcial.

É desenvolvido um procedimento experimental com o objetivo de determinar a função de resposta em frequência de vigas com tratamentos viscoelásticos integrados através de um teste de impacto. A dependência das propriedades dinâmicas destes materiais com a frequência é descrita pelo modelo de derivadas fracionárias de quatro parâmetros e o modelo espacial das vigas compósitas é estabelecido recorrendo ao método dos elementos finitos e a uma formulação *Layerwise*. A resposta em frequência é calculada de modo distinto nos dois métodos implementados: através do princípio de sobreposição modal e através de uma análise direta em frequência para um número discreto de frequências de controlo. Com recurso a técnicas de otimização, as funções de resposta em frequência geradas numericamente são ajustadas a funções obtidas experimentalmente e os parâmetros do modelo constitutivo de derivadas fracionárias são identificados.

Com vista à determinação da resposta transiente de estruturas compósitas com materiais viscoelásticos, garantindo a correta modelação das propriedades do material com a frequência, é desenvolvido um método que, através da transformada direta de Fourier da excitação, transforma a operação de convolução entre a excitação transiente e a função de resposta impulsiva no domínio do tempo numa multiplicação entre o espectro da excitação e a função de resposta em frequência do sistema e que, através da transformada inversa de Fourier, converte o espectro de resposta para o domínio do tempo. Com recurso às capacidades do método desenvolvido, é efetuado um estudo da resposta transiente para diferentes configurações de tratamentos viscoelásticos, bem como para diferentes solicitações aplicadas. Com base nas potencialidades da teoria *Layerwise* e no método dos elementos finitos, é estabelecido o modelo espacial para vigas multicamada com tratamentos viscoelásticos parciais e descontínuos. A eficiência deste tipo de tratamentos localizados é analisada em situação de regime dinâmico transiente e o seu efeito é caracterizado através de um indicador (de eficiência).

Palavras-Chave: controlo passivo de vibrações, amortecimento de vibrações, tratamento viscoelástico, modelo de derivadas fracionárias, resposta transiente, transformada de Fourier.

Abstract

Vibration control is a concern of growing importance in the dynamic design of structures and mechanisms. Taking the aforesaid into account, in this dissertation, the passive control of vibrations by means of a viscoelastic dissipative layer is addressed. Two methods are developed for the identification of the dynamic properties of the viscoelastic material and a transient response analysis is performed for structures with superficial and integrated damping treatments with partial and full configurations.

An experimental procedure is developed to determine the frequency response functions of beams with an integrated layer damping treatment by means of an impact test. The frequency dependence of the dynamic properties of the viscoelastic material is described using a fractional derivative model of four parameters and the spatial model of the composite beams is established using the finite element method and a *Layerwise* formulation. The response is calculated differently on both methods implemented: the first using the superposition of the natural modes of vibration and the second through a direct frequency analysis for a discrete number of control frequencies. Using optimisation techniques, the numerical frequency response functions are adjusted to experimentally determined functions and the fractional derivative model parameters are identified.

In view of determining the transient response of composite structures, preserving the frequency dependence of the dynamic properties, is developed a method that, using the Fourier's transform of the transient load, converts the time domain convolution between the transient load and the impulsive response function to a multiplication between the load spectrum and the frequency response function of the system, and then, using the inverse Fourier transform, converts the response spectrum to the time domain response. To demonstrate the effectiveness of such method, the transient response of beams with different damping treatments is determined and discussed as well as the application of distinct load configurations. Based on the potencial of the *Layerwise* theory and on the finite element method, the spatial model of multilayered beams with partial and discontinuous viscoelastic treatments is developed. The efficiency of these localised treatments is analysed in the time domain and their effect characterised with an indicator (of efficiency).

Keywords: passive vibration control, vibration damping, viscoelastic treatment, fractional derivative model, transient response, Fourier transform.

Acknowledgements

The development of the current work would not have been possible without the help of a number of people, to whom I would like to acknowledge.

First and foremost, I want to thank my advisor of this work, Professor José Dias Rodrigues, for his endless patience demonstrated throughout the entire semester. His constant readiness for any doubt clarification and encouragement allowed the development and conclusion of this thesis. I would also like to thank Professor João Amorim for the help and advice he has given me throughout the accomplishment of this work.

To all my friends, for all the tips and ideas we discussed but also for the five years of friendship and support and for providing me the needed form of escape from my studies.

Lastly, but most definitely not least, I would like to express my sincere gratitude to my family, not only for the unconditional support they always gave me but also for the tremendous effort and patience in order to provide me with an academic education.

Contents

List of Figures

List of Tables

Nomenclature

Subscripts

a	relative to the active degrees of freedom
c	control frequency counter
exp	relative to the experimentally measured function
$i,\ j$	general counter, relative to the degree of freedom
k	index of the composite material layer
num	relative to the numerically generated function
r	modal index

Superscripts

$()^B$	relative to bending component
$()^C$	relative to coupling component
$()^M$	relative to membrane component
$()^S$	relative to shear component
$()^e$	relative to the finite element

Acronyms

ADF	Anelastic Displacement Field
CLD	Constrained Layer Damping
DFA	Direct Frequency Analysis
DOF	Degree of Freedom
FE	Finite Element
FEM	Finite Element Method
FLD	Free Layer Damping
FRF	Frequency Response Function
GHM	Golla-Hughes-McTavish
ILD	Integrated Layer Damping
IMSE	Iterative Modal Strain Energy
LAC	Local Amplitude Criterion

MSE	Modal Strain Energy

Operators

$[\,]^H$	transpose complex conjugate of matrix
$[\,]^T$	transpose of matrix
D^α	fractional derivative of order α
$\mathfrak{F}(\bullet)$	Fourier transform
$\Im(\bullet)$	imaginary component
$\Re(\bullet)$	real component
$(\dot{\bullet})$	first order time derivative
$(\ddot{\bullet})$	second order time derivative
$\{\tilde{\bullet}\}$	vector modification
$[\tilde{\bullet}]$	matrix modification

Scalar Variables $(\bullet)$

a	thickness of host metallic beam [m]	$\in \mathbb{R}$
A	area [m^2]	$\in \mathbb{R}^2$
$\bar{A}(\mathrm{j}\omega)$	acceleration phasor	$\in \mathbb{C}$
b	width of the cross section of the beam [m]	$\in \mathbb{R}$
c	system's equivalent damping constant [Ns/m]	$\in \mathbb{R}$
e	thickness of the viscoelastic layer [m]	$\in \mathbb{R}$
E	Young's modulus [Pa]	$\in \mathbb{R}$
E'	extensional storage modulus [Pa]	$\in \mathbb{R}$
E''	extensional loss modulus [Pa]	$\in \mathbb{R}$
E^*	extensional complex modulus [Pa]	$\in \mathbb{C}$
E_0	static modulus of elasticity [Pa]	$\in \mathbb{R}$
E_∞	dynamic modulus for high frequencies [Pa]	$\in \mathbb{R}$
G	transverse elasticity modulus [Pa]	$\in \mathbb{R}$
G'	shear storage modulus [Pa]	$\in \mathbb{R}$
G''	shear loss modulus [Pa]	$\in \mathbb{R}$
G^*	shear complex modulus [Pa]	$\in \mathbb{C}$
h	thickness of restraining metallic layer [m]	$\in \mathbb{R}$
j	imaginary operator $\mathrm{j} = \sqrt{-1}$	$\in \mathbb{C}$
k, K	system's equivalent stiffness constant [N/m]	$\in \mathbb{R}$
l	length [m]	$\in \mathbb{R}$
l_t	covered length of the beam [m]	$\in \mathbb{R}$

m, M	mass of the system [kg]	$\in \mathbb{R}$
N	number of sampling points	$\in \mathbb{N}$
t_c	transient time duration [s]	$\in \mathbb{R}$
T	temperature [°C]	$\in \mathbb{R}$
T_n	natural period [s]	$\in \mathbb{N}$
u	displacement in the direction x	$\in \mathbb{R}$
$\bar{V}(\mathrm{j}\omega)$	velocity phasor	$\in \mathbb{C}$
w	displacement in the direction z	$\in \mathbb{R}$
$\bar{X}(\mathrm{j}\omega)$	displacement phasor	$\in \mathbb{C}$
α	fractional derivative order $0 < \alpha < 1$	$\in \mathbb{R}$
β^y	rotation around y axis [rad]	$\in \mathbb{R}$
δ	lag angle [rad]	$\in \mathbb{R}$
δ_f	logarithmic decrement in the free response bandwidth	$\in \mathbb{R}$
δ_l	logarithmic decrement in the transient load bandwidth	$\in \mathbb{R}$
η	loss factor	$\in \mathbb{R}$
ν	Poisson's ratio	$\in \mathbb{R}$
ν^*	complex Poisson's ratio	$\in \mathbb{C}$
ξ	damping ratio	$\in \mathbb{R}$
Π^k	kinetic energy [J]	$\in \mathbb{R}$
Π^p	strain energy [J]	$\in \mathbb{R}$
ρ	volumetric weight [kg/m^3]	$\in \mathbb{R}$
τ	relaxation time [s]	$\in \mathbb{R}$
ϕ	phase of the response [rad]	$\in \mathbb{R}$
Ω	volume domain [m^3]	$\in \mathbb{R}^3$
ω	frequency [rad/s]	$\in \mathbb{R}$
ω_d	damped natural frequency [rad/s]	$\in \mathbb{R}$
ω_n	undamped natural frequency [rad/s]	$\in \mathbb{R}$

Vector Variables $\{\,\}$

$\{A(\omega)\}$	accelerance function	$\in \mathbb{C}$
$\{\mathrm{d}\}$	generalised displacement field	$\in \mathbb{R}$
$\{f(t)\}$	dynamic load vector in the time domain	$\in \mathbb{R}$
$\{F\}$	dynamic load vector	$\in \mathbb{C}$
$\{p(t)\}$	dynamic response vector using principal coordinates	$\in \mathbb{R}$
$\{P(\omega)\}$	response phasor using principal coordinates	$\in \mathbb{C}$

$\{q\}$	distributed load vector	$\in \mathbb{R}$
$\{\mathrm{u}\}$	displacement field	$\in \mathbb{R}$
$\{x(t)\}$	dynamic response vector	$\in \mathbb{R}$
$\{\bar{X}(\omega)\}$	response phasor vector	$\in \mathbb{C}$
$\{\alpha(\omega)\}$	receptance function	$\in \mathbb{C}$
$\{\varepsilon\}, \varepsilon$	strain field	$\in \mathbb{R}$
$\{\sigma(t)\}, \sigma$	stress field	$\in \mathbb{R}$
$\{\phi\}$	eigenvector	$\in \mathbb{C}$
$\{Y(\omega)\}$	mobility function	$\in \mathbb{C}$

Matrix Variables [ ]

$[\mathcal{B}]$	deformation matrix	$\in \mathbb{R}$
$[B]$	finite element deformation matrix	$\in \mathbb{R}$
$[D]$	elasticity matrix	$\in \mathbb{R}$
$[\mathcal{D}]$	material's constitutive law	$\in \mathbb{R}$
$[G]$	transverse elasticity matrix	$\in \mathbb{R}$
$[I]$	identity matrix	$\in \mathbb{R}$
$[\mathcal{J}]$	inertia matrix	$\in \mathbb{R}$
$[K]$	stiffness matrix	$\in \mathbb{R}$
$[K^*]$	complex stiffness matrix	$\in \mathbb{C}$
$[\mathcal{L}]$	differential operator	$\in \mathbb{R}$
$[M]$	mass matrix	$\in \mathbb{R}$
$[N]$	shape function matrix	$\in \mathbb{R}$
$[\Phi]$	eigenvector matrix	$\in \mathbb{C}$

Referential

x, y, z	cartesian coordinate referential
ξ, η, ζ	natural coordinate referential

Chapter 1

Introduction

1.1 Background

The evolution of structural engineering has resulted on the removal of the inherent damping properties of structures. For instance, massive structures built with rigid materials have been gradually replaced by lighter and more flexible structures much more efficient than those used in the past. However, these structures are sometimes prone to fatigue damaging when submitted to cyclic loading. In fact, if the damping abilities of the structure are not capable of dissipating energy of the induced vibration, it becomes noisier and considerably less safe (Jones, 2001).

Vibration control has become a subject of the utmost importance in machine and structure design. For that, resonant frequencies of structures, the corresponding modes of vibration and the response to expected excitation forces must be calculated for a successful project design. Vibration problems can occur in a phase where changing the system's internal mass or even the stiffness is impossible. At this point, additional damping treatments or damping devices must be added in order to efficiently control the steady state resonant response of the structure (Moreira, 2004).

Damping can be placed in one of three categories: active, passive or hybrid damping (Lopes, 2008). The first one consists of adding to the structure sensors and actuators capable of measuring the response of the system at each period of time and electronically cancel the disturbance (Jones, 2001). Usually, these devices are built with piezoelectric materials and are glued to the structure.

Passive damping is the major mean of suppressing vibration of structures. It can be broken into two categories: inherent and designed-in damping. Inherent damping is the one that exists in a structure due to the friction of joints, material damping or even rubbing of cables. This type of damping is very small when compared to other sources of damping. Designed-in damping is, as the name would suggest, the addition of damping devices or materials to the structure by design (Johnson, 1995). The most common passive damping devices in engineering are the viscous damping mechanisms, as their mathematical treatment is quite simple and analytical solutions to the equations of motion can easily be obtained. Nonetheless, the application of viscoelastic materials in the form of damping treatments has been one of the preferred solutions of designers for vibration and noise control, being this the focus of the current thesis.

Lastly, hybrid vibration control is essentially a combination of the remaining types of damping: it combines the piezoelectric actuators that perform the active control with the damping materials which induce the passive control of vibrations.

Viscoelastic damping is a property exhibited by a variety of polymers, from synthetic rubbers to adhesives, which allows to add to the structure or machine different damping levels depending on the material selected or even on the configuration of such treatment.

For adequately designing viscoelastic damping treatments, a complete knowledge of the viscoelastic behaviour is essential. However, characterising the viscoelastic behaviour is not an easy endeavour as its properties depend on numerous factors, such as frequency or temperature. Therefore, concerning an effective application of such materials, one has two options: access manufacturer's data or even conduct their own experimental procedure to determine the dynamic properties of the material. The data provided by the manufacturer is, normally, presented in the form of a reduced frequency nomogram. Although, occasionally, is not easy to have access to it or rather the experimental conditions in which they were obtained are not rigorously described. Thereby, opting to determine those properties is the preferred methodology.

1.1.1 Damping Treatments

Even though viscoelastic materials have great energy dissipation in the form of heat when submitted to cyclic deformation, they are not very efficient as structural materials due to their low resistance and high mass (Moreira, 2004). As such, they are added to the structure in the form of viscoelastic treatments, whether surface mounted or embedded ones. The added damping layer dissipates energy as a result of the strain field that it undergoes. The strain field varies over the depth and surface of the structure and can be a result of bending or membrane loads, which leads to an extensional strain field, or even a result of shear loads, which conducts to a shear strain field (Vasques and Cardoso, 2011).

In order to induce a certain type of deformation of the viscoelastic material, the damping treatments can be designed in different configurations: free or unconstrained layer damping (FLD), constrained layer damping (CLD) or integrated layer damping (ILD) (Lopes, 2008; Moreira, 2004).

Free Layer Damping

In this configuration the material is applied in the outside surfaces of the structure or machine as illustrated in figure 1.1.

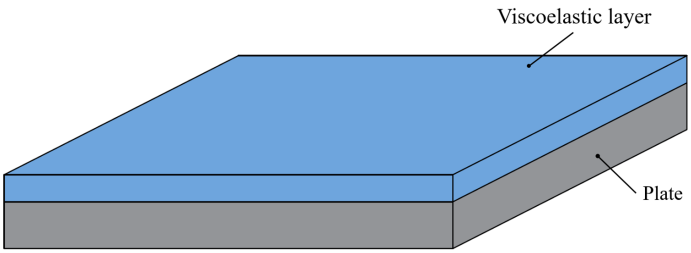

Figure 1.1: Unconstrained layer damping treatment.

The energy is dissipated mostly in the form of heat generated by the tension-compression deformation of the material when the structure is deformed in bending. The amount of damping introduced in the system is directly proportional to the distance between the viscoelastic layer and the neutral axis of the structure, which means that an increase in thickness of viscoelastic material leads to a higher damping level (Vasques and Cardoso, 2011).

However, in order to introduce relevant levels of damping in the structure, thick viscoelastic layers are necessary, which change greatly the system's mass and stiffness. For that reason, this is not the most efficient viscoelastic treatment. However, it continues to be widely used because of its simplicity, both in terms of numerical simulation and in application (Vasques and Cardoso, 2011).

The damping performance achieved using this configuration, as stated by Rao (2003), is independent of the mode of vibration of the structure for full coverage treatments. However, it is possible to optimise for a single or a limited number of modes of vibration using a partial FLD treatment.

Constrained Layer Damping

The constrained layer damping treatment is a result of the application of an elastic constraining layer on top of the viscoelastic material and the host structure - figure 1.2. The stiffness of the added elastic material must be greater than that of the viscoelastic material so that the energy dissipation occurs as a result of the deformation of the viscoelastic material.

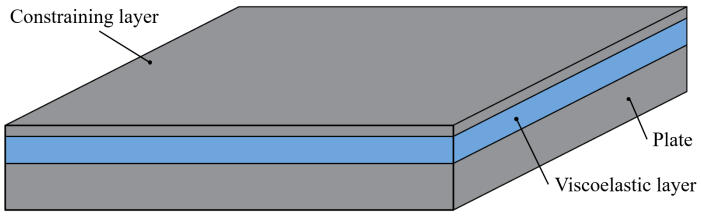

Figure 1.2: Constrained damping layer treatment.

The viscoelastic material is mainly deformed in shear. The maximum shear deformation normally occurs in the neutral plane and is zero at the outside surfaces. As such, the viscoelastic material should be positioned as close to the neutral plane as possible in order to increase the amount of damping added to the structure.

This form of damping treatment usually leads to the application of thinner damping layers when compared to the ones necessary in unconstrained damping treatments, which results in a smaller modification of the mass of the system (Vasques and Cardoso, 2011).

Integrated Layer Damping

The most efficient damping treatment is where the viscoelastic material is integrated in the core of a sandwich structure - figure 1.3.

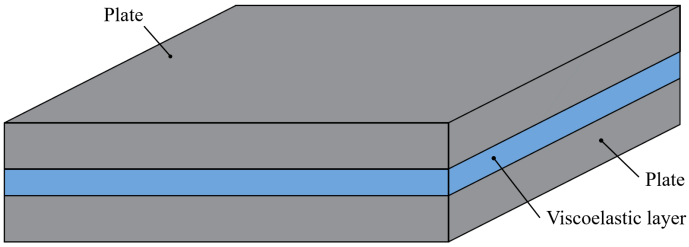

Figure 1.3: Integrated damping layer treatment.

The material is subjected to a shear deformation and its position over the neutral plane of the structure allows the addition of great damping levels with relatively low thicknesses (Vasques and Cardoso, 2011).

This type of treatment, as opposed to the ones previously referred, is not applied as a corrective treatment. Since it is positioned in the core of the structure, it needs to be included

in the project of the structure or machine (Moreira, 2004).

1.2 Modelling viscoelastic treatments

As structures or machines get more complex, analytical solutions cannot always be found and the finite element method (FEM) is the preferred approach to solve static and dynamic problems concerning such structures. For the correct application of the FEM to structures with viscoelastic treatments, three subjects are of concern: the selection of an appropriate spatial model of the composite structure, the selection of a constitutive model of the viscoelastic material that accurately describes the variation of the material's properties with frequency and finally, the selection of an approach to solve the finite element problem.

The spatial modelling of structures with viscoelastic treatments can be executed in copious ways, keeping in mind the significant shear deformation of the viscoelastic material. The approach utilised can be based on combined assemblies of standard finite elements or even the promising discrete layer models, which are the ones of most relevance in the present work (Moreira, 2004; Vasques and Cardoso, 2011).

The constitutive behaviour represents itself an obstacle in modelling viscoelastic treatments, given the peculiar properties of viscoelastic materials, and its dependence with numerous factors. Throughout the years, several models have been proposed: from a combination of springs and dashpots, which are referred to as *classical models* to more complex models such as *Anelastic Displacement Fields* (ADF) model, which describes the frequency dependence through additional anelastic variables, or *Golla-Hughes-McTavish* (GHM) model, which represents the characteristic material function in terms of a series of *mini-oscillator* terms. In the current work the formulation used is the fractional derivative model using four parameters. This model accurately describes the variation of frequency dependent properties of the material with one derivative term and its manipulation is fairly simple when dealt with in the frequency domain (Vasques et al., 2010a).

Lastly, in order to solve the numerical finite element problem, an adequate solution method must be chosen and implemented. As reference, one can implement in the FE code one of several solution methods, such as the Direct Frequency Analysis (DFA) method or even an Iterative Modal Strain Energy (IMSE) method.

1.3 Motivations of the thesis

The use of viscoelastic treatments as an external source of damping has grown recently in a wide range of industries. In the automotive industry, a few examples of the introduction of viscoelastic treatments to reduce sound and vibration are the use of "laminate steels" in the body structure of the vehicle, which consist of panels with metallic outer skins sandwiched by a thin viscoelastic core material, or even the addition of polyvinyl laminated glass on the windows, to reduce road and wind noise. The commercial aircraft industries also recur to local damping treatments in the fuselage using add-on type damping to reduce the vibration amplitude. Since the weight is one of the prior concerns, CLD treatments are designed to minimise the weight increase and possess the maximum efficiency even when the bending deformation of the structure is minimal (Rao, 2003).

Naturally, expectations regarding damping materials have also been expanding as the sound quality and weight reduction has become superior. As such, it is required a complete knowledge of the material's behaviour in the most various situations. Thus, a modest attempt to develop an identification method in order to determine the dynamic properties of a viscoelastic as a function of frequency is performed.

Additionally to the correct application of the material, the development of lightweight, innovative and efficient damping treatment configurations has been of the maximum importance when vibration or sound control is of interest. As one can anticipate, the correct design of such treatments requires an adequate prediction of the material's dynamic properties, using reliable constitutive models and also suitable finite element models that can accurately describe and determine the composite structure's response to different types of load application. Bearing that in mind, a prediction of the transient response of structures with viscoelastic damping treatments using a Fourier transform and the evaluation of the efficiency of such treatments in the time domain are proposed in the current work.

1.4 Objective of the thesis

The main purpose of the current work is to identify the dynamic properties of a viscoelastic material using an indirect curve-fitting process and then use the identified properties to analyse the transient response of structures with viscoelastic damping treatments. To achieve these goals, several other objectives must be fulfilled, as the ones listed bellow:

- Understand the fundamental principles of viscoelastic phenomena, namely the variation of its dynamic properties with frequency and temperature;
- Understand the concept of viscoelastic constitutive modelling, in particular, the use of fractional derivative models in the frequency domain to describe the variation of the material's properties with frequency;
- Develop an experimental set-up to determine Frequency Response Functions (FRF) of clamped-free beams with integrated damping treatments;
- Develop and implement an algorithm in `Matlab`® based on a finite element model of composite beams with viscoelastic materials for the identification of the fractional derivative model parameters of the viscoelastic material through a curve-fitting process of numerical FRFs to experimental FRFs;
- Understand the basis of frequency analysis, particularly, the formulation and application of the Fourier transform;
- Develop and implement a finite element method (FEM) based procedure to determine the transient response of a composite structure with a viscoelastic damping treatment using a frequency domain analysis and the direct/inverse discrete Fourier transform;
- Generalise a spatial finite element (FE) formulation based on a *Layerwise* theory in order to build the spatial model of multilayered beams with partial and discontinuous damping layer treatments;
- Evaluate the efficiency of partial and discontinuous viscoelastic damping treatments based on the time transient response analysis.

1.5 Organisation of the thesis

The thesis begins with an introductory chapter, Chapter 1, where the concept of vibration control using viscoelastic damping treatments is addressed as well as the topic of viscoelastic modelling for FEM application. Also, a brief summary of the contents of the thesis is presented.

In Chapter 2, the characterisation of the viscoelastic material is performed and the effects of frequency and temperature on the material's properties are acknowledged. Two models of experimental procedures for the determination of the dynamic properties of the viscoelastic material are explained as well as the most common data representation methods. The concept of viscoelastic constitutive modelling is also addressed. The fractional derivative model using four parameters is detailed as well as a brief description of other models.

The spatial modelling of viscoelastic treatments is developed in Chapter 3. The *Layerwise* beam formulation using *Timoshenko* assumptions for each layer is explained including the deduction of the displacement, strain and stress fields. The variational formulation is obtained using Hamilton's principle along with the definition of kinetic energy, strain energy and virtual work of distributed loads. It is also described the formulation of the 2-node isoparametric element.

All aspects relative to the experimental procedure are detailed in Chapter 4. The experimental samples are exposed as well as the experimental set-up adopted and a summary of the results attained.

In Chapter 5, the two-step identification method implemented is described, including the finite element model and the algorithm developed. This chapter also includes a schematic diagram of such method, a brief description of the minimisation functions used and a description of the criterion chosen to quantitatively compare the results reached.

The results obtained from the application of the two-step identification method on the composite and bare beams tested are shown in Chapter 6, that includes the fractional derivative model parameters and the resulting storage modulus and loss factor of the viscoelastic material. It is also tested in this chapter, the behaviour of the present method with different sets of initial parameters and different number of modes of vibration considered to generate the numerical Frequency Response Function.

Chapter 7 includes the description of a different identification method, the direct-frequency response identification method. This description includes the finite element model used, the algorithm implemented and the definition of control frequencies where the minimisation function is evaluated.

In Chapter 8, the previous identification method is validated. The results attained with the application of such method on the composite and bare beams are shown as well as a test on the performance of the method using a different number of control frequencies and a different number of modes of vibration.

In Chapter 9, the transient response of composite structures with viscoelastic materials is addressed. The concepts of frequency analysis using the Fourier transform are detailed and the implemented method is described. The methodology is then validated using a viscously damped 1 degree of freedom (DOF) system and applied to composite structures with different damping treatment configurations.

The analysis of the developed work is performed in Chapter 10, and a few conclusions are drawn. Additionally, various suggestions are given in order to continue the work hereby developed.

Chapter 2

Viscoelastic Materials

2.1 Introduction

Viscoelastic materials are commonly used in passive damping mechanisms because they exhibit great energy dissipation in the form of heat. This energy dissipation is a result of the interaction of its long molecular chains when submitted to continuous deformation.

Normally, the viscoelastic material is applied as a distributed surface mounted or embedded treatment and provides the structure with additional damping necessary for noise control. The design and analysis of such structures represents quite a difficult task due to the dependence of the materials' damping properties on external factors as frequency of excitation and temperature.

Thus, it is the purpose of this chapter to study the mechanical behaviour of viscoelastic materials as well as the experimental determination and representation of its mechanical properties in order to achieve maximum efficiency in vibration control applications.

2.2 Viscoelastic Material Characterisation

Materials whose mechanical response to external disturbances combines the characteristics of both elastic solids and viscous fluids are called viscoelastic (Gutierrez-Lemini, 2013). Most viscoelastic materials with great interest in engineering are polymeric or polymeric based materials. These are composed of long intertwined and cross-linked molecular chains that when submitted to deformation develop properties as stiffness and energy dissipation (Amorim, 2013; Jones, 2001).

Even though one can assume that these materials are homogeneous, which means the properties are constant throughout the entire volume of the sample, and isotropic, that means the properties are the same whichever direction is considered, its mechanical properties are highly dependent on numerous factors. Some of these are the time and temperature at which the response is measured, the amplitude and type of excitation applied and even the environmental conditions such as the exposure to hydrocarbon fluids or humidity. However, the application of viscoelastic materials often implies some protection from environmental conditions and a linear viscoelastic behaviour can be assumed. The concept of linear viscoelasticity implies that the increase in the strain amplitude of a determined quantity will lead to an increase in the stress magnitude by the same factor, which is a reasonable approximation within limits (Jones, 2001).

2.2.1 Material Response to Cyclic Stress Loading

The imposition of a one dimension harmonic load generates a stress field characterised by the following equation:

$$\sigma(t) = \sigma_0 \sin(\omega t). \tag{2.1}$$

The resulting strain field is also harmonic of the same frequency as the stress field but lags behind by an angle, δ, which is directly related to the damping characteristics of the material:

$$\varepsilon(t) = \varepsilon_0 \sin(\omega t - \delta). \tag{2.2}$$

As proven in the equation stated above, the viscoelastic behaviour is placed between the behaviour of an elastic solid, being the latter characterised by a harmonic and synchronous strain field that is in phase with the stress field, and the behaviour of a viscous fluid, whose strain field is in quadrature with the stress field.

The plot of measured stress versus measured strain is elliptical and is called the hysteresis loop of the viscoelastic material - figure 2.1. The slope of the major axis is a measure of the stiffness of the material, the aspect ratio is a measure of damping and the area defined by the curve a measure of the energy dissipated (Moreira, 2004).

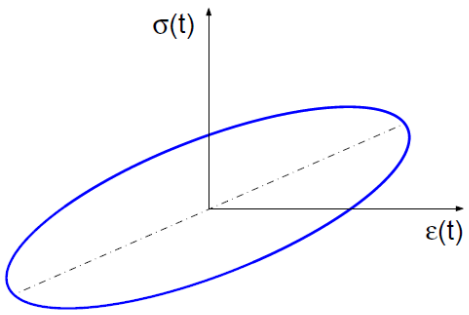

Figure 2.1: Hysteresis loop of a viscoelastic material (Moreira, 2004).

2.2.2 Complex Modulus Model

In the previous chapter, the relation between stress and strain in a viscoelastic material is expressed in terms of trigonometric quantities. However, it becomes practical to address this problem using complex numbers. As such, it is common to describe the stress and strain fields in terms of a complex exponential function defined as:

$$\sigma = \sigma_0 \mathrm{e}^{\mathrm{j}\omega t} \tag{2.3}$$

$$\varepsilon = \varepsilon_0 \mathrm{e}^{\mathrm{j}\omega t - \delta} \tag{2.4}$$

The relation between the complex stress and strain fields leads to the definition of the complex extensional modulus, E^*:

$$\sigma(\mathrm{j}\omega) = E^*(\mathrm{j}\omega)\varepsilon(\mathrm{j}\omega) \Leftrightarrow E^*(\mathrm{j}\omega) = \frac{\sigma(\mathrm{j}\omega)}{\varepsilon(\mathrm{j}\omega)}, \tag{2.5}$$

The complex modulus can be expressed in the form of a sum of its real and imaginary parts:

$$E^*(\mathrm{j}\omega) = E'(\omega) + \mathrm{j}E''(\omega), \tag{2.6}$$

where $E'(\omega)$ is the extensional storage modulus, which accounts for the recoverable energy, and $E''(\omega)$ is the loss modulus which represents the energy dissipation effects. The loss factor of a viscoelastic material is defined as:

$$\eta(\omega) = \frac{E''(\omega)}{E'(\omega)}. \tag{2.7}$$

The loss factor definition allows to rewrite equation (2.6) in the following manner:

$$E^*(\mathrm{j}\omega) = E'[1 + \mathrm{j}\eta(\omega)]. \tag{2.8}$$

The equations stated above can be obtained similarly in terms of shear quantities, leading to the definition of the complex shear modulus, $G^*(\mathrm{j}\omega)$. For a linear, homogeneous and isotropic material, the complex Poisson's ratio, $\nu^*(\mathrm{j}\omega)$, establishes the relation between the extensional and shear complex modulus:

$$E^*(\mathrm{j}\omega) = 2G^*(\mathrm{j}\omega)[1 + \nu^*(\mathrm{j}\omega)]. \tag{2.9}$$

Due to the little frequency dependence of the Poisson's ratio, one can consider its value a real and constant quantity. This simplification leads to identical values of the extensional and shear loss factors (Moreira et al., 2010; Vasques et al., 2010a).

2.2.3 Effects of Temperature and Frequency on Complex Modulus

The Effects of Temperature

The variation of the dynamic properties of viscoelastic polymers, represented by the storage moduli $G'(\omega)$ (or $E'(\omega)$) and the loss factor $\eta(\omega)$, is illustrated in figure 2.2.

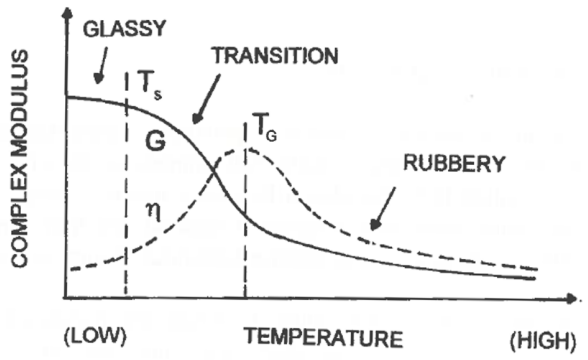

Figure 2.2: Effect of temperature on complex shear modulus behaviour (Jones, 2001).

The behaviour of viscoelastic materials is divided into three different zones as the temperature increases, namely the glassy region, the transition region and the rubbery plateau. Some materials can even evidence a fourth zone named the viscous flow region.

In the first region, the material is characterised by a high modulus and a very low loss factor, which results in deficient damping properties. As the temperature increases, the modulus begins to fall rapidly and the loss factor reveals the opposite behaviour. The transition region encompasses a low range of temperatures and the temperature in the middle of this region is called the *Glass Transition Temperature* (Tg). For temperatures close to the Tg, the material is flexible and the modulus and the loss factor show great variation with the slightest variation in temperature. The maximum value of the loss factor occurs at the *Glass Transition Temperature*.

The rubbery plateau, as the name suggests, is a region where the both storage modulus and loss factor show little variation and the material behaves as a rubbery elastic solid with low

modulus. Several polymers show a fourth region, where the molecular segments slid past one another and the material exhibits a viscous behaviour (Gutierrez-Lemini, 2013).

When vibration control is of interest, the material is required to have a high loss factor to insert good damping properties in the structure. As such, the transition zone defines the more usual range of application of such materials in vibration control (Jones, 2001).

The Frequency Effects

For a thermo-rheologically simple viscoelastic material, the effect of frequency in the complex properties is the inverse of the effect of temperature, but at a much lower rate. The effect of a variation of 100 degrees, which is usually the difference in temperature between the glassy and the transition regions, may correspond to a range of frequency of many decades of magnitude, often ten or more (Jones, 2001).

The effect of frequency in the storage modulus and the loss factor is evidenced in figure 2.3.

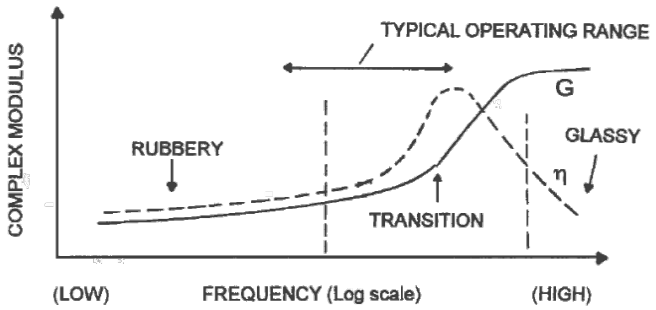

Figure 2.3: Effect of frequency on complex shear modulus behaviour (Jones, 2001).

2.3 Complex Modulus Data Analysis and Representation

The result of the measurement process of the complex modulus properties is often constituted by a set of values of temperature, frequency, storage modulus ($G'(\omega)$ or $E'(\omega)$) and loss factor, $\eta(\omega)$. In this section, the analysis of such data, using the frequency-temperature superposition principle is addressed and its graphical representation is shown.

2.3.1 Frequency-Temperature Superposition Principle

This equivalence between temperature and frequency is designated the frequency-temperature superposition principle, which states that a complex modulus modification induced by a frequency change can be identical do the one produced by an inverse modification in temperature (Vasques et al., 2010a). The application of this principle is quite convenient as it allows to infer complex modulus data using a set of experimental values determined for particular cases of frequency and temperature (Moreira et al., 2010).

Thereby, the complex modulus values at one chosen frequency, f_1, and one chosen temperature, T_1, are equal to those determined at a frequency f_2 and a temperature T_2. Using as an example the complex shear modulus:

$$G^*(f_1, T_1) = G^*(f_2, T_2). \tag{2.10}$$

Since frequency and temperature are related, equation (2.10) can be written in terms of a general parameter called reduced frequency, which is defined as:

$$f_R = f_1\alpha(T_1) = f_2\alpha(T_2), \tag{2.11}$$

$$G^*(f_1\alpha(T_1)) = G^*(f_2\alpha(T_2)), \tag{2.12}$$

where $\alpha(T)$ represents the shift factor which is a function of temperature only. Usually, its determination is done using a logarithmic representation of the storage modulus, or the loss factor, by sliding the different sets of data collected at different temperatures in order to create a single curve (Fernandes, 2013; Jones, 2001; Moreira et al., 2010). The outcome of this process is the value of the shift factor for a given temperature. From those discrete values of the shift factor, it is possible to obtain mathematical models that describe the variation of the shift factor in a broad range of temperatures. The models commonly used and presented in this work are the *Williams-Landel-Ferry* equation, WLF, and the *Arrhenius* equation.

2.3.2 Shift Factor Relationships

William-Landel-Ferry Equation

The WLF equation represents a non-linear relationship between the shift factor and temperature and is expressed as following:

$$\log[\alpha(T)] = -C_1\frac{T - T_0}{B_1 + T - T_0}, \tag{2.13}$$

where C_1 and B_1 are constants determined recurring to the experimental data and T_0 is the reference temperature. The reference temperature can be chosen arbitrarily bearing in mind that its value has an influence on the other parameters of the WLF equation (Jones, 2001).

Arrhenius Equation

A simpler model is the Arrhenius equation, which assumes a linear relashionship between the $\log(\alpha(T)$ and $\frac{1}{T}$:

$$\log[\alpha(T)] = -T_A\left(\frac{1}{T} - \frac{1}{T_0}\right), \tag{2.14}$$

with T_A representing the slope of the plot of $\log(\alpha(T))$ as a function of $\frac{1}{T}$, and T_0 a chosen reference temperature.

The differences between the results from both models addressed is more noticeable in the extreme values of the experimental temperature range. In most cases, the linear model is enough to obtain reliable results, and only occasionally the available data demands a more complicated model (Jones, 2001).

2.3.3 The Temperature-Frequency Nomogram

The most common technique of representing the storage modulus and the loss factor as a function of both frequency and temperature is the nomogram of the viscoelastic material. As an example, the nomogram of the viscoelastic material 3M ISD110 is represented in figure 2.4.

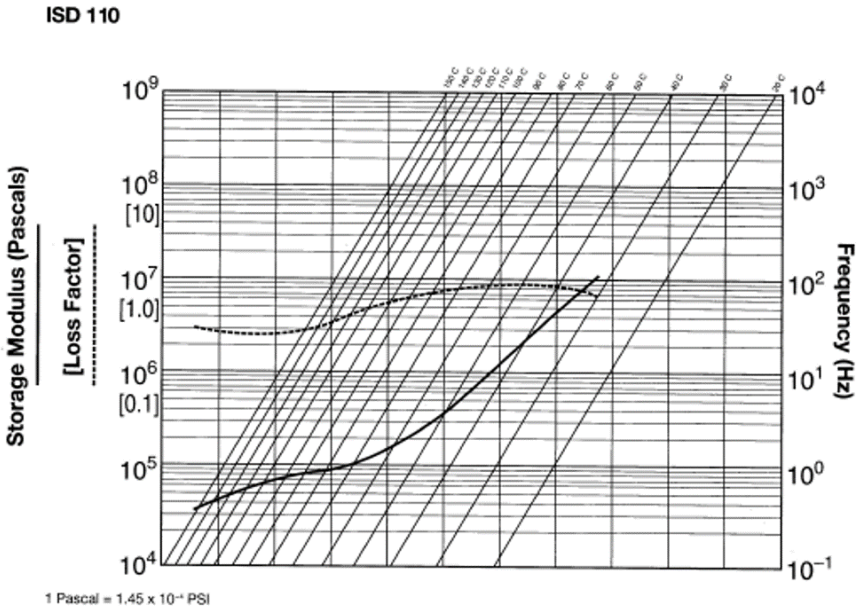

Figure 2.4: Temperature-Frequency Nomogram of ISD110 (Moreira, 2004).

The determination of the dynamic properties from such diagram implies the execution of a few steps. Firstly, one identifies a point defined by the intersection between a value of frequency from the right side axis and a value of temperature from one of the diagonal isotherms. The intersection of the vertical line that contains such point and the loss factor or storage modulus curves returns the values of those properties. These values can then be read in the left side axis.

2.4 Experimental Determination of the Complex Modulus

The determination of the frequency dependent properties of viscoelastic materials represents quite a difficult task and requires cumbersome methods. Even though theoretically, the method may be reliable, in practice is difficult to reproduce an experimental apparatus identical to the analytical model developed. For example, the introduction of force and displacement transducers on the system leads to the addition of mass that needs to be considered in the analytical model. Additionally, the isolation of the system from exterior vibrations is difficult to conceive, and the construction of rigid bases is not always possible. Furthermore, the assumed conditions of mechanical and thermal equilibrium of the viscoelastic material are not easy to preserve for long periods of time, which hinders the acquisition of reliable data (Jones, 2001).

Several methods for measuring the complex moduli of viscoelastic materials have been proposed. They can be roughly divided into two groups: direct and indirect methods. In the direct methods, the properties of the viscoelastic material are determined using bare viscoelastic samples that represent the damping element of the system. While in the indirect methods, the properties of the viscoelastic material are identified comparing the dynamic measurements of beams with and without the application of viscoelastic layers (Vasques et al., 2010b).

In the present work two methods will be explained: the vibrating beam techniques, which constitutes the basis of the experimental set-up used in the current work, and a discrete one degree of freedom method.

2.4.1 Vibrating Beam Techniques

Vibrating beam techniques are the preferred methods for the determination of the complex modulus of viscoelastic materials by the sample's manufacturers.

For the case of a non-self-supporting viscoelastic material, the test specimen consists of a base metallic beam on which is applied a non-constrained or constrained viscoelastic treatment. Whereas for the case of a self-supporting viscoelastic material, the test procedure does not require a base metallic beam and a single uniform viscoelastic beam can be used. The material used for the base beams should be a metal with low structural damping, as aluminium or steel to guarantee that the damping introduced in the composite structure is merely caused by the viscoelastic material.

For the experimental procedure, the beam is clamped at its root end and free at the opposite end. A force transducer applies a prescribed cyclic load and a response transducer measures the response of the beam. The viscoelastic properties are then inferred from the comparison between the natural frequencies and modal loss factors of the base beam and the composite beam. Usually, only the lowest three natural frequencies are required in order to fully characterise the viscoelastic material. Introducing the experimental apparatus in a thermal chamber can lead to the determination of the complex modulus at several temperatures and using the temperature-frequency superposition principle the properties for a wide range of frequencies can be deduced.

Although several changes and innovations have been proposed to this methodology, as the ones suggested by Liao and Wells (2008) or by Wojtowicki et al. (2004), it is extensively described in *ASTM E756-05: Measuring Vibration-Damping Properties of Materials* (ASTM, 2010) where the directives for test specimen preparation, experimental procedure concerns and latter calculations to obtain the numerical values are referred.

The method can be performed in different sample configurations depending on the type of damping material to be tested and on the desired damping properties (shear or extensional properties). These different configurations will be developed in the present chapter.

Oberst Beam

The modified *Oberst Beam* is a metallic beam with an unconstrained viscoelastic layer as illustrated in figure 2.5. The energy is dissipated through cyclic deformation mainly in tension-compression.

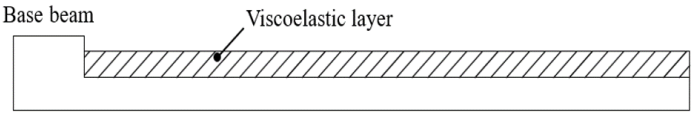

Figure 2.5: *Oberst Beam.*

At first, the natural frequencies and loss factors of the base metallic beam are obtained and then the viscoelastic layer is applied. The damping material is fixed with the introduction of a thin layer of a structural adhesive. The selected adhesive should not interfere with the properties of the damping layer by creating a new viscoelastic layer which compromises the characterisation of the sample material. The natural frequencies and modal loss factors of the composite beam are experimentally identified and, with the application of the mathematical relations described in ASTM (2010) the extensional complex modulus is determined.

Van Oort Beam

In the *Van Oort Beam* configuration, a viscoelastic layer is placed on each side of the metallic beam, resulting in a symmetric sample - figure 2.6.

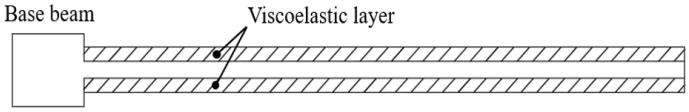

Figure 2.6: *Van Oort Beam.*

This configuration overcomes the problems of undesired bending deformation induced by thermal dilation present for the *Oberst Beam* configuration. It also places the neutral bending axis in the center of the composite beam which leads to a great simplification of the equations used to determine the complex extensional properties (Moreira, 2004).

Sandwich Beam

The *Sandwich Beam* configuration allows the determination of the shear complex modulus of non-self-supporting damping materials. This configuration is constituted of a viscoelastic damping layer placed in the middle of two metallic beams, as illustrated in figure 2.7.

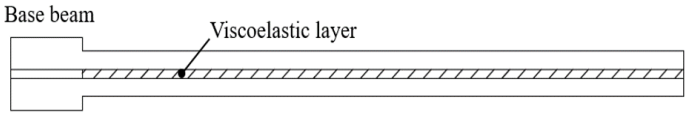

Figure 2.7: *Sandwich Beam.*

It is very important that both metallic beams are dynamically similar, that is, the natural frequencies of the undamped beams must be coincident in order to validate the results obtained for the viscoelastic layer.

The composite beam is symmetric which leads to a great simplification of the equations used to determine the complex quantities (Moreira, 2004).

2.4.2 One Degree of Freedom Model

The determination of the frequency dependent properties of viscoelastic damping materials can also be performed using discrete models. In the present work, the discrete system with one degree of freedom (DOF) will be explained. This model is characterised by its mathematical simplicity but, on the other hand, by its inherent difficulty of experimental execution (Moreira, 2004).

The configuration of the system is illustrated in figure 2.8, where the stiffness element is the viscoelastic layer and a rigid block of mass M represents the concentrated mass of the system. It can be designed so that the viscoelastic material is deformed in shear (figure 2.8a), when the shear complex modulus is needed, or in tension-compression (figure 2.8b), when extensional complex modulus is required.

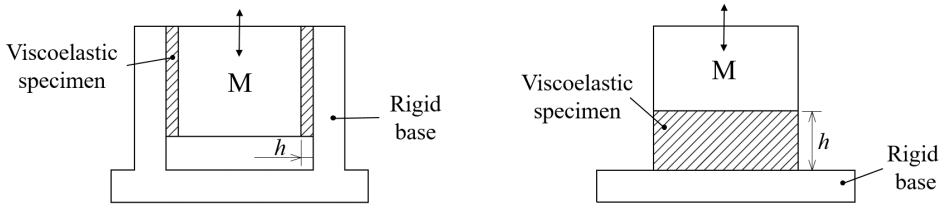

(a) Shear test configuration. (b) Extension test configuration.

Figure 2.8: Discrete one DOF system configuration (Adapted from (Moreira, 2004)).

The complex stiffness of the system is calculated as a function of the geometric parameters of the viscoelastic layer and of the complex modulus of the material. If the viscoelastic material is deformed in shear, the equivalent complex stiffness is calculated using equation (2.15) whereas if it is deformed in tension or compression one must rely on equation (2.16), which are written as follows:

$$K^* = G^* \frac{A_s}{h}, \tag{2.15}$$

where G^* is the complex shear modulus, A_s the transversal section area in shear and h the sample's thickness.

$$K^* = E^* \frac{A_e}{h}, \tag{2.16}$$

where E^* is the complex extensional modulus, A_e the transversal section area and h the sample's thickness.

The characterisation of the viscoelastic material is obtained by identifying the system's complex stiffness through the response function obtained with the application of a harmonic excitation, $f(\mathrm{t})$. A schematic diagram of the system is illustrated in figure 2.9.

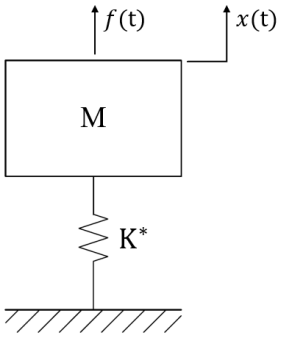

Figure 2.9: One Degree of Freedom system (Adapted from (Moreira, 2004)).

The differential equation of movement takes the form:

$$M\ddot{x}(t) + K^* x(t) = f(t). \tag{2.17}$$

Writing equation (2.17) using exponential terms leads to:

$$-\omega^2 M\bar{X}(\mathrm{j}\omega)\mathrm{e}^{\mathrm{j}\omega t} + K^*\bar{X}(\mathrm{j}\omega)e^{\mathrm{j}\omega t} = F\mathrm{e}^{\mathrm{j}\omega t}. \tag{2.18}$$

The simplification of equation (2.18) results as follows:

$$[K^* - \omega^2 M]\bar{X}(\mathrm{j}\omega) = F. \tag{2.19}$$

The determination of the response function, in the form of a receptance, mobility or accelerance allows the identification of the frequency dependent properties according to the following equations:

$$\text{Receptance} : \alpha(\omega) = \frac{\bar{X}(\mathrm{j}\omega)}{F} = \frac{1}{K^* - \omega^2 M}. \tag{2.20}$$

$$\text{Mobility} : \mathrm{Y}(\omega) = \frac{\bar{V}(\mathrm{j}\omega)}{F} = \frac{\mathrm{j}\omega}{K^* - \omega^2 M}. \tag{2.21}$$

$$\text{Accelerance} : \mathrm{A}(\omega) = \frac{\bar{A}(\mathrm{j}\omega)}{F} = \frac{-\omega^2}{K^* - \omega^2 M}. \tag{2.22}$$

The storage modulus can be obtained with the real part of the stiffness matrix and the loss factor from the ratio between the imaginary and real parts of the stiffness matrix.

Instead of inducing a harmonic force, one can induce a displacement at the base of the system and determine the complex modulus with the analysis of the absolute transmissibility between the response displacement and induced displacement.

Even though the analytical model of the system is quite simple to obtain, experimentally obtaining a system with only one degree of freedom is quite laborious. A torsion mode whose frequency is very similar from the one desired should be restrained and the restriction of such movement can induce unwanted damping which leads to poor results (Moreira, 2004). An efficient one degree of freedom apparatus is described by Vasques et al. (2010b).

2.5 Viscoelastic constitutive modelling

In order to solve static and dynamic problems of structures, the finite element method has been widely used. Introducing viscoelastic materials in these problems requires the development of reliable models in order to accurately describe their behaviour.

As mentioned in the current chapter, the constitutive behaviour of viscoelastic materials depends on frequency, temperature, magnitude and type of excitation. However, obtaining a model that takes into consideration all those variables has not been developed. Thereby, for simplicity, the effects of magnitude and type of excitation are disregarded and isothermal conditions are assumed.

Several mechanical models based on the combination of springs and Newtonian dashpots - viscous elements - were developed. Examples of such models are the Maxwell and Kevin-Voigt models. Even though these were of great interest in the past, writing the constitutive behaviour of viscoelastic materials in the form of a differential equation becomes an arduous labour as the models get more complicated and require higher order differential equations. A great simplification in modelling viscoelastic behaviour has been recognised by the use of fractional calculus. In the fractional derivative model, the viscoelastic behaviour is written in the form of a differential equation where the time derivative order is not an integer number (Vasques et al., 2010a).

2.5.1 Fractional derivative model

In the present work, the fractional derivative model selected to describe the complex modulus of the viscoelastic material as a function of frequency is characterised by 4 parameters. This model is selected as it is fairly simple and allows to accurately describe the dynamic behaviour of real

viscoelastic materials in a wide frequency range (Jones, 2001; Pritz, 1996). The numeric values of the parameters are to be determined using a curve-fitting process. Therefore, the fact that it only requires four parameters to describe the variations of the complex modulus is quite practical as the optimisation process becomes simpler and more efficient with respect to computational complexity.

The differential equation of the fractional derivative model of four parameters describes the relation between the stress tensor and the strain tensor in the following manner:

$$\sigma(t) + \tau^{\alpha} D^{\alpha}\sigma(t) = E_0\varepsilon(t) + \tau^{\alpha} E_{\infty} D^{\alpha}\varepsilon(t), \tag{2.23}$$

where τ, α, E_0 and E_∞ are the four parameters which possess a physical meaning. The parameter E_0 represents the static modulus of elasticity, or even, the dynamic modulus at zero frequency, the parameter E_∞ is the limit value of the dynamic modulus at high frequencies and τ represents the relaxation time of the material. The parameter α is relative to the order of the derivative, and since is a fractional derivative, its value must be placed between $0 < \alpha < 1$ (Pritz, 1996). As such, $D^{\alpha}\sigma(t)$ is the αth order fractional derivative of the stress and $D^{\alpha}\varepsilon(t)$ is the αth order fractional derivative of the strain. As an example, the fractional derivative of the stress is described by:

$$D^{\alpha}\sigma(t) = \frac{1}{\Gamma(1-\alpha)} \frac{\mathrm{d}}{\mathrm{d}t} \int \frac{\sigma(t)}{(t-\tau)^{\alpha}} \mathrm{d}\tau, \tag{2.24}$$

where $\Gamma(x)$ is the Gamma function of argument x and is expressed in equation (2.25).

$$\Gamma(x) = \int_0^{\infty} t^{x-1} \mathrm{e}^{-t} \, \mathrm{d}t. \tag{2.25}$$

In order to include the properties of the viscoelastic layer to predict the FRF of a given structure with a viscoelastic treatment, the mathematical form of the fractional derivative model must be written in the frequency domain. As such, equation (2.23) can be re-written bearing in mind that the derivative term D^{α} can be replaced by a $(\mathrm{j}\omega)^{\alpha}$ term in the frequency domain (Pritz, 1996):

$$\sigma = \frac{E_0 + E_{\infty}(\mathrm{j}\omega\tau)^{\alpha}}{1 + (\mathrm{j}\omega\tau)^{\alpha}} \varepsilon. \tag{2.26}$$

The expression for the complex modulus, $E^*(\mathrm{j}\omega)$, can be derived from equation (2.26), which results in the following:

$$E^*(\mathrm{j}\omega) = \frac{E_0 + E_{\infty}(\mathrm{j}\omega\tau)^{\alpha}}{1 + (\mathrm{j}\omega\tau)^{\alpha}}. \tag{2.27}$$

It is worth mentioning that the preceding logic can be applied in order to obtain the shear complex modulus, $G^*(\mathrm{j}\omega)$. However, the formulation used in the current work is in terms of extensional properties.

Chapter 3

Layerwise Beam Theory

3.1 Introduction

In view of simulating the dynamic behaviour of composite structures, as the ones resultant of the application of a viscoelastic treatment, a spatial finite element model must be developed. In the current work a *Layerwise* beam theory is used.

The kinematics of each layer is modelled independently based on the assumptions dictated by *Timoshenko Beam* theory with the reinforcement of coupling terms that establish the continuity of the displacements in the interfaces of each layer (Moreira et al., 2005; Reddy, 1996). The layers are, then, modelled according to the following assumptions (Moreira et al., 2005):

- All the layers deform both in shear and in extension;
- Deformation through thickness is negligible and discontinuous at layer interfaces;
- For each layer translational and rotary degrees of freedom are considered;
- Linear theories of elasticity and viscoelasticity are assumed;
- Materials are considered to be isotropic and homogeneous in the whole laminate.

The current chapter aims to explain the formulation of a *Layerwise* beam theory for the case of composite beams with viscoelastic treatments, based on the one developed by Moreira et al. (2005) for plates, as well as a 2 node isoparametric finite element formulation.

3.2 Timoshenko Beam Theory

For composite laminated beams, where each layer is composed of a different material, transverse shear deformation is not negligible (Oñate, 2013). As such, *Timoshenko* beam theory is particularly suited for this problems as it accounts for shear deformation.

This theory is based on a number of assumptions which are listed below (Oñate, 2013):

- The vertical displacement, w, is constant throughout the entire cross-section;
- The displacement along the out-of-plane direction (lateral) is null;
- Cross-sections of the beam remain plane after deformation but not necessarily orthogonal to the beam axis.

The displacement field for a single layer *Timoshenko* beam is defined as:

$$\{u\} = \left\{ \begin{array}{cc} w & \psi^y \end{array} \right\}^T, \tag{3.1}$$

where ψ^y is defined by two distinct components: one resultant of the rotation of the beam axis, $\frac{\mathrm{d}w}{\mathrm{d}x}$, and the other as a consequence of the distortion of the cross-section, β^y, as illustrated in figure 3.1 (Oñate, 2013).

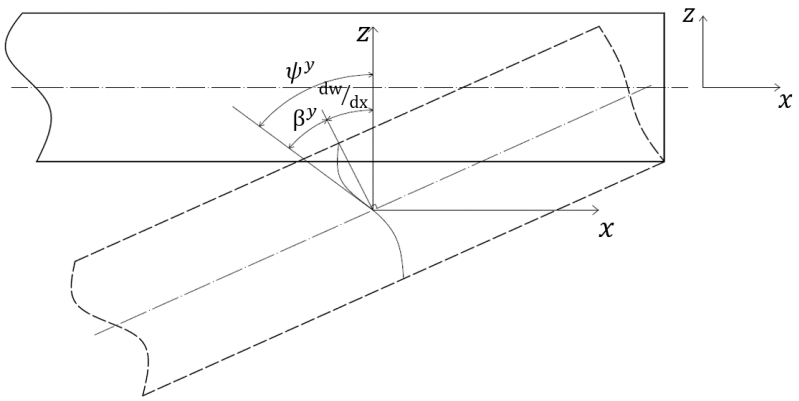

Figure 3.1: Rotation of the transverse cross-section according to *Timoshenko* beam theory (Adapted from (Oñate, 2013)).

3.3 Layerwise Beam Formulation

3.3.1 Displacement Field

The problem is of a composite beam of length, l, and width, b, composed of n layers as evidenced in figure 3.2.

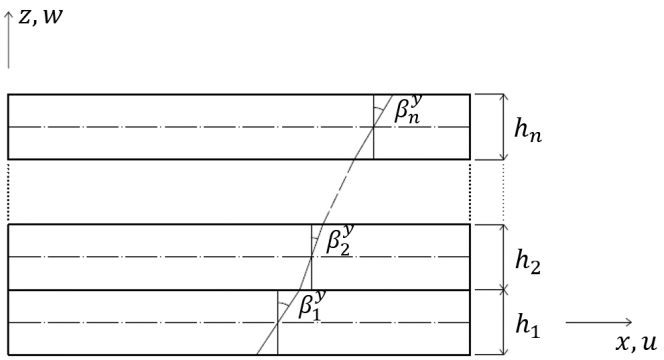

Figure 3.2: Generic layerwise model (Adapted from (Moreira et al., 2005)).

Considering a generic layer, k, the displacement field can be defined as written in equation (3.2).

$$\{u\}_k = \left\{ \begin{array}{c} u_k \\ w_k \end{array} \right\} = \left\{ \begin{array}{c} u_0 + \frac{h_1}{2}\beta_1^y + \sum_{j=2}^{k-1} h_j \beta_j^y + \frac{h_k}{2}\beta_k^y + z_k \beta_k^y \\ w_0 \end{array} \right\}, \tag{3.2}$$

where u_0 and w_0 are, respectively, the horizontal and vertical translations and β_k^y is the rotation of the cross-section perpendicular to the longitudinal axis of the beam.

The displacement field can, thus, be written in matrix form through a set of generalised variables:

$$u_k = [\mathcal{N}]_k \{d\}, \tag{3.3}$$

where d is defined as written in equation (3.4) and $[\mathcal{N}]_k$ matrix is written in equation (3.5).

$$\{d\} = \left\{ \begin{array}{ccccccc} u_0 & w_0 & \beta_1^y & ... & \beta_k^y & ... & \beta_n^y \end{array} \right\}^T, \tag{3.4}$$

$$[\mathcal{N}]_k = \left[\begin{array}{ccccccccccc} 1 & 0 & \frac{h_1}{2} & \dots & h_j & \dots & \frac{h}{2} + z_k & 0 & \dots & 0 \\ 0 & 1 & 0 & \dots & 0 & \dots & 0 & 0 & \dots & 0 \end{array} \right]. \tag{3.5}$$

3.3.2 Strain Field

The strain field of the k-th layer is derived by pre-multiplying the displacement field by a differential operator $\mathcal{L}$ defined as follows:

$$[\mathcal{L}] = \left[\begin{array}{cc} \frac{\partial}{\partial x} & 0 \\ \frac{\partial}{\partial z} & \frac{\partial}{\partial x} \end{array} \right], \tag{3.6}$$

resulting in a strain vector, $\tilde{\varepsilon}$, as expressed in equation (3.7).

$$\{\tilde{\varepsilon}\} = \left\{ \begin{array}{c} \varepsilon_{xx} \\ \gamma_{xz} \end{array} \right\}. \tag{3.7}$$

Equation (3.8) evidences the terms resultant from the membrane, coupling, bending and transverse shear deformation, which are identified through the superscripts M, C, B and S, respectively. It also divides the strain vector in three components for integration convenience.

$$\{\varepsilon\} = \{\{\varepsilon\}_k^M + \{\varepsilon\}_k^C;\ \{\varepsilon\}_k^B;\ \{\gamma_{xz}\}_k^S\}, \tag{3.8}$$

where each of the components can be determined as evidenced from equation (3.9) to (3.12).

$$\varepsilon_{xx}^M = \frac{\partial u_0}{\partial x}; \tag{3.9}$$

$$\varepsilon_{xx}^C = \frac{h_1}{2}\frac{\partial \beta_1^y}{\partial x} + \sum_{j=2}^{k-1} h_j \frac{\partial \beta_j^y}{\partial x} + \frac{h_k}{2}\frac{\partial \beta_k^y}{\partial x}; \tag{3.10}$$

$$\varepsilon_{xx}^B = z_k \frac{\partial \beta_k^y}{\partial x}; \tag{3.11}$$

$$\gamma_{xz}^S = \beta_k^y + \frac{\partial w}{\partial x}. \tag{3.12}$$

The deformation matrix of the k-th layer $[\tilde{\mathcal{B}}]_k$ can be defined as follows:

$$[\tilde{\mathcal{B}}]_k = [\mathcal{L}][\mathcal{N}]_k. \tag{3.13}$$

Recalling equation (3.8), the deformation matrix can be rearranged evidencing the different strain components, leading to three submatrixes that are evidenced in equation (3.14).

$$[\mathcal{B}]_k = \left[\begin{array}{cccccc|c} \frac{\partial}{\partial x} & 0 & \frac{h_1}{2}\frac{\partial}{\partial x} & ... & h_j\frac{\partial}{\partial x} & \frac{h_k}{2}\frac{\partial}{\partial x} & \\ 0 & 0 & 0 & 0 & 0 & z_k\frac{\partial}{\partial x} & [0] \\ 0 & \frac{\partial}{\partial x} & 0 & 0 & 0 & 1 & \end{array}\right]. \tag{3.14}$$

Thereby, the strain field can be obtained using equation (3.15):

$$\{\varepsilon\}_k = [\mathcal{B}]_k\{d\}. \tag{3.15}$$

3.3.3 Stress Field

The stress field of a generic k-th layer, bearing in mind the combination of the different components of the strain field, can be defined as follows:

$$\{\sigma\}_k = \left\{ \begin{array}{ccc} \{\sigma\}_k^M + \{\sigma\}_k^C & \{\sigma\}_k^B & \{\tau\}_k^S \end{array} \right\}^T. \tag{3.16}$$

The aforementioned stress field is determined by the multiplication of the constitutive law of the material, defined in matrix form as $[\mathcal{D}]_k$, by the strain field vector, $\{\varepsilon_k\}$ - equation (3.17).

$$\{\sigma\}_k = [\mathcal{D}]_k\{\varepsilon\}_k. \tag{3.17}$$

The definition of matrix $[\mathcal{D}]_k$, grouping the terms relative to the bending, membrane and shear components, is as follows:

$$[\mathcal{D}]_k = \left[\begin{array}{ccc} [D]_k^M & [0] & [0] \\ [0] & [D]_k^B & [0] \\ [0] & [0] & [G]_k^S \end{array}\right], \tag{3.18}$$

where $[D]_k^M$, $[D]_k^B$ and $[G]_k^S$ for a homogeneous isotropic material are defined in the following equations:

$$[D]_k^M = [D]_k^B = \frac{E_k}{1-\nu_k^2}\left[\begin{array}{ccc} 1 & \nu_k & 0 \\ \nu_k & 1 & 0 \\ 0 & 0 & \frac{1-\nu_k}{2} \end{array}\right], \tag{3.19}$$

$$[G]_k^S = \frac{E_k}{2(1-\nu_k)}\left[\begin{array}{cc} 1 & 0 \\ 0 & 1 \end{array}\right]. \tag{3.20}$$

E_k represents the Young's modulus and ν_k represents the Poisson's ratio of the material of the generic layer k. To model viscoelastic layers according to the matrixes previously derived, a unitary Young's modulus is assumed and the complex frequency dependence is introduced by multiplying the constitutive law above mentioned by the complex modulus obtained, for example, with a fractional derivative formulation.

3.3.4 Strain Energy

The strain energy, Π^P, of the entire composite beam is obtained as follows:

$$\Pi^P = \sum_{k=1}^{n}\frac{1}{2}\int_{\Omega_k}\{\varepsilon\}_k^T\{\sigma\}_k \, \mathrm{d}\Omega_k, \tag{3.21}$$

where Ω_k is the volume domain of layer k.

The application of equation (3.15) in equation (3.21) and the transformation of the integral over the volume of the sample in an integral over the area, A, and thickness of layer k, z_k, results in:

$$\Pi^P = \sum_{k=1}^{n} \frac{1}{2} \int_A \int_{z_k} \{d\}^T [\mathcal{B}]_k^T [\mathcal{D}]_k [\mathcal{B}] \{d\} \, \mathrm{d}z_k \mathrm{d}A. \tag{3.22}$$

For integration purposes matrix $[\mathcal{B}]_k$ is transformed in a generalised matrix, $[\hat{\mathcal{B}}]$, as the following one:

$$[\hat{\mathcal{B}}]_k = \begin{bmatrix} [\mathcal{B}]_k^{MC} \\ \frac{1}{z_k}[\mathcal{B}]_k^B \\ [\mathcal{B}]_k^S \end{bmatrix}. \tag{3.23}$$

Substituting equation (3.23) and computing the integral over the thickness of the considered layer, results as follows:

$$\Pi^P = \sum_{k=1}^{n} \frac{1}{2} \int_l \{d\}^T [\hat{\mathcal{B}}]_k^T [\hat{\mathcal{D}}]_k [\hat{\mathcal{B}}] \{d\} b \, \mathrm{d}l, \tag{3.24}$$

where $[\tilde{\mathcal{D}}]_k$ is defined according to equation (3.25).

$$[\tilde{\mathcal{D}}]_k = \begin{bmatrix} h_k [D]_k^M & [0] & [0] \\ [0] & \frac{h_k^3}{12}[D]_k^B & [0] \\ [0] & [0] & h_k [G]_k^S \end{bmatrix}. \tag{3.25}$$

3.3.5 Kinetic Energy

The kinetic energy of the composite beam, Π^K, is obtained according to the following integral equation:

$$\Pi^K = \sum_{k=1}^{n} \frac{1}{2} \int_{\Omega_k} \{\dot{u}\}_k^T [\mathcal{J}]_k \{\dot{u}\}_k \, \mathrm{d}\Omega_k, \tag{3.26}$$

where $\{\dot{u}\}_k$ represents the velocity field of each layer and $[\mathcal{J}_k]$ is the inertia matrix, being the latter expressed in equation (3.27).

$$[\mathcal{J}]_k = \begin{bmatrix} \rho_k & 0 \\ 0 & \rho_k \end{bmatrix}. \tag{3.27}$$

Expressing equation (3.26) in terms of a generalised velocity field, results as follows:

$$\Pi^K = \sum_{k=1}^{n} \frac{1}{2} \int_{\Omega_k} \{\dot{d}\}^T [\mathcal{N}]_k^T [\mathcal{J}]_k [\mathcal{N}] \{\dot{d}\}_k \, \mathrm{d}\Omega_k, \tag{3.28}$$

The simplification of the integral in equation (3.28) and considering $[J]_k = [N]^T [\mathcal{J}]_k [N]$ results in:

$$\Pi^K = \sum_{k=1}^{n} \frac{1}{2} \int_A \int_{z_k} \{\dot{d}\}^T [J]_k \{\dot{d}\}_k \, \mathrm{d}z_k \mathrm{d}A. \tag{3.29}$$

Calculating the integral over the thickness of the layer results in equation (3.30).

$$\Pi^K = \sum_{k=1}^{n} \frac{1}{2} \int_A \{\dot{d}\}^T [\hat{J}]_k \{\dot{d}\}_k \, \mathrm{d}A, \tag{3.30}$$

where $[\hat{J}]_k$ can finally be written:

$$[\hat{J}]_k = \rho_k h_k \left[\begin{array}{ccccccc|c} 1 & 0 & \frac{h_1}{2} & \cdots & h_j & \cdots & \frac{h_k}{2} & \\ & 1 & 0 & \cdots & 0 & \cdots & 0 & \\ & & \frac{h_1^2}{4} & \cdots & \frac{h_1}{2}h_j & \cdots & \frac{h_1 h_k}{4} & \\ & & & \ddots & & & & [0] \\ & & & & h_j^2 & \cdots & h_j \frac{h_k}{2} & \\ & & & & & \ddots & & \\ \text{sym.} & & & & & & \frac{h_k^2}{3} & \\ \hline & & & & [0] & & & [0] \end{array}\right] \tag{3.31}$$

3.3.6 Virtual work of the distributed loads

For a transverse distributed load applied in the surface of the beam the resultant virtual work is calculated by:

$$\delta W = \int_l \{\delta d\}^T \{q\} \, \mathrm{d}l, \tag{3.32}$$

where $\{\delta d\}$ is the virtual displacement and $\{q\}$ the load vector.

3.3.7 Variational Formulation

The formulation of the problem according to variational quantities is obtained using the Hamilton's principle, whose mathematical equation is described by:

$$\delta \int_{t_1}^{t_2} (\Pi^K - \Pi^P) \, \mathrm{d}t + \int_{t_1}^{t_2} \delta W \, \mathrm{d}t = 0. \tag{3.33}$$

Introducing the developed equations (3.24), (3.30) and (3.33) and integrating by parts leads to:

$$\begin{aligned} \int_{t_1}^{t_2} \Bigg(-\sum_{k=1}^{n} \int_l \{\delta d\}^T [\hat{J}]_k \{\ddot{d}\} b \, \mathrm{d}l - \sum_{k=1}^{n} \int_l \{\delta d\}^T [\hat{\mathcal{B}}]_k^T [\hat{\mathcal{D}}]_k^T [\hat{\mathcal{B}}]_k^T \{d\} \, \mathrm{d}l \\ + \int_l \{\delta d\}^T \{q\} \Bigg) \mathrm{d}t = 0. \end{aligned} \tag{3.34}$$

Seeing that equation (3.34) must be satisfied for every $\{\delta d\}$ within the interval defined by t_1 and t_2 it can be expressed as:

$$\sum_{k=1}^{n} \int_l \{\delta d\}^T [\hat{J}]_k \{\ddot{d}\} b \, \mathrm{d}l + \sum_{k=1}^{n} \int_l \{\delta d\}^T [\hat{\mathcal{B}}]_k^T [\hat{\mathcal{D}}]_k^T [\hat{\mathcal{B}}]_k^T \{d\} \, \mathrm{d}l - \int_l \{\delta d\}^T \{q\} \; = 0. \tag{3.35}$$

3.4 Finite Element Formulation

The finite element proposed for modeling the beams with an integrated viscoelastic treatment is the 2-node isoparametric beam element. A natural coordinate system is, then, defined for each element, as depicted in figure 3.3, according to which both mass and stiffness matrix are determined.

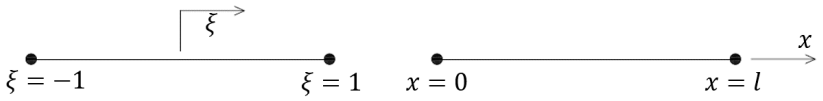

Figure 3.3: Left: Natural coordinate system. Right: Cartesian coordinate system.

The transformation from the local coordinate system to the cartesian coordinate system is determined mathematically as expressed in equation (3.36).

$$x(\xi) = \sum_{i=1}^{2} N_i x_i, \tag{3.36}$$

where N is the shape function matrix and x_i the coordinate of each node in the cartesian coordinate system. The shape functions of each node of the element, used to interpolate both the geometry of the beam and the degrees of freedom of the element, are the linear Lagrange polynomials:

$$N_1 = \frac{1}{2}(1-\xi), \tag{3.37}$$

$$N_2 = \frac{1}{2}(1+\xi). \tag{3.38}$$

The shape function matrix, $[N]$, is then defined as:

$$[N]_i = \begin{bmatrix} N_i & 0 & 0 \\ & \ddots & 0 \\ \text{sym.} & & N_i \end{bmatrix}, \tag{3.39}$$

$$[N] = [N_1 \ N_2]. \tag{3.40}$$

The nodal displacement field, $\{d_e\}$, for a composite structure with n lamina is defined as follows:

$$\{d_e\} = \left\{ \ u_1 \quad w_1 \quad \beta_{11} \quad \dots \quad \beta_{n1} \quad u_2 \quad w_2 \quad \beta_{12} \quad \dots \quad \beta_{n2} \quad \dots \ \right\}^T. \tag{3.41}$$

The generalised displacement field is calculated from the nodal displacement field according to equation (3.42).

$$\{d\} = [N]\{d_e\}. \tag{3.42}$$

3.4.1 Weak Form

The introduction of the nodal displacement and acceleration fields in equation (3.35), results in:

$$\sum_{e=1}^{n_E}\left(\sum_{k=1}^{n}\int_l\{\delta d^e\}^T[N]^T[\hat{J}]_k[N]\{\ddot{d^e}\}b\ \mathrm{d}l^e+\sum_{k=1}^{n}\int_l\{\delta d^e\}^T[N]^T[B]_k^T[\hat{\mathcal{D}}]_k^T[B]_k[N]\{d^e\}\ \mathrm{d}l^e - \int_l\{\delta d^e\}^T[N]^T\{q\}\ \mathrm{d}l^e\right)=0, \tag{3.43}$$

$$\begin{aligned}\sum_{e=1}^{n_E}\Bigg(&\sum_{k=1}^{n}\int_l\{\delta d^e\}^T[N]^T[\hat{J}]_k[N]\{\ddot{d^e}\}b\ \mathrm{d}l^e\\ &+\sum_{k=1}^{n}\int_l\{\delta d^e\}^T[N]^T[B]_k^T[\hat{\mathcal{D}}]_k^T[B]_k[N]\{d^e\}\ \mathrm{d}l^e-\int_l\{\delta d^e\}^T[N]^T\{q\}\ \mathrm{d}l^e\Bigg)=0,\end{aligned} \tag{3.44}$$

where $[B]_k$ matrix can de defined as:

$$[B]_k=[\hat{\mathcal{B}}]_k[N]. \tag{3.45}$$

As $\{\delta d^e\}^T$ is arbitrary, equation (3.44) allows the definition of the mass matrix, $[M^e]$, stiffness matrix, $[K^e]$, and load vector, $\{f^e\}$, as follows:

$$[M^e]=\sum_{k=1}^{n}[M^e]_k=\sum_{k=1}^{n}\int_{l^e}[N]^T[\hat{J}]_k[N]b\ \mathrm{d}l^e, \tag{3.46}$$

$$[K^e]=\sum_{k=1}^{n}[K^e]_k=\sum_{k=1}^{n}\int_{l^e}[B]_k^T[\hat{\mathcal{D}}]_k[B]_kb\ \mathrm{d}l^e, \tag{3.47}$$

$$\{f^e\}=\int_{l^e}[N]^T\{q\}\ \mathrm{d}l^e. \tag{3.48}$$

3.4.2 Equations of Motion

The relation between the elemental degrees of freedom and the global ones is usually written using a connectivity matrix, $[R^e]$:

$$\{d^e\}=[R^e]\{d_a\}. \tag{3.49}$$

As such, equation (3.44) can be written as:

$$\{\delta d_a\}^T[M]\{\ddot{d_a}\}+\{\delta d_a\}^T[K]\{d_a\}-\{\delta d\}^T\{f_a\}=0, \tag{3.50}$$

where $[M]$, $[K]$ and $\{f_a\}$ are defined as:

$$[M]=\sum_{k=1}^{n}[R^e]^T[M^e][R^e], \tag{3.51}$$

$$[K]=\sum_{k=1}^{n}[R^e]^T[K^e][R^e], \tag{3.52}$$

$$\{f\} = \int_{l^e} [R^e]^T \{f^e\}. \tag{3.53}$$

In conclusion, the discrete equations of motion with the active degrees of freedom can be stated as expressed in equation (3.54).

$$[M]\{\ddot{d}_a\} + [K]\{d_a\} = \{f\}. \tag{3.54}$$

Chapter 4

Experimental Data

4.1 Introduction

The experimental procedure consists on the determination of frequency response functions of a bare aluminium beam as well as three sandwich beams constituted by two outer aluminium layers and a viscoelastic core. The measured data is then used to validate the identification methods proposed and to, consequently, determine the parameters of the fractional derivative model, thus identifying the dynamic properties of the material.

4.2 Viscoelastic Material

The material to be tested in the present work is the 3M ISD112 which is an acrylic polymer based viscoelastic material that has been widely used in many applications to reduce vibrations and/or shock. A few of its application fields include the automotive, electrical or even aerospace markets.

In figure 4.1 is shown the reduced frequency nomogram where the variation of the shear storage modulus, $G'(\omega, T)$, and loss factor, $\eta(\omega, T)$, is represented for different sets of temperature and frequency. This nomogram is supplied by the manufacturer for reference only (3M, 2012).

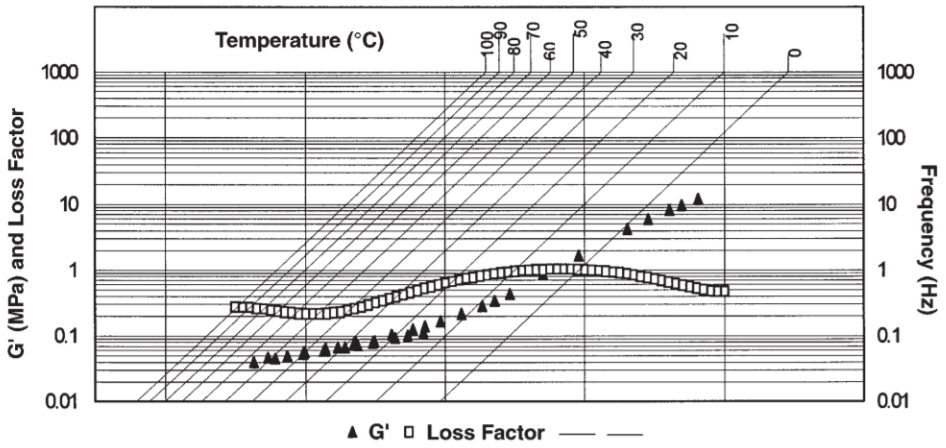

Figure 4.1: Reduced Frequency Nomogram of the viscoelastic material 3M ISD112 (3M, 2012).

For further use, it is considered that the viscoelastic material possesses a volumic mass of 1140 kgm^{-3} (Moreira, 2004).

4.3 Experimental samples

The test samples are sandwich beams constituted of a viscoelastic core between two aluminium layers, as illustrated in figure 4.2. The notation used for beam geometry is: l for the free length of the beam, a for the elastic layer thickness, b for the width of the section of the beam and lastly, e, for the thickness of the viscoelastic layer.

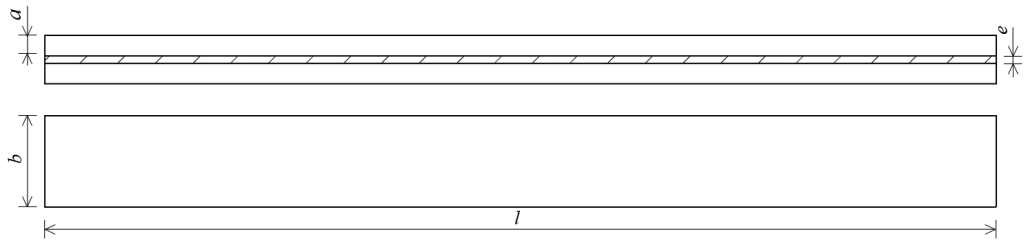

Figure 4.2: Schematic representation of the composite beams tested.

In order to characterise the complex modulus of the viscoelastic material, the exact properties (Young's modulus, E, and loss factor, η) of the aluminium layer must be determined. As such a bare aluminium beam is tested. The elastic and composite beams tested can be seen in figure 4.3 and their dimensions are described in table 4.1.

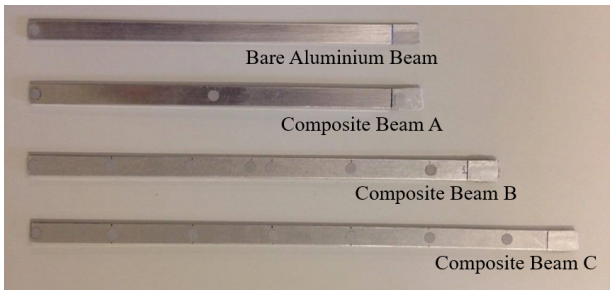

Figure 4.3: Bare beam and composite beams tested.

Table 4.1: Test sample geometry.

Sample	l [mm]	a [mm]	b [mm]	e [mm]
Bare Beam	180	1	10	-
A	180	1	10	0.127
B	220	1	10	0.127
C	260	1	10	0.127

For further consideration, the required aluminium physical properties are evidenced in table 4.2.

Table 4.2: Bare aluminium beam properties.

	m [g]	ρ [kgm^{-3}]
Aluminium	4.955	2541

4.4 Experimental Set-Up

The experimental set-up reproduces a system of a vibrating beam fixed at the root end and free at the opposite one submitted to an impulse force. In order to legitimise the experimental data obtained, a few previous concerns must be taken relative to the experimental set-up and procedure:

- One must guarantee that the experimental set-up and procedure accurately reproduce the analytical model developed in terms of boundary conditions and load application;
- Several measurements must be taken at different times to ensure self-consistency of the data, bearing in mind that precise results do not necessarily imply accurate results;
- Rigid body modes of the structure that influence the frequency response functions must be efficiently fixed;
- Both thermal and molecular equilibrium of the sample must be achieved for each experimental measure.

The apparatus developed consists of a rigid test fixture, which is fixed on a test bench, represented in figure 4.4. This component clamps the test specimen using six screws fastened with a constant torque (approximately 20 Nm). The clamped length of each beam corresponds to 15 mm.

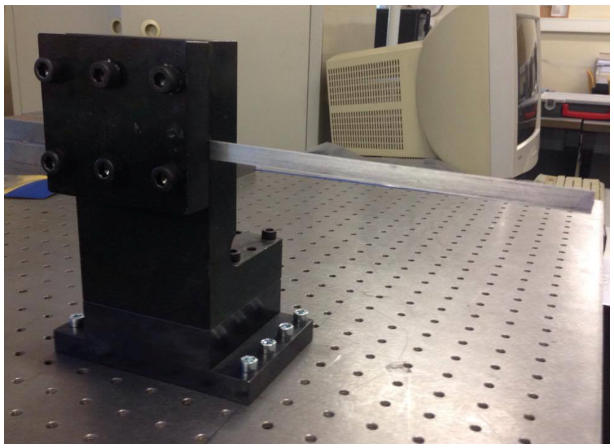

Figure 4.4: Clamping system.

The excitation force is applied with an impulse hammer (*DYTRAN Instruments Model: 5800SL*) which is shown in figure 4.5.

The point of impact must be carefully chosen. Firstly, it must be applied in the center line of the vibrating beam to avoid the excitation of undesired torsion modes. Secondly, the selection of the horizontal position of the point of application is conditioned by the quality of the response function in such point. In other words, the impact should not be applied close to nodal points of the bending vibrational modes.

Figure 4.5: Impulse hammer.

The surface vibration of the beam is measured in terms of velocity of the free end of each beam with a non-contact laser doppler vibrometer. This measuring system does not interfere with the mass or stiffness of the composite specimen. The laser vibrometer includes a sensor head that sends and receives a helium laser and a controller which decodes the signal from the laser head. Both laser head and the controller are shown in figure 4.6.

(a) Laser head.

(b) Vibrometer controller.

Figure 4.6: Laser Doppler Vibrometer System.

The signal from the piezoelectric force sensor on the impact hammer and the signal from the laser vibrometer controller are sent to an FFT spectral analyser (*Brüel and Kjaer, Signal Analyzer Unit Type 2035*) - figure 4.7 - where the frequency response functions are generated. The FRFs will be designated hereinafter by two subscripts: the first one indicating the distance, in millimeters, between the section where the response is measured and the clamped root end and the second one indicating the distance between the response section and the clamped end of the beam.

Figure 4.7: Signal Analyser Unit.

A vital information concerning the transducers that must be correctly introduced in the analyser is their sensitivity, which is listed in table 4.3.

Table 4.3: Sensitivity of the transducers used.

Transducer	Sensitivity
Impulse Hammer	23.7 mV/N
Laser Vibrometer	8 V/ms^{-1}

The entire experimental setup is illustrated in the diagram of figure 4.8.

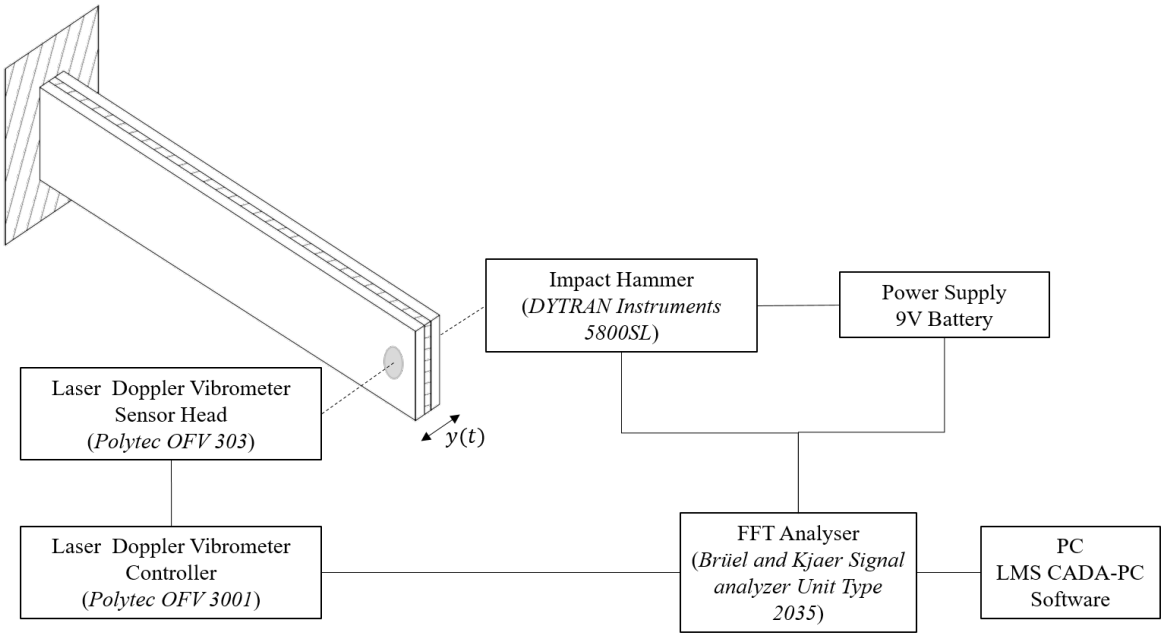

Figure 4.8: Diagram of the experimental procedure to measure the FRFs.

4.5 Experimental Results

4.5.1 Bare Beam FRF

Analysing the first five natural shapes of the aluminium beam, illustrated in figure 4.9, it can be seen that the free end of the beam is the preferred point as all the natural modes contribute to the response in such node. However, contemplating the application of the impact force in different points of the beam, the nodes of vibration of the low order natural modes must be avoided. The numeric value of such nodes are summarised in table 4.4 as a function of the beam's length, l.

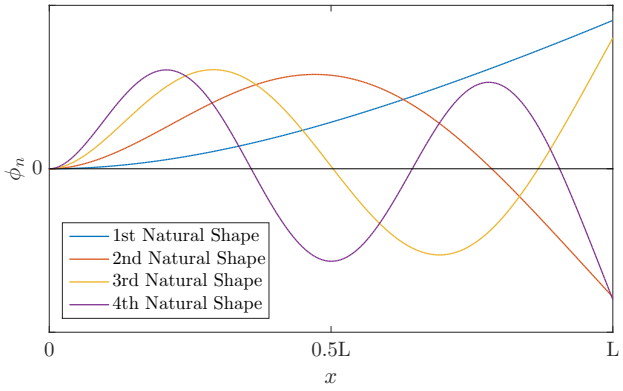

Figure 4.9: Representation of the natural shapes of a clamped-free bending beam.

Table 4.4: Nodes of vibration of a clamped-free bending beam.

	Vibration Nodes (l^{-1})
1st Mode	-
2nd Mode	0.774
3rd Mode	0.5/0.868
4th Mode	0.356/0.644/0.906

As such, three impact points are selected concerning the natural nodes of vibration as well as the discretisation of the beam for finite element method application, which is developed in forthcoming chapters. The points of application of the impulsive force are summarised in the following table.

Table 4.5: Points of application of the impulsive force of the bare beam.

	Impact Point [mm]	Response Point [mm]
1	44	180
2	108	180
3	180	180

The experimental mobilities are obtained in a frequency range of [0 200] Hz ($\Delta f = 0.25$ Hz) making possible to accurately identify two natural frequencies. The experimental data relative to the bare beam can be consulted in Appendix A.

4.5.2 Composite Beam FRF

Similarly to the base beam experimental procedure, different frequency response functions are obtained for the composite beams by varying the point of application of the impulse. However, the natural shapes of vibration of composite beams are not as directly determined as the ones of a simple elastic beam. As such, the selection of such points is performed through experiment, bearing in mind the discrete degrees of freedom considered for finite element method application.

Composite Beam A

For the composite beam A, of length $l = 180$ mm, also three points are selected for the impact application. The experimental mobilities are measured in a bandwidth of [0 400] Hz ($\Delta f = 0.5$ Hz), which includes the representation of two natural modes. The points of application of the impulsive force are summarised in table 4.6.

Table 4.6: Points of application of the impulsive force of composite beam A.

	Impact Point [mm]	Response Point [mm]
1	80	180
2	108	180
3	180	180

The frequency response functions can be observed in Appendix A.

Composite Beam B

For the composite beam B, of length $l = 220$ mm, the mobilities are obtained in two frequency bandwidths: [0 400] Hz ($\Delta f = 0,5$ Hz) and [0 800] Hz ($\Delta f = 1$ Hz) which leads to the identification of two and three natural modes, respectively.

The points where the experimental frequency response functions are obtained are displayed in table 4.7.

Table 4.7: Points of application of the impulsive force.

	Impact Point [mm]	Response Point [mm]
1	88	220
2	128	220
3	220	220

Composite Beam C

For the composite beam C, of length $l = 260$ mm, the mobilities are experimentally determined using two different bandwidths: [0 - 200] Hz ($\Delta f = 0.25$ Hz) and [0 400] Hz ($\Delta f = 0.5$ Hz). In the first bandwidth, two natural modes can be identified with higher sampling frequency whereas in the second bandwidth, three natural modes are present.

The points where the frequency response functions are obtained are displayed in table 4.8.

Table 4.8: Points of application of the impulsive force.

	Impact Point [mm]	Response Point [mm]
1	108	260
2	172	260
3	260	260

4.5.3 Notes on the experimental FRFs

As evidenced in the graphs present in Appendix A, the frequency response functions of the composite beams exhibit a distortion on the second mode of vibration.

This distortion could be caused by a spurious torsion mode. However, analysing the work of Fernandes (2013) where transmissibility functions were measured using a distinct set-up and the same composite beams were used, the distortion on such mode is also noticeable. As such, it indicates that the distortion is a result of a defect on the samples rather than an inconsistency of the experimental set-up. It may be caused by a lack of straightness of the base metallic beams, since they are cut from a bigger plate, leading to poor results in the second mode of vibration. This inconsistency is more marked in direct mobilities and especially the ones of the longest composite beam (composite beam C).

Chapter 5

Two-Step Identification Method

5.1 Introduction

The characterisation of the frequency dependent properties of the viscoelastic material is performed using an inverse identification method. In this method, the frequency dependence of the viscoelastic material is modelled using a fractional derivative model of four parameters. Thus, in order to identify the storage modulus and loss factor properties of the viscoelastic material, the parameters of the fractional derivative model must be determined.

In the current work, the identification method proposed is based on the one developed by Kim and Lee (2009). This method uses a finite element model (FEM) of a composite beam and a search algorithm in order to minimise the difference between the measured frequency response functions and the ones obtained from the FEM. This minimisation is achieved by optimising the parameters of the fractional derivative model. The identification method is divided into two steps: the first conduces to a resonant frequency alignment and the second one to a minimisation of the difference in magnitude of the measured FRF data and simulated data.

5.2 Finite Element Model

In order to discretise the composite beam for finite element modelling a *Layerwise* theory is used, where each layer is modelled by a *Timoshenko* beam theory.

The resulting discrete differential equations of motion can be described as follows:

$$[M]\{\ddot{x}\} + [K^*]\{x\} = \{f(t)\}, \tag{5.1}$$

where $[M]$ is the mass matrix, $[K^*]$ the complex stiffness matrix, $\{x\}$ and $\{f(t)\}$ are the displacement and force vectors, respectively.

The stiffness matrix resultant of the FEM has two components: the one relative to the elastic layers of the composite beam and the one relative to the viscoelastic layer. The viscoelastic stiffness matrix is built with a unitary constant modulus. The frequency dependence is then introduced by multiplying such matrix by the complex modulus attained from the fractional derivative model.

5.3 Numerical Frequency Response Function

The FRF can be obtained numerically using the modal superposition principle, which means that the response is considered as a sum of the different modes of vibration. As such, it is necessary to determine the natural frequencies and mode shapes of the beam. Naturally, in

order to obtain the vibration modes, an eigenproblem must be solved. As an approximation, the real eigenproblem is solved instead of the determination of complex eigenvalues and eigenvectors.

$$\Re[K^*]\{u\} = \lambda^2[M]\{u\}, \tag{5.2}$$

where $\{u\}$ and λ^2 are the eigenvectors and eigenvalues, respectively.

The stiffness matrix can not be considered frequency independent while solving the eigenproblem due to decoupling effects induced by the viscoelastic layer in structures with sandwich damping treatments, as the ones used in this work. The mechanical properties can, however, be assumed constant in the vicinity of each mode and the eigensolution can be determined independently. The complex stiffness matrix is iteratively updated at the value of frequency of each iteration of each natural mode. Once the convergence of the natural frequency of the natural mode in analysis is verified the respective eigenvalue and eigenvector are saved and the modal loss factor can be determined. This approach is called Iterative Modal Strain Energy and its procedure is as follows (Vasques et al., 2010a).

IMSE Algorithm

Step 1. Eigensolution with $\omega = \omega^0 = 0$ rad/s

$$\Re[K^*(\mathrm{j}\omega^0)]\{u_r\} = (\omega_r^0)^2[M]\{u_r\} \tag{5.3}$$

Step 2. Loop for each eigenpair $(\omega_r^0, \{u_r\})$ with $r = 1, ..., p$.

1. Initial Value
$$\omega_r^i = \omega_r^0 \tag{5.4}$$

2. Iterative loop for each natural frequency and mode shape

   - Eigensolution $(\omega_s^0, \{u_s\})$ with $s = 1, ..., p$
   $$\Re[K^*(\mathrm{j}\omega_r^i)]\{u_s\} = (\omega_s^{i+1})^2[M]\{u_s\} \tag{5.5}$$

   - Iterated natural frequency
   $$\begin{cases} \omega_s^{i+1} : rejected, & s < r \\ \omega_r^{i+1} = \sqrt{(\omega_s^{i+1})^2}, & s = r \end{cases}$$

   - Convergence condition test
   $$\Delta_\omega = \frac{|\omega_r^{i+1} - \omega_r^i|}{\omega_r^{i+1}} \leq \Delta_{max} = 1 \times 10^{-6} \tag{5.6}$$

3. Modal loss factor
$$\{\phi_r\} = \frac{\{u_r\}}{\sqrt{\{u_r\}^T[M]\{u_r\}}} \tag{5.7}$$

$$\eta_r = \frac{\{\phi_r\}^T \Im[K^*(\mathrm{j}\omega_r^{i+1})]\{\phi_r\}}{\{\phi_r\}^T \Re[K^*(\mathrm{j}\omega_r^{i+1})]\{\phi_r\}} \tag{5.8}$$

In order to obtain the system's response as a superposition of the several modes of vibration, a change into a principal system of coordinates must be performed.

$$\{x(t)\} = [\Phi]\{p(t)\}, \tag{5.9}$$

where $[\Phi]$ is the eigenvector matrix and $\{p(t)\}$ are the natural coordinates.

Bearing in mind the orthonormality property of eigenvectores, equation 5.1 can be written as follows:

$$\lceil I \rfloor \{\ddot{p}(t)\} + \lceil \omega_r^2(1+\mathrm{j}\eta_r) \rfloor \{p(t)\} = \{f(t)\}, \tag{5.10}$$

where $\lceil I \rfloor$ is an identity matrix, ω_r the r-th natural frequency, η_r the modal loss factor and $\{f(t)\}$ the excitation load.

Expressing the natural coordinates in the frequency domain, as evidenced in equation (5.11), the equation of motion of the r-th degree of freedom can be written as in equation (5.12).

$$\{p(t)\} = \{P(\mathrm{j}\omega)\}\mathrm{e}^{\mathrm{j}\omega t}, \tag{5.11}$$

$$-\omega^2 P_r(\mathrm{j}\omega)\mathrm{e}^{\mathrm{j}\omega t} + \left(\omega_r^2(1+\mathrm{j}\eta_r)\right) P_r(\mathrm{j}\omega)\mathrm{e}^{\mathrm{j}\omega t} = \{\Phi_r\}^T\{F\}\mathrm{e}^{\mathrm{j}\omega t}, \tag{5.12}$$

where $P(\mathrm{j}\omega)$ is the displacement phasor in the principal coordinate system and $\{F\}$ is the load vector in the frequency domain.

The displacement phasor can then be obtained from equation (5.13) as follows:

$$P_r(\mathrm{j}\omega) = \frac{\{\phi_r\}^T\{F\}}{\omega_r^2(1+\mathrm{j}\eta_r) - \omega^2}. \tag{5.13}$$

Once the modal response is attained in the natural coordinate system, the response of the system in the generalised degrees of freedom can finally be determined as expressed in the following equation:

$$\{\bar{X}(\mathrm{j}\omega)\} = \sum_{r=1}^{n} P_r(\mathrm{j}\omega)\{\phi_r\}. \tag{5.14}$$

For the particular case of $\{F\}$ being a unitary load exclusively applied in one degree of freedom, i, $\{\bar{X}_i(\mathrm{j}\omega)\}$ of equation (5.14) corresponds to the receptance function, $\{\alpha_i(\mathrm{j}\omega)\}$.

The function used in the minimisation process is, however, relative to the velocity of the beam. The mobility can be determined through derivation of the receptance function in the frequency domain according to the following equation:

$$\{Y_i(\mathrm{j}\omega)\} = \mathrm{j}\omega\{\alpha_i(\mathrm{j}\omega)\}. \tag{5.15}$$

The vector of mobilities written above contains the FRFs of every degree of freedom of the beam resultant of the application of an impulse in the node i. Since the experimental FRF are obtained relative to the node at the free end of the beam, j, and in the minimisation process merely the magnitude of the FRF is adjusted, the numerical FRF can be written as:

$$FRF_{num} = |Y_{ji}(\mathrm{j}\omega)|. \tag{5.16}$$

5.4 Identification Method

In order to widen the convergent region, and thus escaping from local minimum values for the parameters, a two-step identification method is applied. The method is programmed in the software `Matlab`® using the minimisation functions available in the `Optimization Toolbox`® and in the `Global Optimization Toolbox`®.

In the first step, only the natural frequencies are aligned by minimising the square difference between those obtained experimentally and those determined analytically as illustrated in figure 5.1a. The minimisation function used in the first step is expressed in equation (5.17).

$$f_1 = \sum_{r=1}^{m} (\omega_{rexp} - \omega_{rnum})^2, \tag{5.17}$$

where the subscripts *num* and *exp* denote the values determined numerically and the ones obtained experimentally, respectively.

The second step, whose initial values are the ones obtained in the first step, aims to minimise the difference between the magnitude of the measured FRF and the numerical one, resulting in a minimisation function as the one in equation (5.18). An illustration of the second step is represented in figure 5.1b.

$$f_2 = \int_f (FRF_{exp} - FRF_{num})^2 \mathrm{d}f, \tag{5.18}$$

The function f_2 is written as an integral over the whole frequency range in order to overcome the error associated with frequencies where the ratio between the response function and experimental noise is small. Since the function FRF_{exp} is a set of discrete values of magnitude evaluated at discrete values of frequency, the integral is solved numerically according to the following equation:

$$f_2 = \sum_{s=1}^{n-1} \frac{\omega_{s+1} + \omega_s}{2} [\kappa(\omega_{s+1}) + \kappa(\omega_s)], \tag{5.19}$$

where n is the number of discrete frequencies in which the experimental function is defined and $\kappa(\omega)$ is expressed in the following equation:

$$\kappa(\omega) = (FRF_{exp}(\omega) - FRF_{num}(\omega))^2. \tag{5.20}$$

From equation (5.19) and equation (5.20), it is noticeable that the performance of the method is directly related to the number of discrete experimental frequencies. As such, one can anticipate that as the number of discrete frequencies increases so does the reliability of the minimisation function.

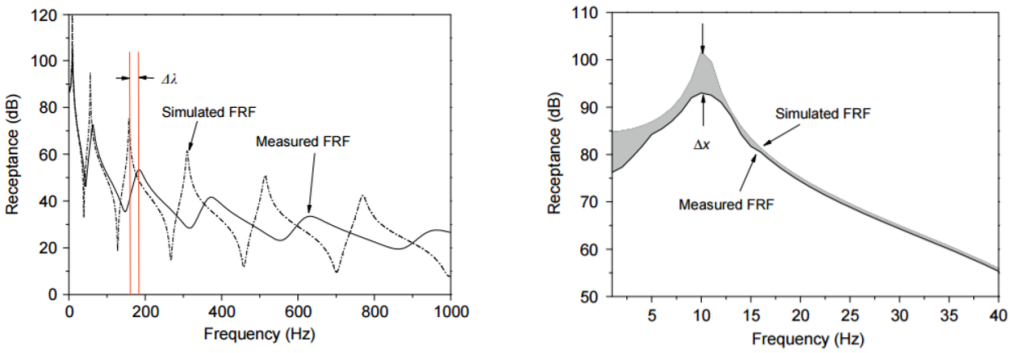

(a) First step. (b) Second step.

Figure 5.1: Two-step identification method (Kim and Lee, 2009).

A flowchart of the identification method is then shown in figure 5.2. The iterative procedure for the determination of the natural frequencies and natural shapes of the composite beam is schematised in figure 5.3.

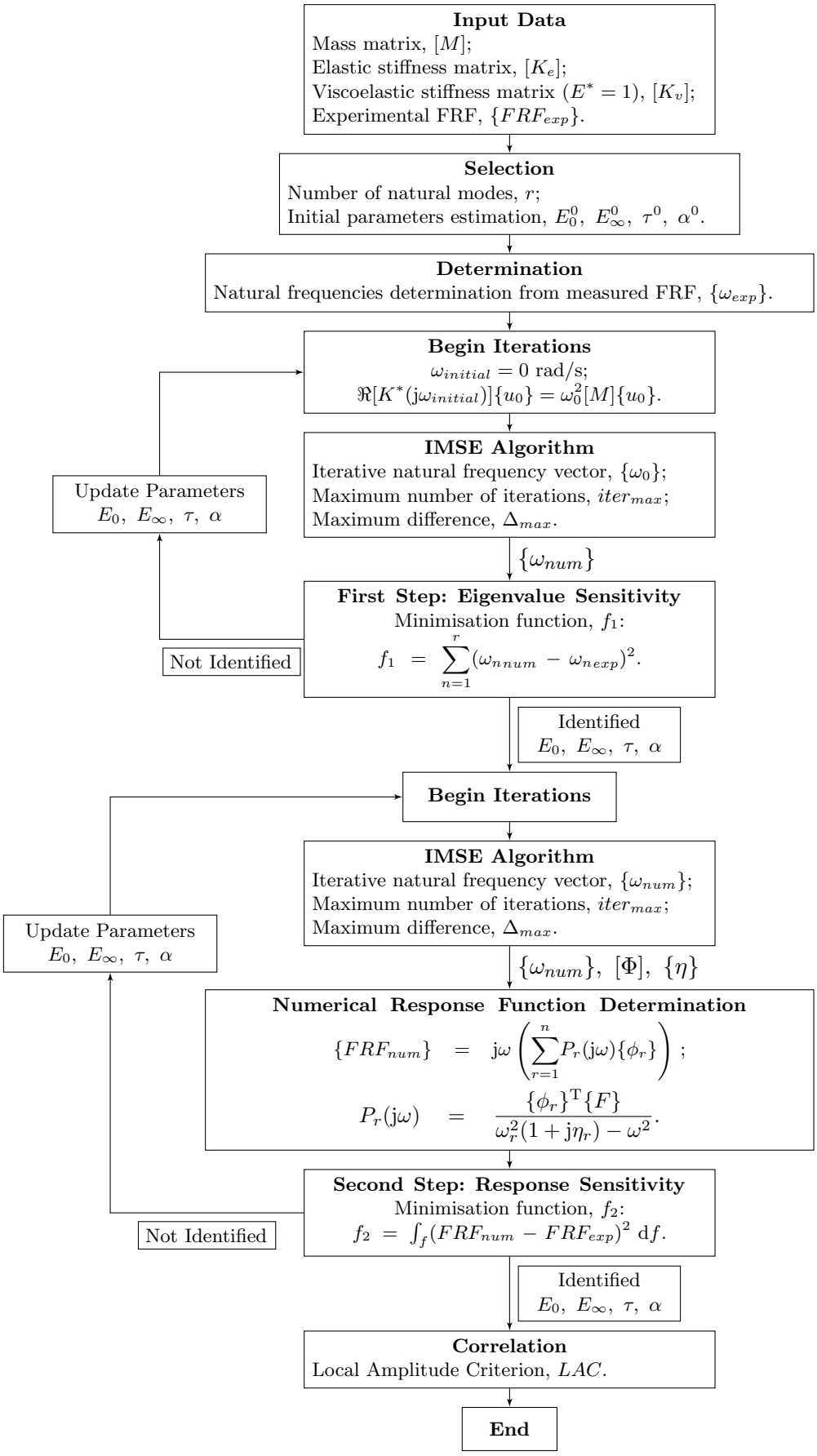

Figure 5.2: Diagram of the two-step identification method.

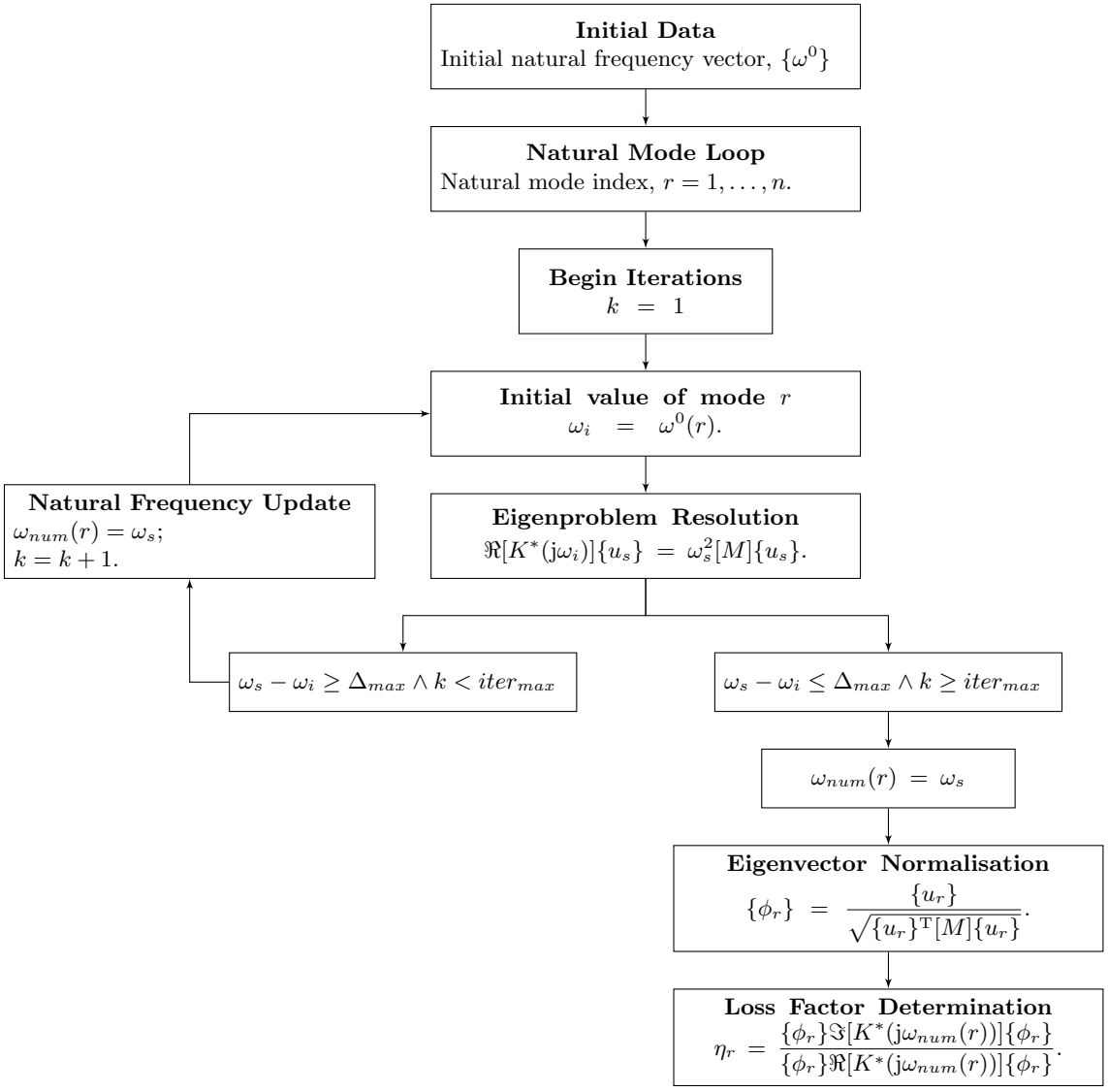

Figure 5.3: Diagram of the IMSE algorithm.

5.5 Optimisation Functions

As stated in the current chapter, the minimisation functions used to perform the first and second steps of the identification process, are the ones available in the software `Matlab`®.

Different minimisation functions are available in both `Optimization Toolbox`® and in the `Global Optimization Toolbox`® however, the ones of most relevance in the current work are *fminseach*, *fmincon* and *patternsearch*. As such, a brief introduction on the behaviour of such functions will be developed in the current chapter.

5.5.1 *fminsearch*

The minimisation function *fminsearch* uses the Nelder-Mead algorithm which attempts to minimise non-linear functions of n variables using only function values. In other words, it does not require any derivative information. It is, then, considered a direct search method.

This method is a simplex based method, which means that in each iteration it evaluates a *convex hull* of $n+1$ vertices defined as: $x_0, ..., x_{n+1} \in \mathbb{R}^n$. For instance, in a $\mathbb{R}^2$ space, the simplex is a triangle and in a $\mathbb{R}^3$ is a tetrahedron (Lagarias et al., 1998).

To fully define the Nelder-Mead algorithm, four parameters must be stated: coefficients of reflection, ρ, expansion, χ, contraction, γ and shrinkage, σ. These coefficients dictate the values calculated in each step of the iterative process and the ones adopted in `Matlab`® are the ones bellow.

$$\rho = 1, \chi = 2, \gamma = \frac{1}{2} \; and \; \sigma = \frac{1}{2}. \tag{5.21}$$

In each iteration k, with $k \geq 0$, of the Nelder-Mead algorithm, the following steps are performed:

Step 1. Ordering and labeling vertices

In the first step the $n+1$ vertices are written in ascending order: $f(x_1) \leq f(x_2) \leq \ldots \leq f(x_{n+1})$. This results in x_1 being the best point and x_{n+1} the worst, since the objective is to minimise $f(x)$. Therefore, the forthcoming steps are performed in order to replace the worst point of the simplex.

Step 2. Reflect

In this step, the reflection point, x_r, is calculated from the following equation:

$$x_r = \bar{x} + \rho(\bar{x} - x_{n+1}), \tag{5.22}$$

where $\bar{x}$ is defined as the centroid of the n best points:

$$\bar{x} = \sum_{i=1}^{n} \frac{x_i}{n}. \tag{5.23}$$

If $f(x_1) \leq f(x_r) < f(x_n)$, the value of x_r is accepted and the iteration ends.

Step 3. Expand

If $f(x_r) < f(x_1)$ the expansion point, x_e is calculated:

$$x_e = \bar{x} + \chi(x_r - x_{n+1}). \tag{5.24}$$

For the case of $f(x_e) < f(x_r)$, x_e is accepted and the iteration ends. If not, x_r is accepted and the iteration is terminated.

Step 4. Contract

If $f(x_r) \geq f(x_n)$ perform a contraction step, which can be an *outside contraction* or an *inside contraction*.

1. Outside Contraction
   If $f(x_n) \leq f(x_r) < f(x_{n+1})$ calculate x_c as follows:

$$x_c = \bar{x} + \gamma(x_r - \bar{x}). \tag{5.25}$$

   If $f(x_c) \leq f(x_r)$, x_c is accepted and the iteration finishes. Otherwise, a shrink step must be performed.

2. Inside Contraction
   If $f(x_r) \geq f(x_{n+1})$ calculate x_{cc} as follows:

$$x_{cc} = \bar{x} - \gamma(\bar{x} - x_{n+1}) \tag{5.26}$$

   If $f(x_{cc}) \leq f(x_r)$, x_{cc} is accepted and the iteration concludes. Otherwise, a shrink step must be performed.

Step 5. Perform a shrink step
Performing a shrink test implies that only the best point in the current iteration will continue to the next. The new n points are determined as follows:

$$v_i = x_1 + \sigma(x_i - x_1),\ i = 2, \ldots, n+1. \tag{5.27}$$

5.5.2 *fmincon*

Fmincon is a constrained gradient-based minimisation function. It is available with multiple algorithms, however, the one used is the recommended Interior Point Algorithm. The rather complex mathematical formulation of the Interior Point Algorithm, that lies outside the scope of the current work, will be avoided and merely a brief reference will be performed.

The original minimisation function, $f(x)$, submitted to equality and inequality constraints of $h(x) = 0$ and $g(x) \leqslant 0$, is transformed in a series of approximate minimisation functions as follows:

$$\underset{x,s}{min}\, f_\mu(x, s) = \underset{x,s}{min}\, f(x) - \mu \sum_{i=1}^{m} \ln(s_i). \tag{5.28}$$

The above written problem only possesses equality constraints in the form of $h(x) = 0$ and $g(x) + s = 0$. The number of slack variables, s, is, then, equal to the number of inequality constraints. The coefficient μ, is a small scalar value that when close to zero, the minimisation of the approximate problem tends to the minimisation of the original problem.

The solution of the barrier problem is characterised by introducing the Lagrangian of equation (5.28) and the optimal solution is achieved when the gradient of the Lagrangian function is null. In (Byrd et al., 1999) the interior point algorithm is thoroughly explained.

As is noticeable, the application of *fmincon* requires that both the minimisation function and constraints are continuous and possess continuous first derivatives. Using the Interior Point Algorithm in `Matlab`® allows that both gradient vector and hessian matrix are obtained numerically using finite differences methods.

5.5.3 *patternsearch*

Patternsearch is a direct search minimisation function and therefore does not require the calculation of the first or even higher order derivatives of the minimisation function. In order to find a minimum value of the objective function it uses an adaptative mesh algorithm.

At each iteration, k, a finite number of trial points are generated which belong necessarily to the feasible region, Ω. For an unconstrained minimisation problem, the feasible region corresponds to $\mathbb{R}^n$. However, when the problem has linear or inequality constrains the domain can be defined as $\Omega \subset \mathbb{R}^n$. The objective of each iteration is to find a trial point with a lower function value than the current iteration value, which is the best objective function value so far. All trial points belong to a mesh which is constructed at each iteration and scaled by a mesh size parameter, Δ_k^m.

The evaluation of f_Ω at a trial point starts with testing if x belongs to Ω, if x lies outside Ω, the value $f_\Omega(x)$ is set to $+\infty$ without evaluating the function. On the other hand, if $x \in \Omega$, the function value is calculated. There are two steps in each iteration: the search step and the poll step. In the first one, a number of feasible points are evaluated and when an improved point is generated the iteration either stops or continues in order to find a better improved solution. The next iteration begins with the new iteration solution and a mesh size parameter equal to or bigger than the ones previously defined. If the algorithm fails to find an improved mesh point, the poll step is performed. In this step, the barrier function is evaluated in points in the vicinity of the mesh points to see if a lower function value is found. If the algorithm does not succeed, the mesh is refined in order to increase the mesh size resolution and to evaluate the barrier function in points closer to the solution of the previous iteration. (Audet and Dennis Jr, 2006).

5.6 Correlation Indicator

The frequency response functions generated numerically and obtained experimentally can be quantitatively and objectively compared using correlation indicators. The one used in the present work is the *Local Amplitude Criterion* (LAC).

This criterion allows to determine the closeness between the two response functions as well as to distinguish between frequency regions of good and poor correlation (Zang et al., 2001). It returns a real value in the range of [0 1], indicating zero-total correlation. It can be determined with the following equation:

$$LAC_{jl}(\omega) = \frac{2|\{\alpha_{jl_{num}}(\omega)\}^H \{\alpha_{jl_{exp}}(\omega)\}|}{\{\alpha_{jl_{num}}(\omega)\}^H \{\alpha_{jl_{num}}(\omega)\} + \{\alpha_{jl_{exp}}(\omega)\}^H \{\alpha_{jl_{exp}}(\omega)\}}, \tag{5.29}$$

where $\{\alpha_{jl_{num}}(\omega)\}$ and $\{\alpha_{jl_{exp}}(\omega)\}$ are the frequency response functions, obtained numerically and experimentally, respectively, of the j degree of freedom relative to the application of a load in the l degree of freedom. The index H denotes the transpose complex conjugate of the vector.

Chapter 6

Two-Step Identification Method Application

6.1 Introduction

In the current chapter, the developed algorithm is applied to determine the mechanical properties of aluminium as well as the fractional derivative model parameters, which consequently lead to the dynamic properties of the viscoelastic material.

For the composite beams, the algorithm is evaluated using distinct minimisation functions available in `Matlab`® and explained in previous chapters: *fminsearch*, which is an unconstrained gradient-free function that uses the Nelder-Mead simplex algorithm; *fmincon*, which is a gradient-based function that uses the interior-point algorithm and *patternsearch*, which is a direct search algorithm that does not require the gradient or even derivatives of a higher order of the function, it merely evaluates a set of points around the current iteration point to find a lower value of the minimisation function.

6.2 Base beam results

To determine the base beam properties, which are the modulus of elasticity, E, and the loss factor, η, a few modifications are performed on the algorithm previously mentioned. These alterations included the analysis of the complex stiffness matrix as frequency independent and solving the eigenproblem recurring to a Modal Strain Energy (MSE) approach. This method assumes that the modes obtained from the undamped system are representative of the damped system, which is not a poor approximation given that aluminium is a lightly damped material (Vasques et al., 2010a).

For the finite element model, the beam is discretised using 45 elements, which results in elements with 4 mm of length. The points of impact are carefully selected, detailed in previous chapters, to ensure that it corresponds to a node of the discrete beam.

The properties of aluminium are fairly known and the ones most currently used are taken as the initial parameters which are summarised in table 6.1.

Table 6.1: Initial parameters for the identification method for the bare beam.

Parameter	Value
E /Pa	69×10^9
η	1×10^{-3}

For the bare beam minimisation process, the first step is evaluated using the function *patternsearch* and the second step is evaluated using *fmincon*. In both steps, the problem is intro-

duced as a semi-constrained one, where properties are defined as non-null positive values.

The minimisation process is performed using the frequency response functions obtained by measuring the velocity in the free end of the beam and applying the impact in 3 different points. The results for each FRF are shown in the subsequent sections.

6.2.1 $FRF_{180,44}$

The parameters obtained using $FRF_{180,44}$ on the identification method are summarised in table 6.2.

Table 6.2: Identified base beam properties using the $FRF_{180,44}$.

Parameter	First Step	Second Step
E /Pa	61.2023×10^9	61.2023×10^9
η	8.6784×10^{-4}	3.3315×10^{-3}

The experimental and identified response functions are shown in figure 6.1 and the local amplitude criterion is plotted in figure 6.2 .

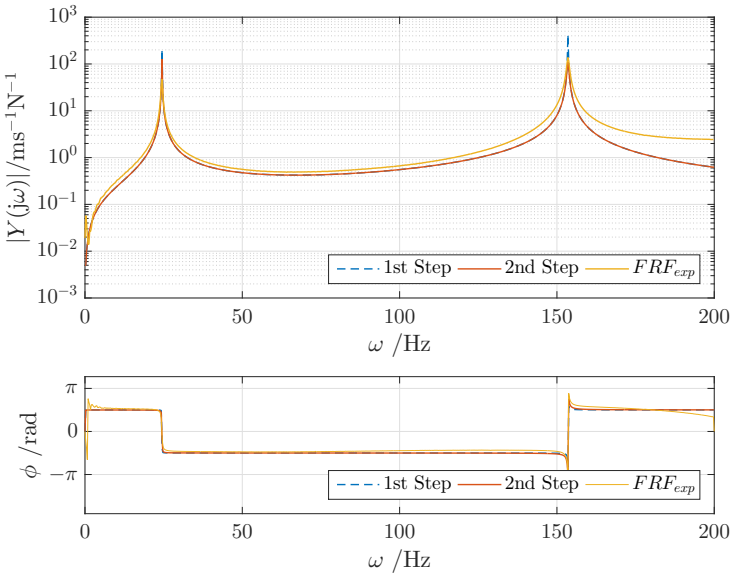

Figure 6.1: Experimental and identified $FRF_{180,44}$.

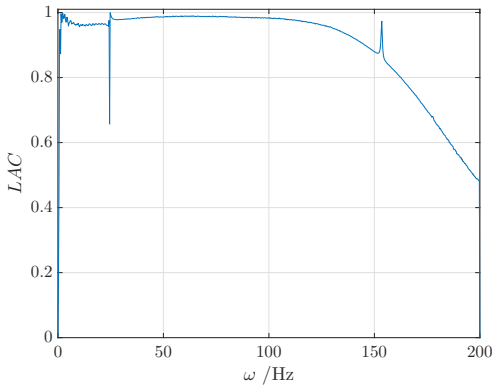

Figure 6.2: LAC for the $FRF_{180,44}$.

6.2.2 $FRF_{180,108}$

The identified parameters of the fractional derivative in both first and second step of the method are present in table 6.3.

Table 6.3: Identified base beam properties using the $FRF_{180,108}$.

Parameter	First Step	Second Step
E /Pa	61.2024×10^9	61.2024×10^9
η	1.0879×10^{-3}	8.3546×10^{-3}

The representation of the synthesised FRF and the one determined through experiment is shown in figure 6.3. The quantitative comparison performed adopting the local amplitude criterion is illustrated in figure 6.4.

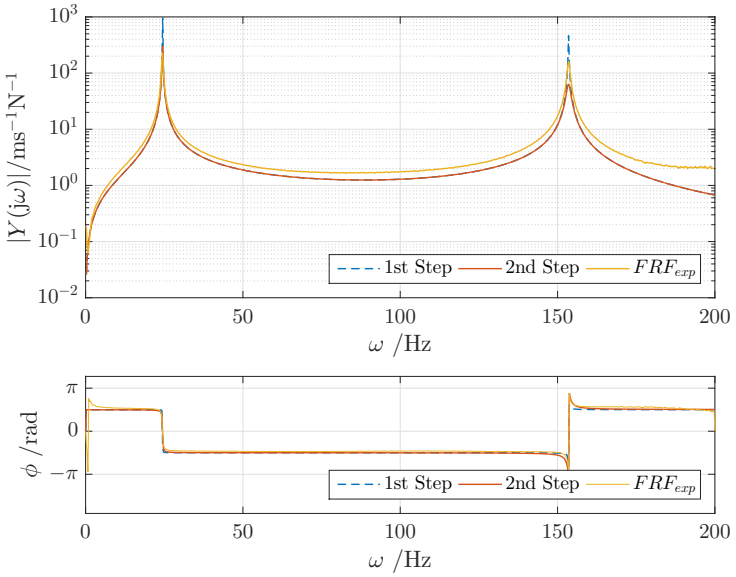

Figure 6.3: Experimental and identified $FRF_{180,108}$.

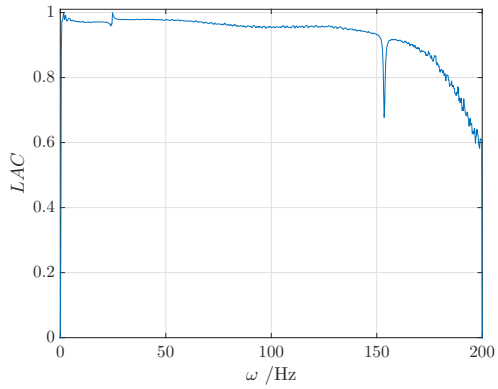

Figure 6.4: LAC for the $FRF_{180,108}$.

6.2.3 $FRF_{180,180}$

Using the direct FRF leads to the following parameters:

Table 6.4: Identified base beam properties using the $FRF_{180,180}$.

Parameter	First Step	Second Step
E /Pa	61.2024×10^9	61.2024×10^9
η	1.3160×10^{-3}	1.4643×10^{-2}

The graphic validation of the results is shown in table 6.4 is illustrated in figure 6.5. The resulting LAC is represented in figure 6.6.

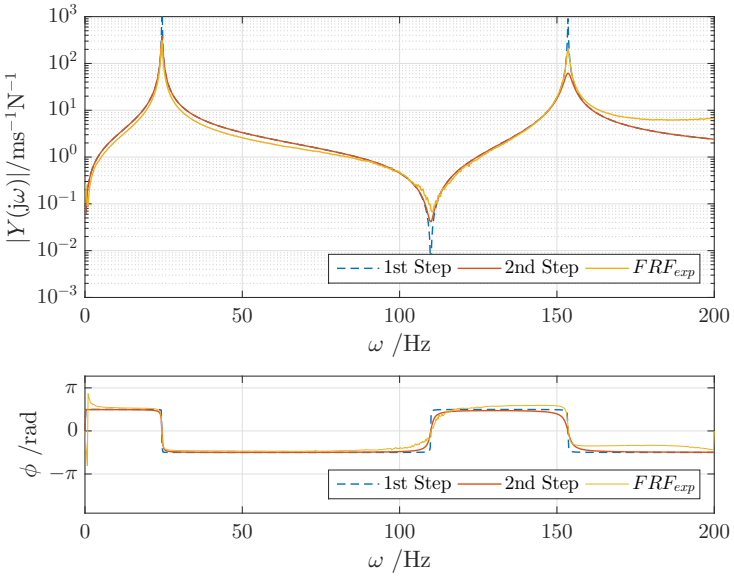

Figure 6.5: Experimental and identified $FRF_{180,180}$.

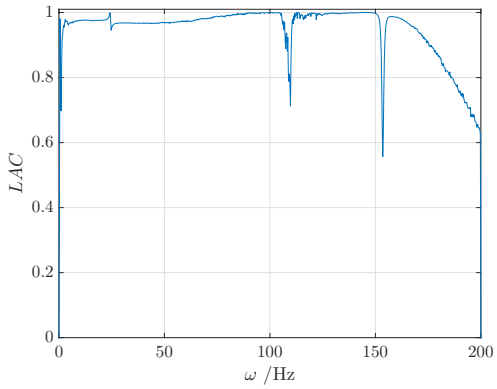

Figure 6.6: LAC for the $FRF_{180,180}$.

6.2.4 Notes on the bare beam results

For the minimisation process, even though only the results of one combination of minimisation functions are shown, several tests were performed. The results obtained were coincident, and the parameters values numerically similar.

Evaluating the numeric results obtained using the 3 distinct FRFs, is noticeable an exact agreement on the values of the modulus of elasticity, E, whereas the loss factor, η, shows a small discrepancy on the 3 functions. It is also visible that in the first step, the value of E is identified and the second step adjusts the amplitude by merely modifying the loss factor. Such occurrence is an expected consequence given the fact that is the damping that is responsible for the amplitude changes in the resonance bandwidths.

The results obtained using the Local Amplitude Criterion show a smaller concordance of the synthesised and experimental FRF on the second mode of vibration. This result can be explained by the use of modal superposition principle to numerically generate the FRF: where an increase in the number of modes considered leads to an improvement on the results of the preceding modes.

Lastly, the values selected for the base beam properties represent the mean values of the ones obtained in the 3 minimisation processes and are summarised in table 6.5.

Table 6.5: Determined properties of the aluminium bare beam.

Parameter	Value
E /Pa	61×10^9
η	4×10^{-3}

6.3 Composite beam results

For the application of the minimisation algorithm on the composite beams, the initial parameters chosen are the ones present in table 6.6.

Table 6.6: Initial parameters for the identification method for the composite beams.

Parameter		Value
E_0	/Pa	1×10^6
E_∞	/Pa	1×10^9
τ	/s	1×10^{-7}
α		5×10^{-1}

Choosing the aforementioned parameters is a result of several attempts on the performance of the algorithm conjointly with the satisfaction of the thermodynamic constraints of the parameters established in (Bagley and Torvik, 1986) and summarised bellow:

1. $E_0, E_\infty, \tau, \alpha > 0$;
2. $E_\infty > E_0$;
3. $\alpha < 1$.

For the finite element model, the beams are divided into 4 mm long elements, resulting in 45, 55 and 65 elements for the sample A, sample B and sample C, respectively.

Distinct minimisation functions available in `Matlab`® are tested for the 1st and 2nd steps of the identification method. The minimisation functions used in both steps are summarised in table 6.7.

Table 6.7: Minimisation functions adopted for the evaluation of the 2 Steps.

	1st Step	2nd Step
1	*fminsearch*	*fmincon*
2	*fmincon*	*patternsearch*
3	*patternsearch*	*patternsearch*

The selection of these functions is a longstanding process given the wide range of functions available. Applying a minimisation function that uses a gradient-based algorithm in both steps of the process shows unimpressive results as a consequence of the poorly scaled parameters. As such, choosing to evaluate one of the steps using a gradient-free function seems a fitted alternative. Thus, as shown above, 3 alternatives are selected: one that uses an unconstrained gradient-free function in the first step and a gradient-based function in the second step; one that uses a gradient-based function in the first step and a gradient-free in the second step and the last that evaluates both steps using a direct search function. It is also noticeable that the second step should preferably be implemented using constrained minimisation functions, leading to negative parameters otherwise.

When gradient-based functions are considered, both gradient vector and hessian matrix are calculated numerically through finite differences method, using a step size of 0.01% of the parameter's values.

6.3.1 Composite Beam A

For the application of the identification method on the composite beam A, two vibration modes are considered. Even though the experimental functions are obtained in a frequency bandwidth

of [0 400] Hz, as previously mentioned, it is verified through experiment that the implementation of the second step leads to better results when the frequency bandwidth considered for the integration process does not include frequencies much higher than the last natural mode considered.

This verification is related to the fact that the FRF is obtained using a superposition of natural modes. It is fairly known that the effect of a given mode of vibration is more evident in the vicinity of its natural frequency. Therefore, deviating from such frequency implies an increasing influence of the preceding or following modes of vibration, depending if the deviation is to lower or higher frequencies than the natural frequency considered.

Bearing such in mind, the integration of the minimisation function in the second step of the identification process, is performed in a frequency bandwidth whose superior limit is not far superior than the natural frequency of the last mode considered. For the current composite beam a frequency bandwidth of [0 300] Hz is selected.

1st Step: *fminsearch*, 2nd Step: *fmincon*

As previously stated, three FRF are obtained for the composite beam A, with different points of impact. The values obtained for the parameters using the $FRF_{180,80}$, are described in table 6.8.

Table 6.8: Identified parameters using the $FRF_{180,80}$ and functions *fminsearch* and *fmincon* for the first and second steps, respectively.

Parameter		First Step	Second Step
E_0	/Pa	2.1874×10^{6}	2.1874×10^{6}
E_∞	/Pa	4.0441×10^{9}	4.0441×10^{9}
τ	/s	1.3379×10^{-16}	1.3379×10^{-16}
α		2.2513×10^{-1}	2.2513×10^{-1}

In figure 6.7, are illustrated the synthesised and the experimental FRFs and in figure 6.8, is performed the comparison of the two functions recurring to LAC criterion.

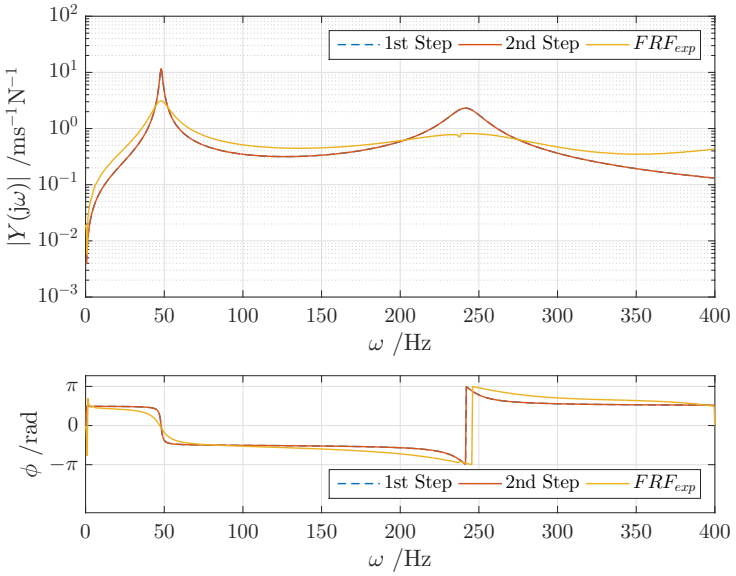

Figure 6.7: Experimental and identified $FRF_{180,80}$ using functions *fminsearch* and *fmincon* for the first and second steps, respectively.

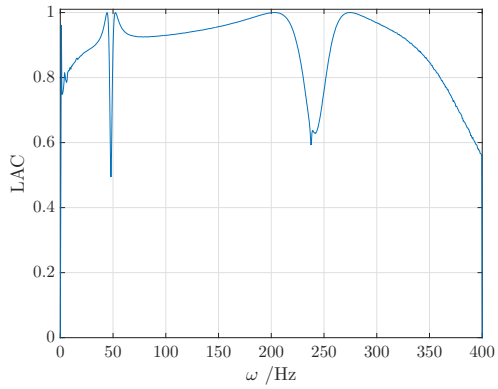

Figure 6.8: LAC for the $FRF_{180,80}$ using functions *fminsearch* and *fmincon* for the first and second steps, respectively.

Using $FRF_{180,108}$ for the minimisation process conducts to the results shown in table 6.9.

Table 6.9: Identified parameters using the $FRF_{180,108}$ and functions *fminsearch* and *fmincon* for the first and second steps, respectively.

Parameter		First Step	Second Step
E_0	/Pa	2.0601×10^6	2.0601×10^6
E_∞	/Pa	1.6868×10^8	1.6868×10^8
τ	/s	1.0413×10^{-8}	6.4812×10^{-9}
α		2.8889×10^{-1}	2.9102×10^{-1}

In figure 6.9 are depicted the experimental and synthesised functions obtained and in figure 6.10 the result of the LAC criterion evaluation.

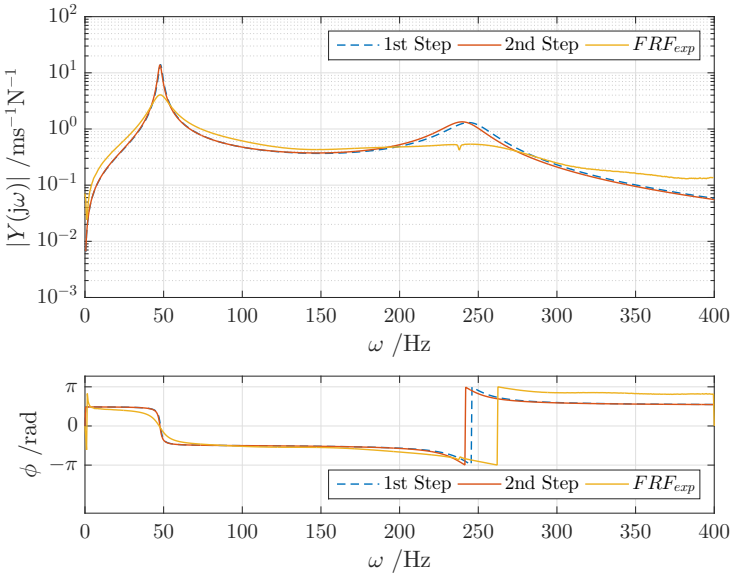

Figure 6.9: Experimental and identified $FRF_{180,108}$ using functions *fminsearch* and *fmincon* for the first and second steps, respectively.

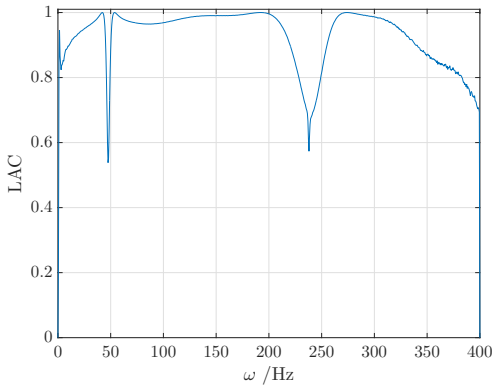

Figure 6.10: LAC for the $FRF_{180,108}$ using functions *fminsearch* and *fmincon* for the first and second steps, respectively.

Using the direct frequency response function, the results for the parameters are shown in table 6.10.

Table 6.10: Identified parameters using the $FRF_{180,180}$ and functions *fminsearch* and *fmincon* for the first and second steps, respectively.

Parameter		First Step	Second Step
E_0	/Pa	2.0563×10^6	2.0563×10^6
E_∞	/Pa	6.2235×10^8	6.2235×10^8
τ	/s	4.2885×10^{-7}	4.2885×10^{-7}
α		5.4561×10^{-1}	5.4561×10^{-1}

As for the FRFs obtained, they are shown in figure 6.11 and the comparison between the experimental function and the numerically generated one is evidenced in figure 6.12.

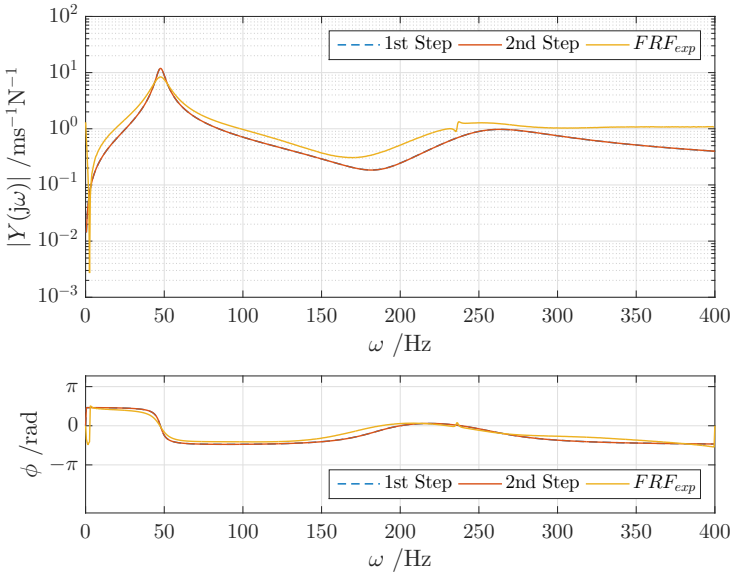

Figure 6.11: Experimental and identified $FRF_{180,180}$ using functions *fminsearch* and *fmincon* for the first and second steps, respectively.

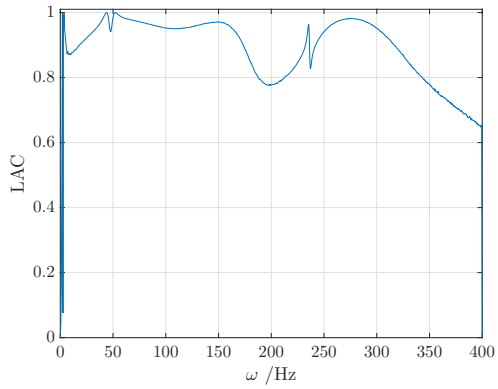

Figure 6.12: LAC for the $FRF_{180,180}$ using functions *fminsearch* and *fmincon* for the first and second steps, respectively.

Analysing the results mentioned above, it is noticeable that from the first step to the second step of the minimisation process, little or no change occurs in the numeric values of the parameters. The *fmincon* algorithm stops even though the minimisation function does not reach small values, which could be caused by the non-smoothness of the minimisation function and the presence of a local minimum. The three synthesised functions evidence lower correlation levels in the resonance bandwidth and, on the case of the direct FRF, on the antiresonance bandwidth also, resulting in the underestimate of the loss factor of the material.

It is also perceptible that the results differ quite substantially when different FRF are used in the minimisation process, which invalidates the parameters obtained as well as the resultant frequency dependent properties of the viscoelastic material.

The mentioned behaviour is observed for all composite beams using this two minimisation functions. As such, for reference, the results obtained for the remaining composite beams are presented in Appendix B.

1st Step: *fmincon*, 2nd Step: *patternsearch*

Evaluating the first step using *fmincon* and the second step using *patternsearch* leads to the results present in the current section.

Using $FRF_{180,80}$ for the identification process conducted, in each step, to the parameters shown in table 6.11.

Table 6.11: Identified parameters using the $FRF_{180,80}$ and functions *fmincon* and *patternsearch* for the first and second steps, respectively.

Parameter		First Step	Second Step
E_0	/Pa	1.0000×10^{6}	1.4622×10^{6}
E_∞	/Pa	1.0000×10^{9}	3.1735×10^{8}
τ	/s	5.5803×10^{-7}	5.5803×10^{-7}
α		6.2867×10^{-1}	4.9586×10^{-1}

The FRFs generated and experimentally obtained can be seen in figure 6.13 and compared using LAC in figure 6.14.

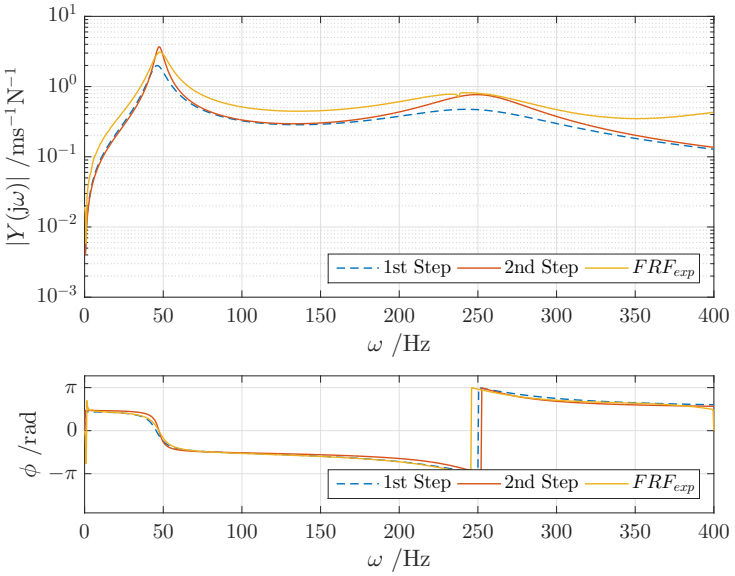

Figure 6.13: Experimental and identified $FRF_{180,80}$ using functions *fmincon* and *patternsearch* for the first and second steps, respectively.

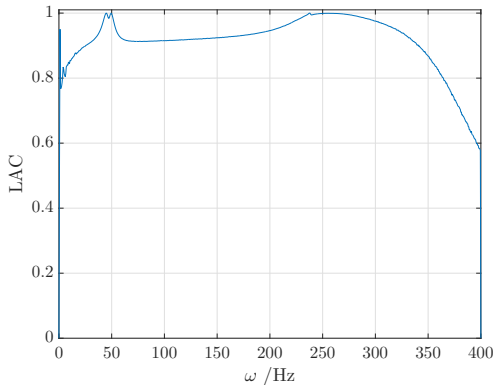

Figure 6.14: LAC for the $FRF_{180,80}$ using functions *fmincon* and *patternsearch* for the first and second steps, respectively.

The results reached for the fractional derivative parameters when using $FRF_{180,108}$ are shown in table 6.12.

Table 6.12: Identified parameters using the $FRF_{180,108}$ and functions *fmincon* and *patternsearch* for the first and second steps, respectively.

Parameter		First Step	Second Step
E_0	/Pa	1.0000×10^6	1.4540×10^6
E_∞	/Pa	1.0000×10^9	1.0474×10^9
τ	/s	3.9301×10^{-7}	3.9301×10^{-7}
α		5.9744×10^{-1}	5.7791×10^{-1}

The resultant FRF is represented in figure 6.15 and the LAC criterion is shown in figure 6.16.

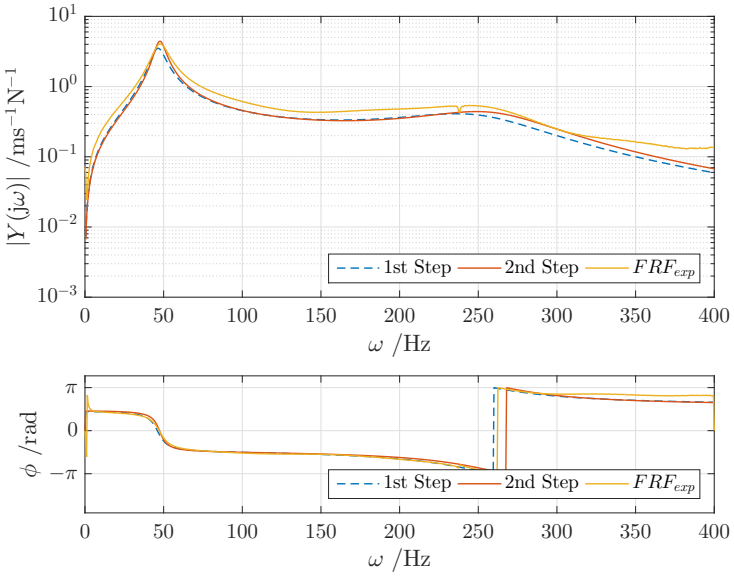

Figure 6.15: Experimental and identified $FRF_{180,108}$ using functions *fmincon* and *patternsearch* for the first and second steps, respectively.

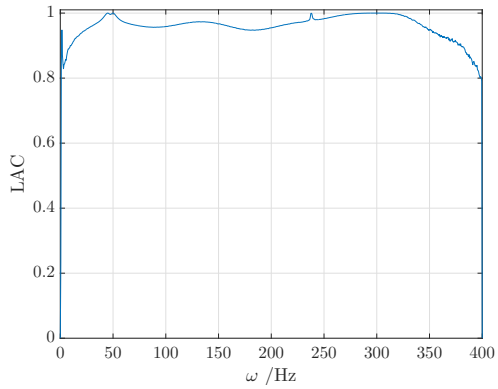

Figure 6.16: LAC for the $FRF_{180,108}$ using functions *fmincon* and *patternsearch* for the first and second steps, respectively.

The parameters obtained using the direct frequency response function are displayed in table 6.13.

Table 6.13: Identified parameters using the $FRF_{180,180}$ and functions *fmincon* and *patternsearch* for the first and second steps, respectively.

Parameter		First Step	Second Step
E_0	/Pa	1.0000×10^{6}	1.2835×10^{6}
E_∞	/Pa	1.0000×10^{9}	6.9578×10^{8}
τ	/s	3.6573×10^{-7}	3.6573×10^{-7}
α		5.7329×10^{-1}	5.4594×10^{-1}

The FRFs are evidenced in the graph of figure 6.17 and the LAC criterion is depicted in figure 6.18.

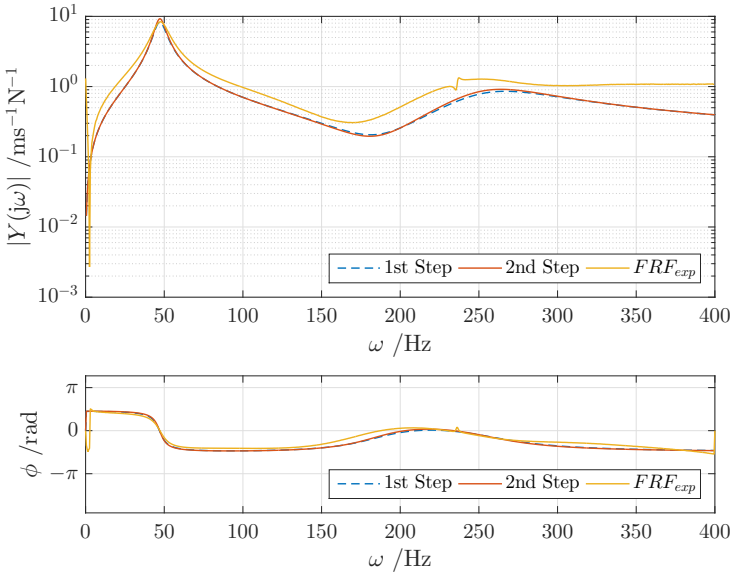

Figure 6.17: Experimental and identified $FRF_{180,180}$ using functions *fmincon* and *patternsearch* for the first and second steps, respectively.

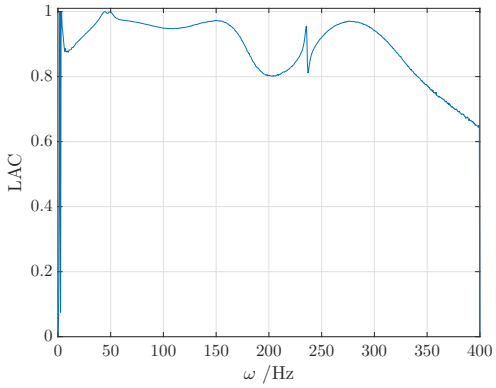

Figure 6.18: LAC for the $FRF_{180,180}$ using functions *fmincon* and *patternsearch* for the first and second steps, respectively.

1st Step: *patternsearch*, 2nd Step: *patternsearch*

The application of global search functions in both steps of the minimisation process leads to the results shown in the current section.

The results obtained using $FRF_{180,80}$ are listed in table 6.14.

Table 6.14: Identified parameters using the $FRF_{180,80}$ and the function *patternsearch* for both steps of the minimisation process.

Parameter		First Step	Second Step
E_0	/Pa	4.3597×10^6	1.0670×10^6
E_∞	/Pa	1.1661×10^8	2.0179×10^8
τ	/s	1.0000×10^{-6}	1.0000×10^{-6}
α		5.0000×10^{-1}	4.6484×10^{-1}

The representation of the FRFs is presented in figure 6.19 and the result of the application of the local amplitude criterion is shown in figure 6.20.

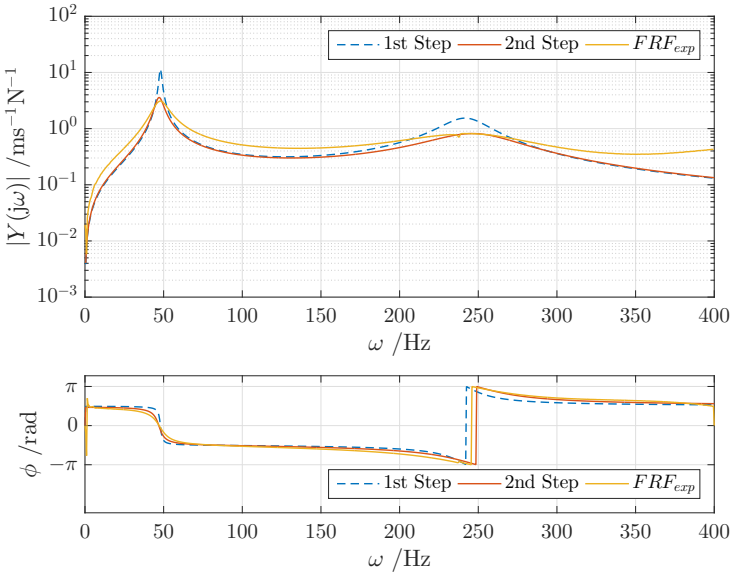

Figure 6.19: Experimental and identified $FRF_{180,80}$ using *patternsearch* for the evaluation of both steps of the minimisation process.

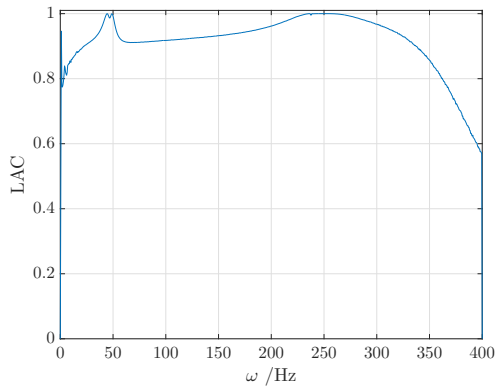

Figure 6.20: LAC for the $FRF_{180,80}$ using the function *patternsearch* for for both, first and second steps.

The results obtained using $FRF_{180,108}$ on the identification method are shown in table 6.15, and the plot of the resulting functions and the LAC are depicted in figure 6.21 and figure 6.22, respectively.

Table 6.15: Identified parameters using the $FRF_{180,108}$ and the function *patternsearch* in both steps.

Parameter		First Step	Second Step
E_0	/Pa	3.9664×10^6	4.1212×10^5
E_∞	/Pa	1.5167×10^8	3.6247×10^8
τ	/s	1.0000×10^{-6}	1.0000×10^{-6}
α		5.0000×10^{-1}	4.9948×10^{-1}

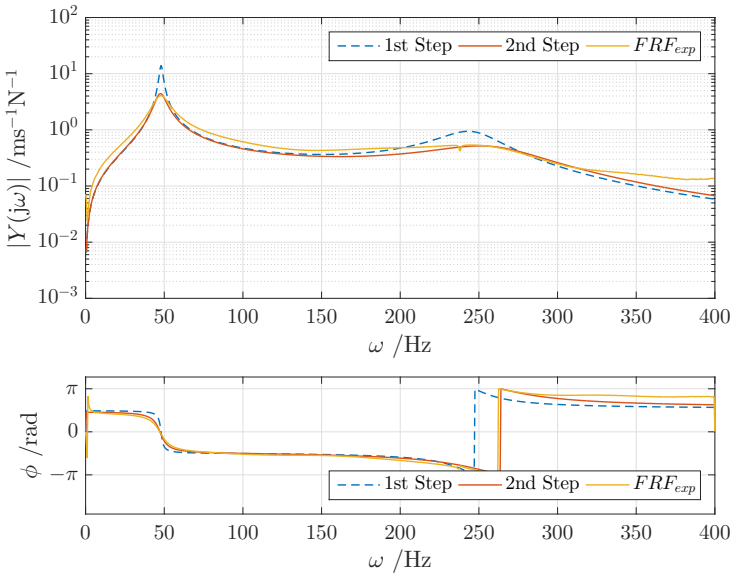

Figure 6.21: Experimental and identified $FRF_{180,108}$ using the function *patternsearch* in both steps of the minimisation process.

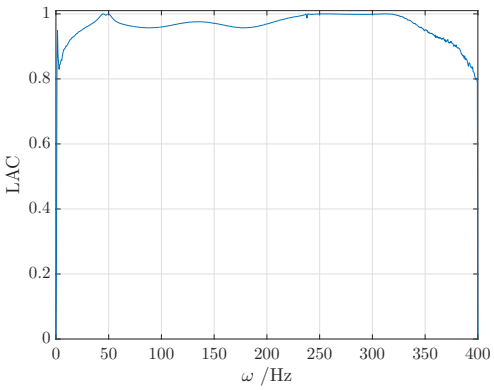

Figure 6.22: LAC for the $FRF_{180,108}$ using *patternsearch* in both steps of the identification process.

The results reached when using the direct frequency response are shown in table 6.16.

Table 6.16: Identified parameters using the $FRF_{180,180}$ and the function *patternsearch* in both steps.

Parameter		First Step	Second Step
E_0	/Pa	1.6069×10^6	6.1157×10^5
E_∞	/Pa	2.8862×10^8	2.7792×10^8
τ	/s	1.0000×10^{-6}	1.0000×10^{-6}
α		5.0000×10^{-1}	4.8730×10^{-1}

The resultant FRF is illustrated in figure 6.23. The quantitative comparison between the experimental and numerical functions is demonstrated in figure 6.24.

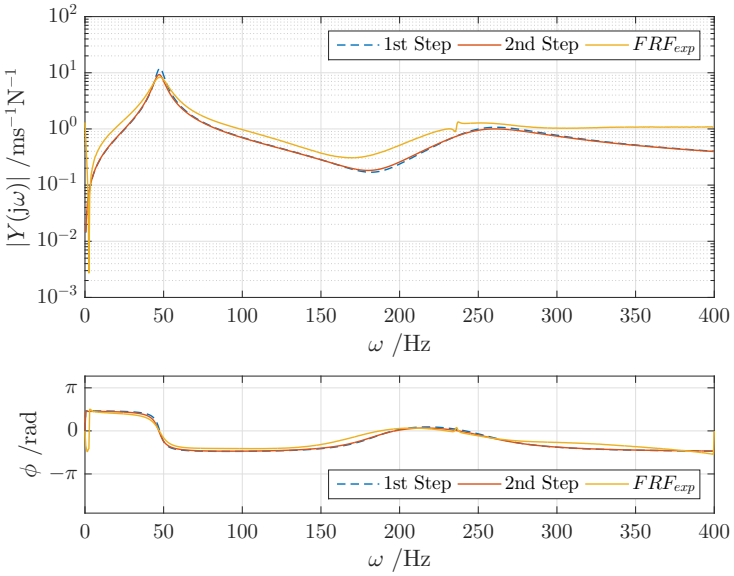

Figure 6.23: Experimental and identified $FRF_{180,180}$ using the function *patternsearch* in both steps of the minimisation process.

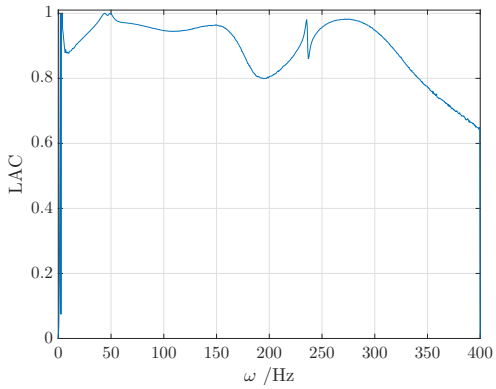

Figure 6.24: LAC for the $FRF_{180,180}$ evaluating both steps using *patternsearch*.

6.3.2 Composite Beam B

Similarly to what was conducted for the composite beam A, two modes of vibration are considered for generating the numerical FRF in the identification method. The integration bandwidth adopted on the second step of the minimisation process is [0 250] Hz.

1st Step: *fmincon*, 2nd Step: *patternsearch*

The parameters obtained using the $FRF_{220,88}$ are written in table 6.17.

Table 6.17: Identified parameters using the $FRF_{220,88}$ and functions *fmincon* and *patternsearch* for the first and second steps, respectively.

Parameter		First Step	Second Step
E_0	/Pa	1.0000×10^{6}	1.3893×10^{6}
E_∞	/Pa	1.0000×10^{9}	7.1752×10^{8}
τ	/s	1.1290×10^{-7}	1.1297×10^{-7}
α		5.1775×10^{-1}	5.0646×10^{-1}

The representation of the experimental and generated FRF is shown in figure 6.25 and the LAC comparison is accomplished in figure 6.26.

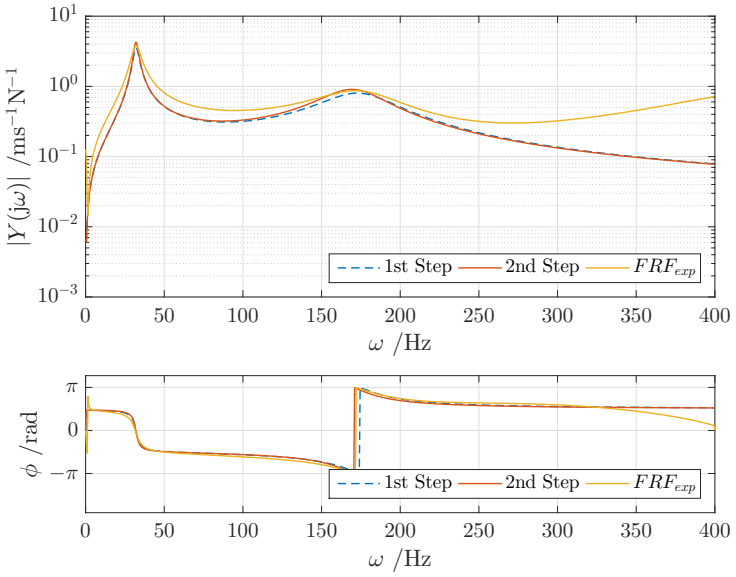

Figure 6.25: Experimental and identified $FRF_{220,88}$ using functions *fmincon* and *patternsearch* for the first and second steps, respectively.

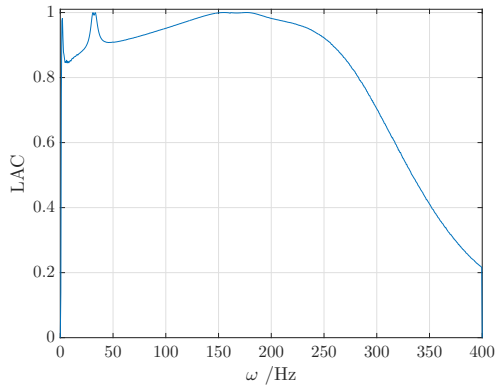

Figure 6.26: LAC for the $FRF_{220,88}$ using functions *fmincon* and *patternsearch* for the first and second steps, respectively.

The $FRF_{220,128}$ leads to the identification of the parameters shown in table 6.18.

Table 6.18: Identified parameters using the $FRF_{220,128}$ and functions *fmincon* and *patternsearch* for the first and second steps, respectively.

Parameter		First Step	Second Step
E_0	/Pa	1.0000×10^6	1.4549×10^6
E_∞	/Pa	1.0000×10^9	6.5834×10^8
τ	/s	3.5708×10^{-7}	3.5708×10^{-7}
α		5.9854×10^{-1}	5.5264×10^{-1}

The FRFs are shown in figure 6.27 and the LAC comparison is performed in figure 6.28.

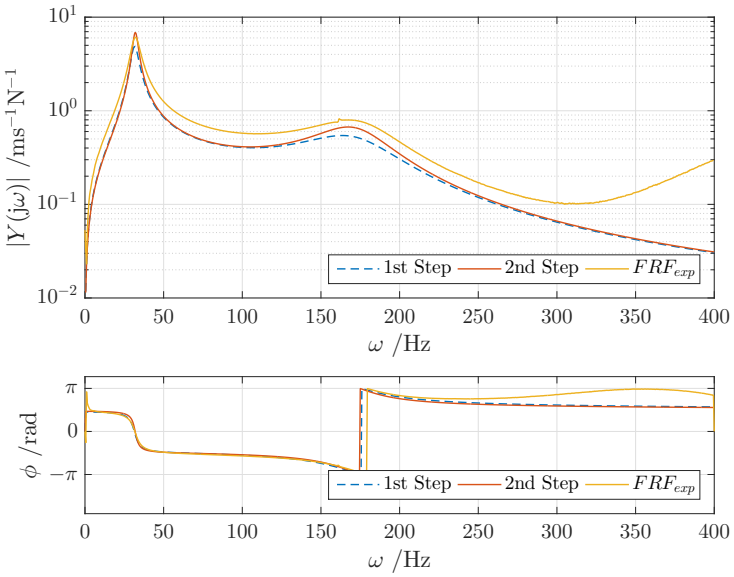

Figure 6.27: Experimental and identified $FRF_{220,128}$ using functions *fmincon* and *patternsearch* for the first and second steps, respectively.

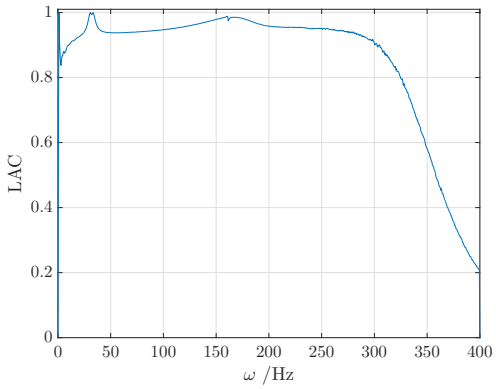

Figure 6.28: LAC for the $FRF_{220,128}$ using functions *fmincon* and *patternsearch* for the first and second steps, respectively.

The direct FRF leads to the fractional derivative parameters shown in table 6.19.

Table 6.19: Identified parameters using the $FRF_{220,220}$ and functions *fmincon* and *patternsearch* for the first and second steps, respectively.

Parameter		First Step	Second Step
E_0	/Pa	1.0000×10^{6}	1.9257×10^{6}
E_∞	/Pa	1.0000×10^{9}	4.6607×10^{8}
τ	/s	5.7859×10^{-7}	5.7859×10^{-7}
α		5.8951×10^{-1}	5.8056×10^{-1}

The mobilities generated numerically and experimentally are shown in figure 6.29. The result after the application of the LAC is shown in figure 6.30.

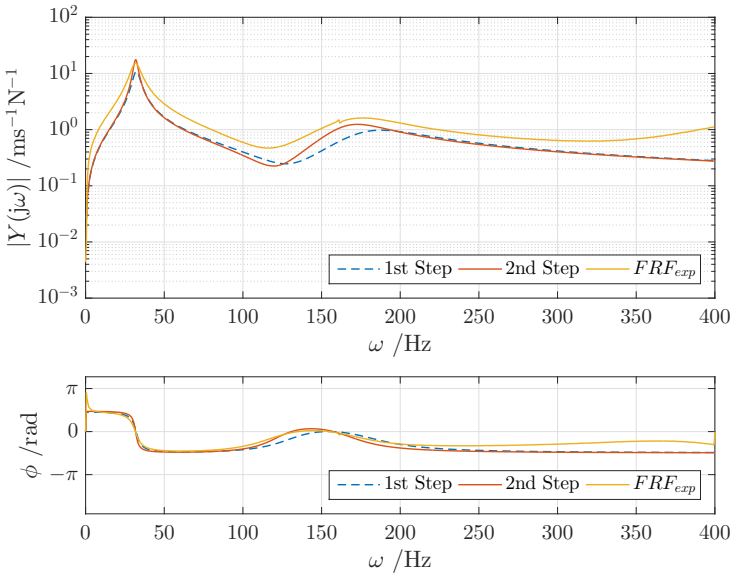

Figure 6.29: Experimental and identified $FRF_{220,220}$ using functions *fmincon* and *patternsearch* for the first and second steps, respectively.

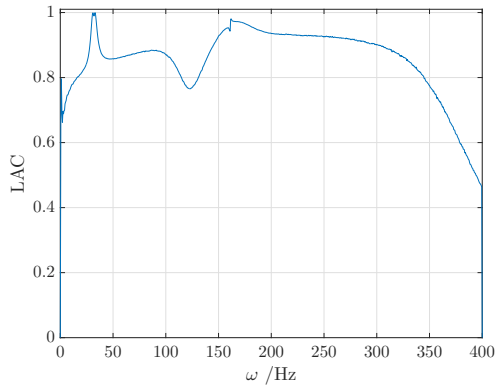

Figure 6.30: LAC for the $FRF_{220,220}$ using functions *fmincon* and *patternsearch* for the first and second steps, respectively.

1st Step: *patternsearch*, 2nd Step: *patternsearch*

The application of a direct search minimisation function in both steps of the process on the experimental data attained of composite beam B, leads to the results listed in the current section.

Using $FRF_{220,88}$ results in the parameters shown in table 6.20. Such parameters generate the FRF represented in figure 6.31. The evaluation of the correlation between the experimental FRF and the synthesised one is illustrated in figure 6.32.

Table 6.20: Identified parameters using the $FRF_{220,88}$ and functions *patternsearch* in both steps.

Parameter		First Step	Second Step
E_0	/Pa	8.4884×10^5	1.2840×10^6
E_∞	/Pa	2.8582×10^8	2.3171×10^8
τ	/s	1.0000×10^{-6}	1.0000×10^{-6}
α		5.0000×10^{-1}	4.9928×10^{-1}

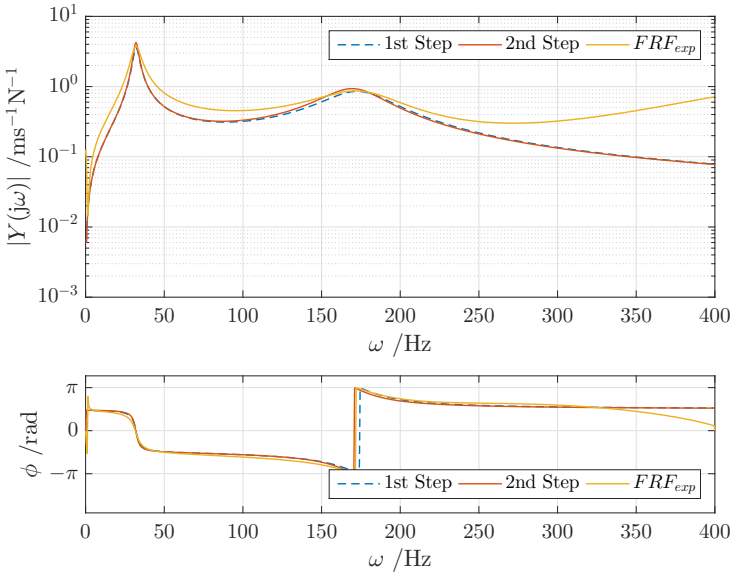

Figure 6.31: Experimental and identified $FRF_{220,88}$ using function *patternsearch* in both steps.

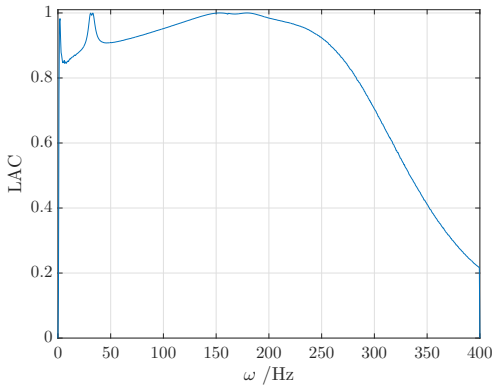

Figure 6.32: LAC for the $FRF_{220,88}$ using function *patternsearch* in both steps.

Using the $FRF_{220,128}$ on the two-step identification method, results in the fractional derivative parameters summarised in table 6.21. The graphical results are depicted in both figure 6.33 and figure 6.34.

Table 6.21: Identified parameters using the $FRF_{220,128}$ and functions *patternsearch* for both steps.

Parameter		First Step	Second Step
E_0	/Pa	1.7046×10^6	9.2798×10^5
E_∞	/Pa	2.0063×10^8	2.4192×10^8
τ	/s	1.0000×10^{-6}	1.0000×10^{-6}
α		5.0000×10^{-1}	4.9025×10^{-1}

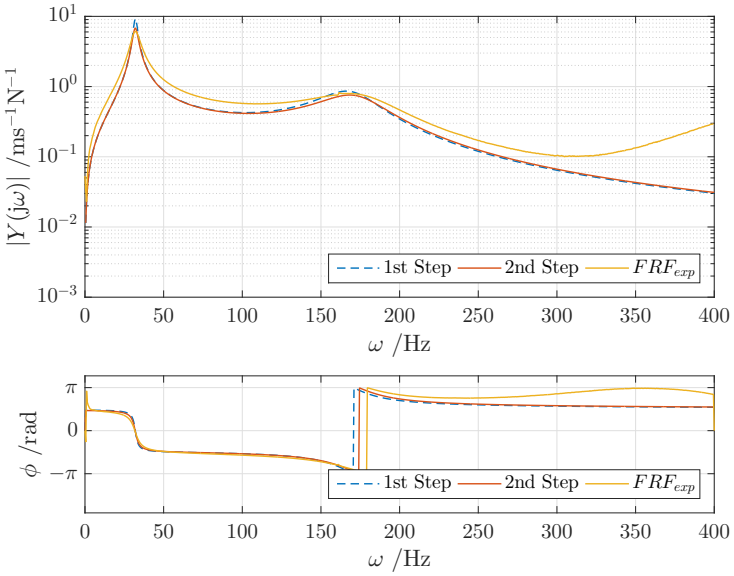

Figure 6.33: Experimental and identified $FRF_{220,128}$ using function *patternsearch* in both steps.

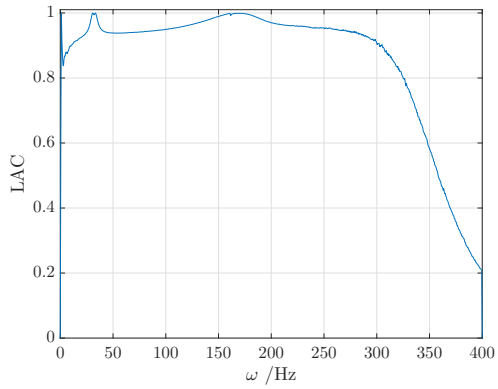

Figure 6.34: LAC for the $FRF_{220,128}$ using function *patternsearch* in both steps.

The application of the direct FRF leads to the numeric results evidenced in table 6.22.

Table 6.22: Identified parameters using the $FRF_{220,220}$ and functions *patternsearch* for both steps.

Parameter		First Step	Second Step
E_0	/Pa	0.0000×10^{0}	1.4526×10^{6}
E_∞	/Pa	3.7938×10^{8}	1.9120×10^{8}
τ	/s	1.0000×10^{-6}	1.0000×10^{-6}
α		5.0000×10^{-1}	4.9687×10^{-1}

The FRFs generated and experimental are shown in figure 6.35. The validation using LAC is evidenced in figure 6.36.

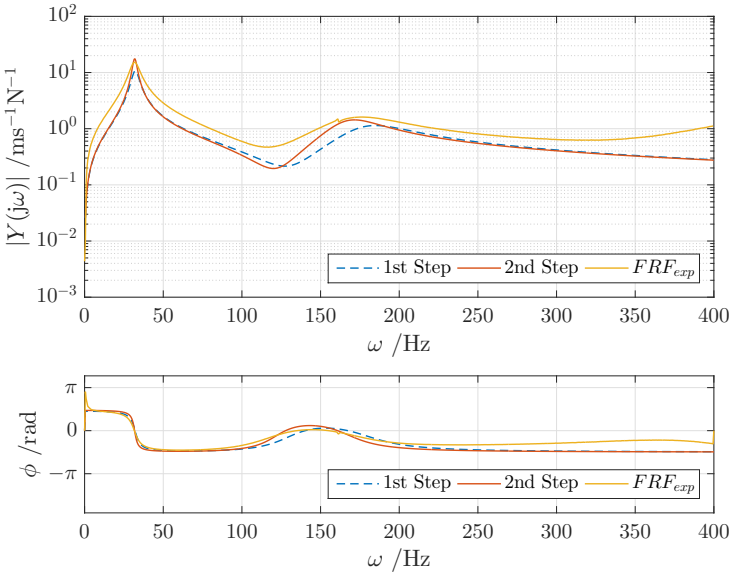

Figure 6.35: Experimental and identified $FRF_{220,220}$ using function *patternsearch* in both steps.

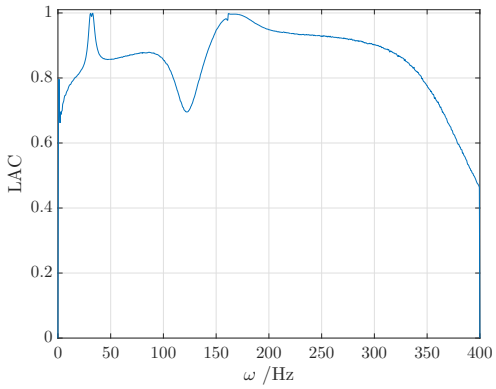

Figure 6.36: LAC for the $FRF_{220,220}$ using function *patternsearch* in both steps.

6.3.3 Composite Beam C

Analogously to the composite beams A and B proceedings, two natural modes of vibration of the composite beam C are used for the identification of the fractional derivative parameters. In the second step, the frequency bandwidth on which the integration of the minimisation function is performed is [0 200] Hz.

The experimental frequency response functions obtained for the composite beam C show a very prominent disturbance around the second mode of vibration, especially on the direct FRF. Such disturbance hinders the exact determination of the second natural frequency, as such, the tendency of the function is assumed and the second natural frequency is estimated visually.

1st Step: *fmincon*, 2nd Step: *patternsearch*

The results of the application of the minimisation function *fmincon* and *patternsearch* for the three FRFs of composite beam C are exposed in the current section.

The parameters obtained with the application of the method on $FRF_{260,108}$ are listed in table 6.23.

Table 6.23: Identified parameters using the $FRF_{260,108}$ and functions *fmincon* and *patternsearch* for the first and second steps, respectively.

Parameter		First Step	Second Step
E_0	/Pa	1.0000×10^6	1.0887×10^6
E_∞	/Pa	1.0000×10^9	7.4921×10^8
τ	/s	7.0328×10^{-8}	7.0328×10^{-8}
α		4.7206×10^{-1}	4.5452×10^{-1}

The graphical results obtained after the application of the identification method are shown in figures 6.37 and 6.38.

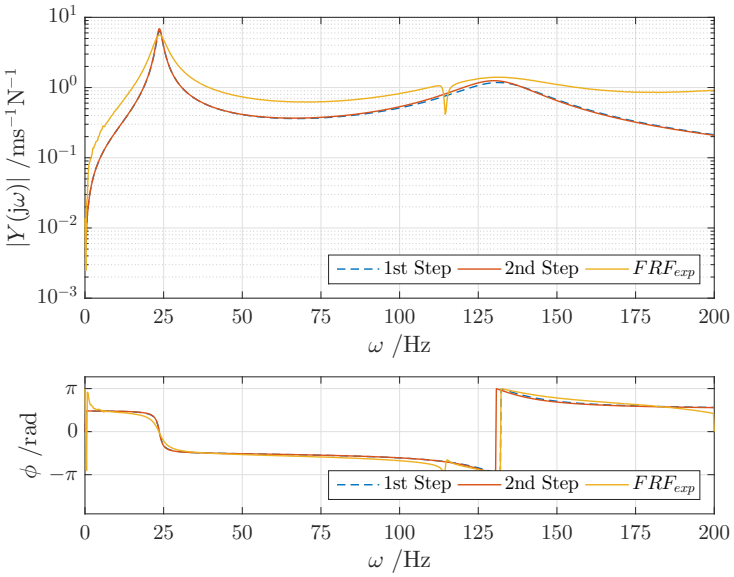

Figure 6.37: Experimental and identified $FRF_{260,108}$ using functions *fmincon* and *patternsearch* in the first and second steps, respectively.

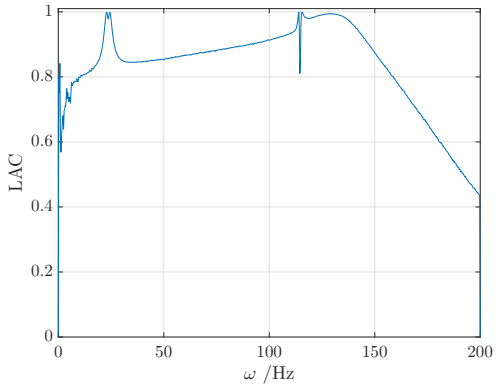

Figure 6.38: LAC for the $FRF_{260,108}$ using functions *fmincon* and *patternsearch* in the first and second steps, respectively.

The functions $FRF_{260,172}$ and $FRF_{260,260}$ lead to the identification of the parameters listed in table 6.24 and table 6.25, respectively. Both identified and experimentally obtained FRFs are

represented in figure 6.39 and in figure 6.41, and the LAC comparison are presented in figure 6.40 and figure 6.42.

Table 6.24: Identified parameters using the $FRF_{260,172}$ and functions *fmincon* and *patternsearch* in the first and second steps, respectively.

Parameter		First Step	Second Step
E_0	/Pa	1.0000×10^{6}	1.2893×10^{6}
E_∞	/Pa	1.0000×10^{9}	9.4759×10^{8}
τ	/s	1.0548×10^{-7}	1.0548×10^{-7}
α		5.4973×10^{-1}	5.3832×10^{-1}

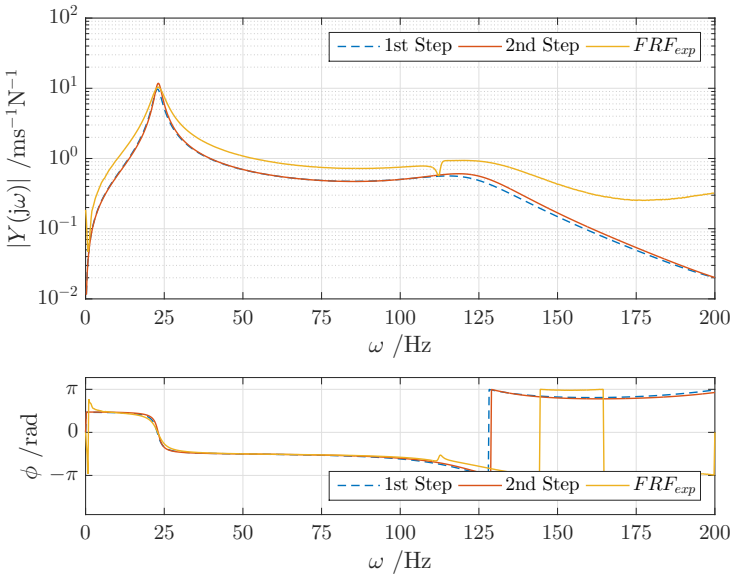

Figure 6.39: Experimental and identified $FRF_{260,172}$ using functions *fmincon* and *patternsearch* in the first and second steps, respectively.

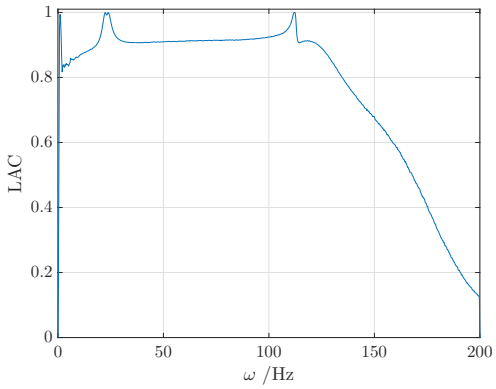

Figure 6.40: LAC for the $FRF_{260,172}$ using functions *fmincon* and *patternsearch* in the first and second steps, respectively.

Table 6.25: Identified parameters using the $FRF_{260,260}$ and functions *fmincon* and *patternsearch* in the first and second steps, respectively.

Parameter		First Step	Second Step
E_0	/Pa	1.0000×10^{6}	1.3760×10^{6}
E_∞	/Pa	1.0000×10^{9}	1.3677×10^{8}
τ	/s	4.5640×10^{-7}	4.5640×10^{-7}
α		6.1284×10^{-1}	4.9526×10^{-1}

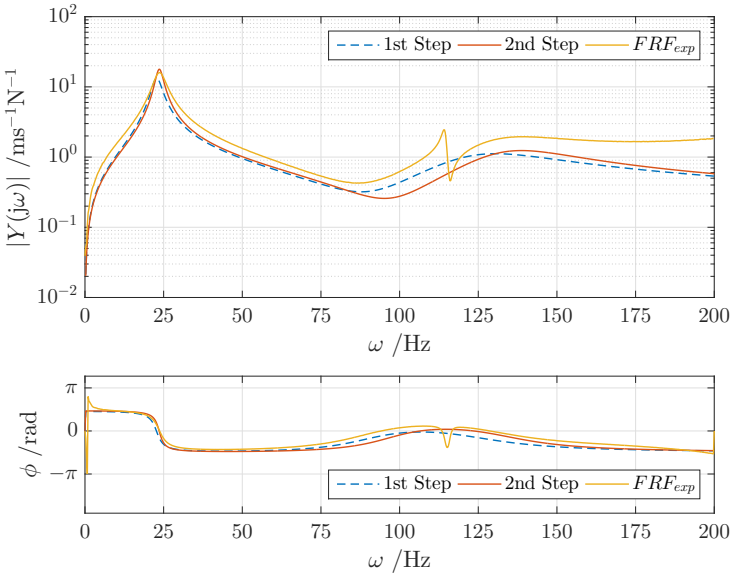

Figure 6.41: Experimental and identified $FRF_{260,260}$ using functions *fmincon* and *patternsearch* in the first and second steps, respectively.

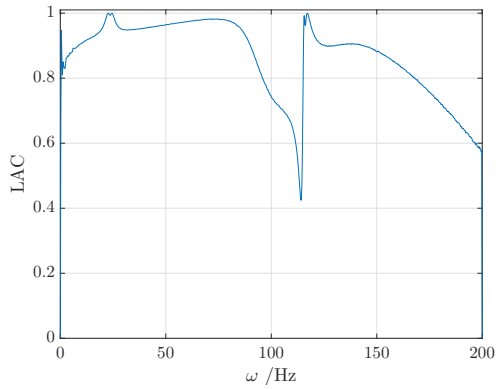

Figure 6.42: LAC for the $FRF_{260,260}$ using functions *fmincon* and *patternsearch* in the first and second steps, respectively.

1st Step: *patternsearch*, 2nd Step: *patternsearch*

Using the FRFs of composite beam C allied with direct search minimisation functions leads to the results present in the current chapter.

The application of $FRF_{260,108}$ results in the parameters shown in table 6.26.

Table 6.26: Identified parameters using the $FRF_{260,108}$ and evaluating both steps with *patternsearch*.

Parameter		First Step	Second Step
E_0	/Pa	1.7550×10^6	9.7752×10^5
E_∞	/Pa	3.2708×10^8	2.2341×10^8
τ	/s	1.0000×10^{-6}	1.0000×10^{-6}
α		5.0000×10^{-1}	4.5020×10^{-1}

Both experimental and numerical FRF are evidenced in figure 6.43. Validation using LAC is performed in figure 6.44.

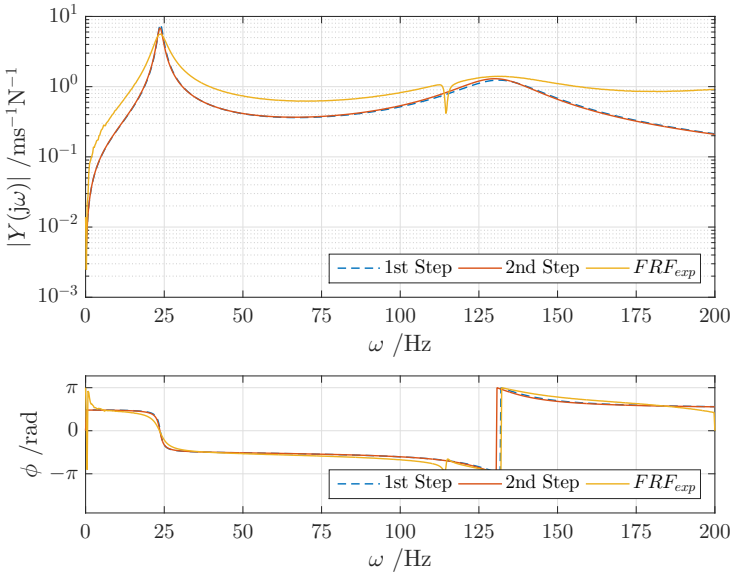

Figure 6.43: Experimental and identified $FRF_{260,108}$ using functions *patternsearch* for both steps.

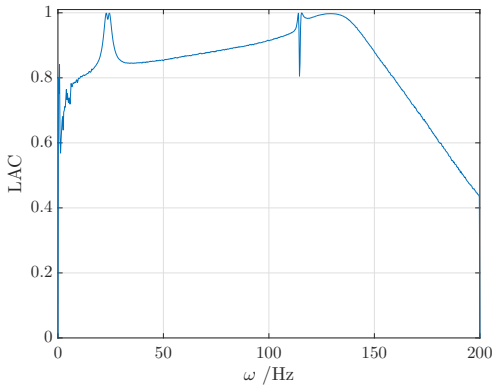

Figure 6.44: LAC for the $FRF_{260,108}$ using functions *patternsearch* for both steps.

The results using $FRF_{260,172}$ are listed in table 6.27.

Table 6.27: Identified parameters using the $FRF_{260,172}$ and evaluating both steps with *patternsearch*.

Parameter		First Step	Second Step
E_0	/Pa	1.3423×10^6	9.9127×10^5
E_∞	/Pa	1.7042×10^8	1.9946×10^8
τ	/s	1.0000×10^{-6}	1.0000×10^{-6}
α		5.0000×10^{-1}	4.8999×10^{-1}

The FRF obtained using the FEM and the one experimentally determined are shown in figure 6.45.

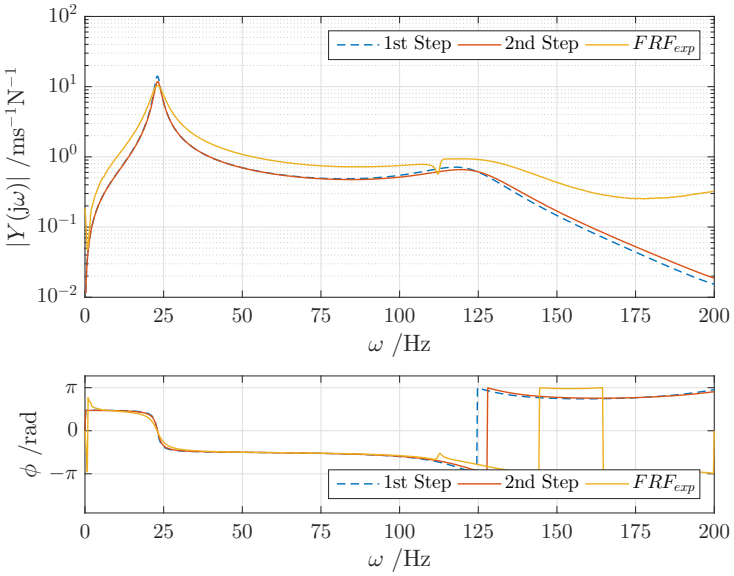

Figure 6.45: Experimental and identified $FRF_{260,172}$ using functions *patternsearch* for both steps.

The validation of the results is performed using LAC and shown in figure 6.46.

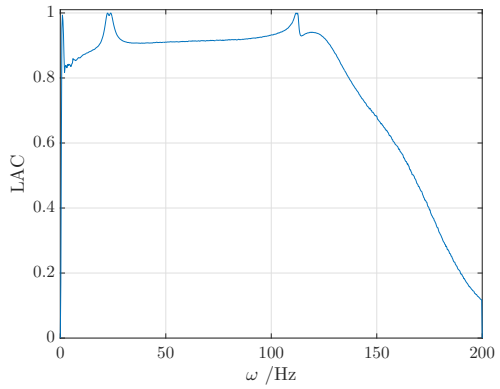

Figure 6.46: LAC for the $FRF_{260,172}$ using functions *patternsearch* for both steps.

Using the direct FRF leads to the parameters catalogued in table 6.28.

Table 6.28: Identified parameters using the $FRF_{260,260}$ and evaluating both steps with *patternsearch*.

Parameter		First Step	Second Step
E_0	/Pa	3.2443×10^6	3.6401×10^5
E_∞	/Pa	1.1929×10^8	4.2648×10^8
τ	/s	1.0000×10^{-6}	1.0000×10^{-6}
α		5.0000×10^{-1}	4.9905×10^{-1}

The representation of both experimental and numerical function is illustrated in figure 6.47.

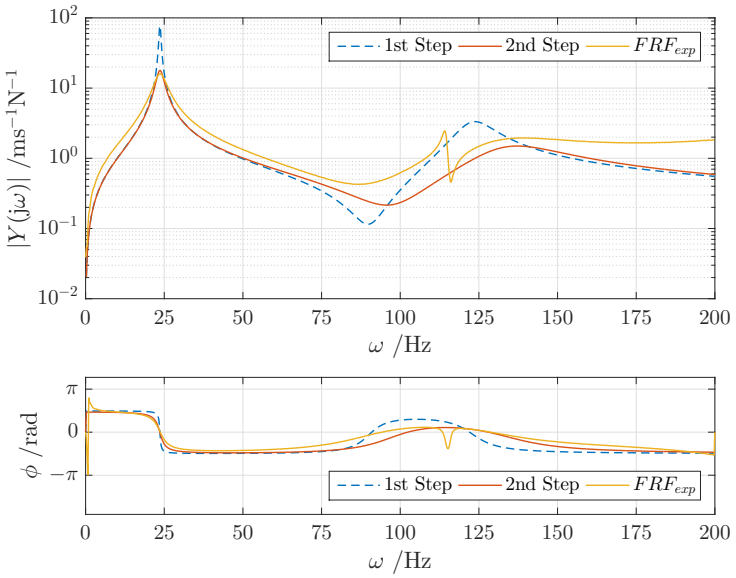

Figure 6.47: Experimental and identified $FRF_{260,260}$ using functions *patternsearch* for both steps.

The LAC validation is shown in figure 6.48.

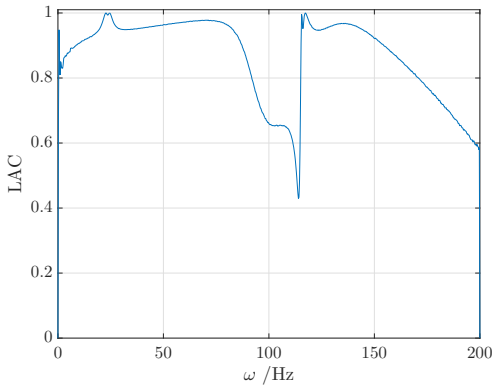

Figure 6.48: LAC for the $FRF_{260,260}$ using functions *patternsearch* for both steps.

6.3.4 Notes on the results obtained for the composite beams

1st Step: *fminsearch*, 2nd Step: *fmincon*

As previously stated, the results obtained using the minimisation function *fminsearch* in the first step and *fmincon* in the second step are not satisfactory as little correlation is reached in the resonance bandwidths.

Applying an unconstrained minimisation function can lead to results for the parameters physically inconsistent, as for example, negative values. Even though the results reached for the selected set of initial parameters do not evidence that occurrence, if the initial parameters were changed to the ones portrayed in table 6.29, the results attained would not be as satisfactory. As such, one can conclude that the implementation of a constrained algorithm generates more reliable data and simplifies the algorithm's search bandwidth.

Table 6.29: Evaluation of the first step of the minimisation process with different initial parameters using $FRF_{180,80}$ for composite beam A.

Parameter		Initial Parameter	First Step
E_0	/Pa	1.0000×10^5	7.5850×10^5
E_∞	/Pa	1.0000×10^6	2.4739×10^7
τ	/s	1.0000×10^{-6}	-9.7779×10^{-6}
α		5.0000×10^{-1}	2.1940×10^{-1}

1st Step: *fmincon*, 2nd Step: *patternsearch*

The implementation of the first step using *fmincon* and the second step using *patternsearch*, leads to satisfactory results in terms of the correlation between the numerical and experimental FRFs. Nonetheless, it is noticeable that towards the end of the measured frequency bandwidth the similarity of the two functions gradually decreases, which is an inevitable result as the evaluation of the second step is performed using a limited frequency bandwidth.

Regarding the numeric values obtained for the parameters, it is observable that they are quite similar, especially if considering the parameters obtained for each composite beam separately. When analysing the values attained in the first step, it is perceptible that only the parameters α and τ are optimised. That could be a result of the difference in magnitude of such values when compared to E_0 and E_∞. Such difference on the scaling of the parameters hinders the steps taken in each iteration of the minimisation process. As an attempt to overcome such occurrence, two measures were implemented: mathematically scaling the minimisation problem and conducting the first step in two stages, the first one optimising E_0 and E_∞ and the second stage where only τ and α are updated. However, the final results were not improved and the correlation between the generated and experimental functions deteriorated.

When comparing the experimental FRF resultant of the evaluation of the first step with the one obtained in the end of the identification process, it is visible that the general shape of the function is reached in the first step while the second step only leads to minor amplitude changes, mostly in the resonance bandwidth. The importance of the first step in order to approximate the solution and avoid local minimum values is, hence, demonstrated.

1st Step: *patternsearch*, 2nd Step: *patternsearch*

The application of a direct search method in both steps results in similar correlation values between the numeric and experimental FRFs as the ones reached using *fmincon* on the first step.

However, the computational time of *patternsearch* is far superior, resulting in, as reference, 52 minutes as opposed to 32 minutes when evaluating *fmincon* in the first step for the $FRF_{180,108}$ of composite beam A.

It is verified that for all the composite beams tested and for the both steps of the minimisation method, the parameter τ remains unaffected. Although, in subsequent chapters, when the analysis of the influence of initial parameters on the results is established, its value is optimised for a single combination of initial parameters, which indicates that $\tau = 1 \times 10^{-6}$ s does not update as it is too close of the optimum solution.

It is also verified using *patternsearch* in both steps of the identification method, that the frequency alignment conducts to results very close to the optimal ones.

6.3.5 Identified Storage Modulus and Loss Factor

After the identification of the fractional derivative model parameters, the frequency dependent properties of the viscoelastic material can then be determined as a function of frequency. The results achieved using the two combinations of minimisation functions proposed are present in the current chapter.

For each composite beam, the storage modulus and loss factor are indicated within the frequency band of the experimental frequency response function. As such, care must be taken when comparing different composite beams.

1st Step: *fmincon*, 2nd Step: *patternsearch*

The resulting properties, $E'(\omega)$ and $\eta(\omega)$, obtained when evaluating the first step using *fmincon* and the second step with *patternsearch* are presented in figures 6.49, 6.50 and 6.51 for composite beams A, B and C, respectively.

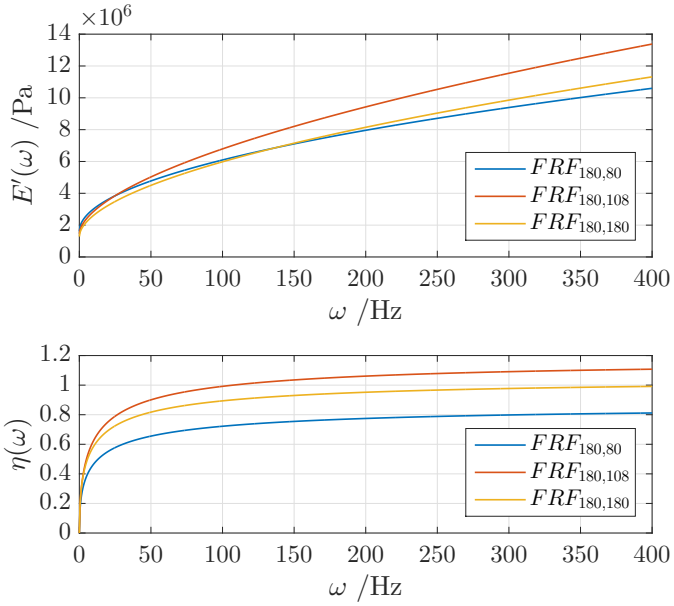

Figure 6.49: Storage modulus and loss factor obtained for the composite beam A using the parameters obtained from the evaluation of the 1st Step using *fmincon* and the 2nd Step using *patternsearch*.

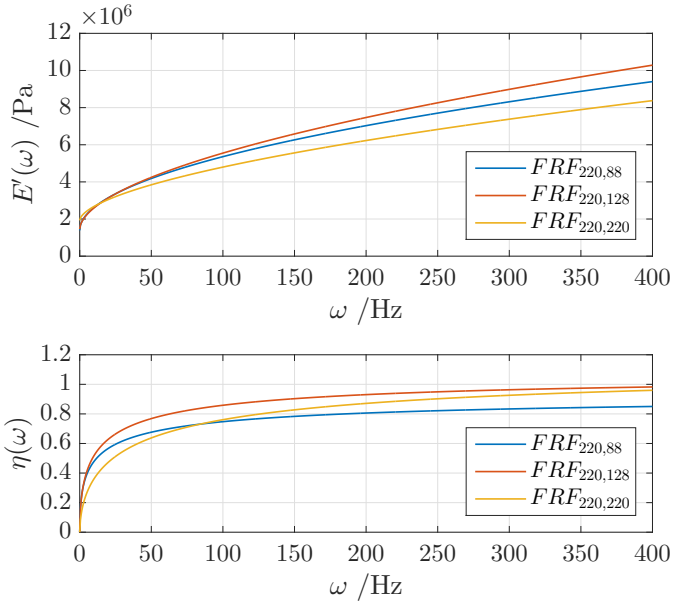

Figure 6.50: Storage modulus and loss factor obtained for the composite beam B using the parameters obtained from the evaluation of the 1st Step using *fmincon* and the 2nd Step using *patternsearch*.

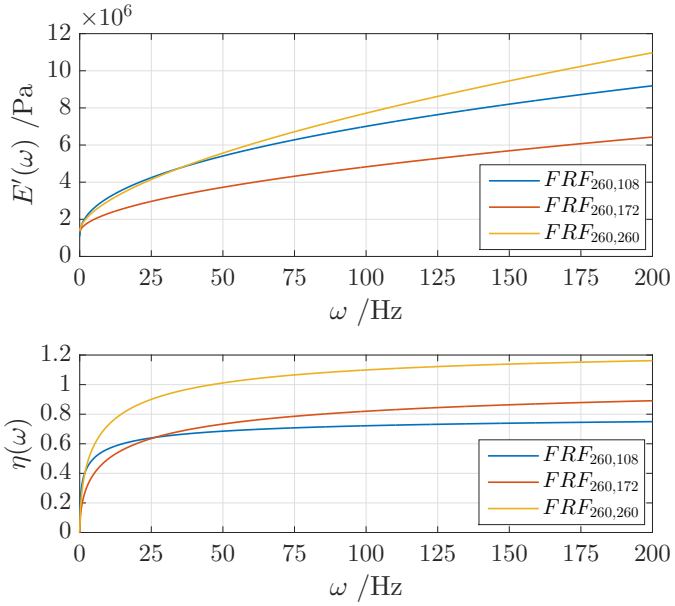

Figure 6.51: Storage modulus and loss factor obtained for the composite beam C using the parameters obtained from the evaluation of the 1st Step using *fmincon* and the 2nd Step using *patternsearch*.

1st Step: *patternsearch*, 2nd Step: *patternsearch*

The frequency dependent properties obtained for each composite beam when using *patternsearch* in both steps of the minimisation process are illustrated in figures 6.52, 6.53 and 6.54.

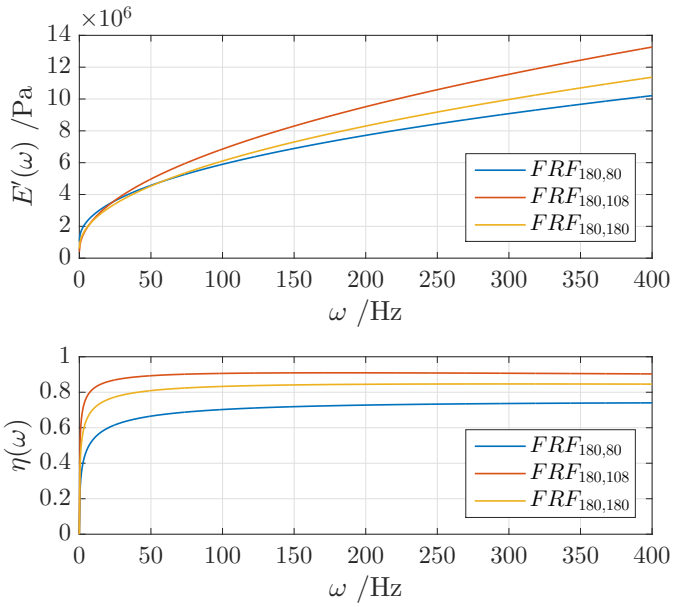

Figure 6.52: Storage modulus and loss factor obtained for the composite beam A using the parameters obtained from the evaluation of both steps using *patternsearch*.

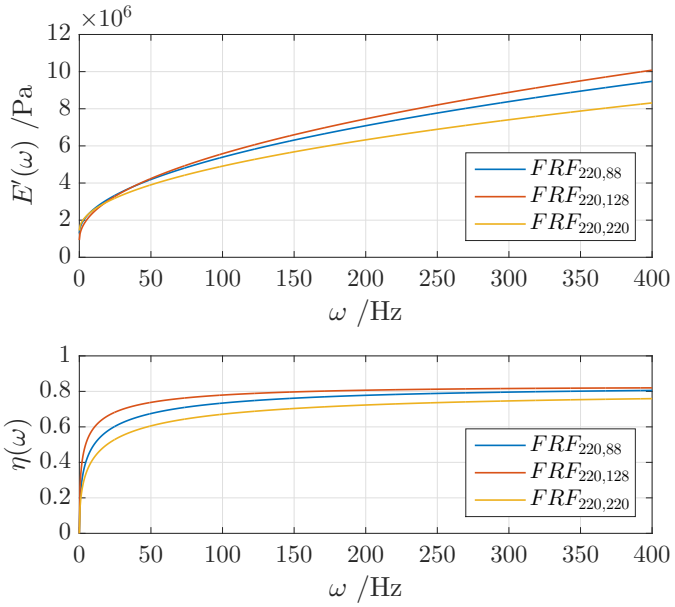

Figure 6.53: Storage modulus and loss factor obtained for the composite beam B using the parameters obtained from the evaluation of both steps using *patternsearch*.

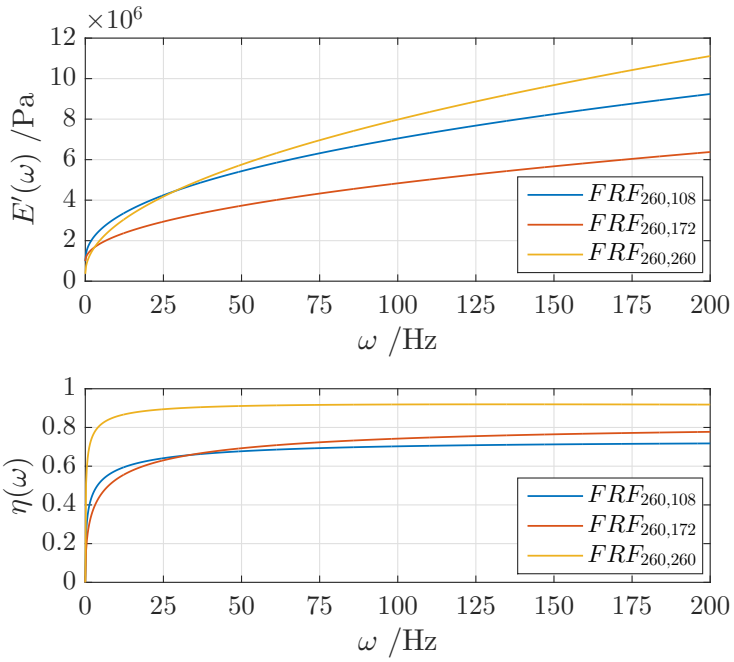

Figure 6.54: Storage modulus and loss factor obtained for the composite beam C using the parameters obtained from the evaluation of both steps with *patternsearch*.

The attained results for the frequency dependent properties of 3M ISD112 are not coincident. It is verified that the least coherence is shown, with no exception, for composite beam C. Although the numeric values vary, the tendency of $E'(\omega)$ and $\eta(\omega)$ remains the same for all composite beams and all the excitation points, showing an increase of both values as the frequency increases.

The identification of the final properties of the viscoelastic material is performed considering the FRF where the most impressive correlation level is verified. The results adopted are the ones obtained from the application of the two-step identification method with $FRF_{180,108}$ of composite beam A using *fmincon* in the first step and *patternsearch* in the second step. For reference, the values of the identified parameters of the fractional derivative model are shown in table 6.30 and a representation of the storage modulus and loss factor is illustrated in figure 6.55.

Table 6.30: Identified fractional derivative model parameters for the material 3M ISD112 using the two-step identification method.

Parameter		Value
E_0	/Pa	1.4540×10^{6}
E_∞	/Pa	1.0474×10^{9}
τ	/s	3.9301×10^{-7}
α		5.7791×10^{-1}

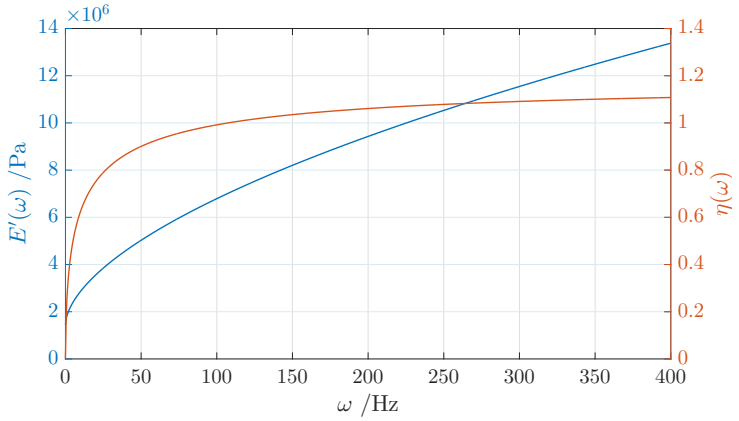

Figure 6.55: Identified storage modulus and loss factor using the two-step identification method.

6.3.6 Influence of the initial parameters

It is verified an extreme dependence of the results obtained for the fractional derivative parameters on the initial parameters. As such, different initial conditions are tested and the results are documented in the current chapter.

The results are listed in table 6.31 and in table 6.32. The first one corresponds to the evaluation of the first step using *fmincon* and the second step using *patternsearch*, and the latter corresponds to the evaluation of both steps using *patternsearch*. The FRF used for the identification method is $FRF_{180,108}$ of composite beam A.

Table 6.31: Initial parameter influence on the results obtained for $FRF_{180,108}$ using *fmincon* in the first step and the second step evaluated with *patternsearch*.

Parameter		Initial Parameters	First Step	Second Step
E_0	/Pa	1.0000×10^{5}	1.0000×10^{5}	1.4392×10^{6}
E_∞	/Pa	1.0000×10^{9}	1.0000×10^{9}	1.0063×10^{9}
τ	/s	1.0000×10^{-6}	4.1458×10^{-7}	4.1458×10^{-7}
α		5.0000×10^{-1}	5.8795×10^{-1}	5.7513×10^{-1}
E_0	/Pa	1.0000×10^{6}	1.0000×10^{6}	3.6623×10^{-4}
E_∞	/Pa	1.0000×10^{8}	1.0000×10^{8}	1.3695×10^{8}
τ	/s	1.0000×10^{-6}	4.0529×10^{-6}	4.0529×10^{-6}
α		5.0000×10^{-1}	4.5874×10^{-1}	4.6405×10^{-1}
E_0	/Pa	1.0000×10^{6}	1.0000×10^{5}	9.4873×10^{5}
E_∞	/Pa	1.0000×10^{9}	1.0000×10^{9}	1.2804×10^{9}
τ	/s	1.0000×10^{-7}	1.4302×10^{-7}	1.4302×10^{-7}
α		5.0000×10^{-1}	5.3901×10^{-1}	5.3420×10^{-7}
E_0	/Pa	1.0000×10^{6}	1.0000×10^{6}	2.3453×10^{5}
E_∞	/Pa	1.0000×10^{9}	1.0000×10^{9}	3.6294×10^{8}
τ	/s	1.0000×10^{-6}	5.8985×10^{-6}	5.8985×10^{-6}
α		8.0000×10^{-1}	8.0983×10^{-1}	6.6920×10^{-1}
E_0	/Pa	1.0000×10^{5}	1.7646×10^{5}	1.5596×10^{-2}
E_∞	/Pa	1.0000×10^{7}	1.0002×10^{7}	6.1994×10^{6}
τ	/s	1.0000×10^{-5}	4.3342×10^{-6}	8.9045×10^{2}
α		5.0000×10^{-1}	6.1162×10^{-2}	9.4365×10^{-2}

As is perceptible from the analysis of the table listed above, the results obtained for the parameters differ quite substantially when distinct initial parameters are used. The change of one order of magnitude of the parameters E_0, τ leads to coherent results from those obtained in previous subchapters and so does the change of the parameter α. However, when the changes occur in the parameter E_∞, the solution diverges quite considerably which can be a result of the higher order of magnitude of such parameter.

The method proves to be unstable when the entire initial parameters differ considerably from the ones tested in preceding chapters, resulting in incoherent values for the parameters and small correlation levels of the two FRFs.

Table 6.32: Initial parameter influence on the results obtained for $FRF_{180,108}$ evaluated with *patternsearch* in both steps.

Parameter		Initial Parameters	First Step	Second Step
E_0	/Pa	1.0000×10^5	3.9528×10^6	4.1210×10^5
E_∞	/Pa	1.0000×10^9	1.5213×10^8	3.6247×10^8
τ	/s	1.0000×10^{-6}	1.0000×10^{-6}	1.0000×10^{-6}
α		5.0000×10^{-1}	5.0000×10^{-1}	4.9948×10^{-1}
E_0	/Pa	1.0000×10^6	4.0411×10^6	4.1215×10^5
E_∞	/Pa	1.0000×10^8	1.4901×10^8	3.6247×10^8
τ	/s	1.0000×10^{-6}	1.0000×10^{-6}	1.0000×10^{-6}
α		5.0000×10^{-1}	5.0000×10^{-1}	4.9948×10^{-1}
E_0	/Pa	1.0000×10^6	3.7951×10^6	4.8417×10^5
E_∞	/Pa	1.0000×10^9	4.8982×10^8	1.1295×10^9
τ	/s	1.0000×10^{-7}	1.0000×10^{-7}	1.0000×10^{-7}
α		5.0000×10^{-1}	5.0000×10^{-1}	4.9948×10^{-1}
E_0	/Pa	1.0000×10^6	5.0487×10^6	2.6070×10^6
E_∞	/Pa	1.0000×10^9	1.7122×10^9	1.3717×10^9
τ	/s	1.0000×10^{-6}	1.0000×10^{-6}	1.0000×10^{-6}
α		8.0000×10^{-1}	8.0000×10^{-1}	6.9063×10^{-1}
E_0	/Pa	1.0000×10^5	8.9948×10^5	2.9777×10^6
E_∞	/Pa	1.0000×10^6	8.3676×10^6	2.2143×10^7
τ	/s	1.0000×10^{-5}	5.6271×10^{-3}	5.6122×10^{-4}
α		5.0000×10^{-1}	9.0884×10^{-1}	9.0935×10^{-1}

The results show, as expected, an improvement relative to the ones obtained when using the function *fmincon* in the first step of the minimisation process. However, the results are still not numerically coincident.

Changing the parameters E_0 and E_∞ of one order of magnitude leads to the same results in the end of the second step. As such, the method proves to be quite robust to changes on those parameters. As for τ and α, it was previously noted that the algorithm only leads to minor or even null changes in such parameters. That result is preserved when a different set of initial parameters are used. Merely when changing the values of the entire set of parameters both τ and α are updated.

6.3.7 Influence of the number of modes considered

As previously settled, the last mode of vibration used for the determination of the numerical FRF presents a smaller correlation than the first one considered. As such, evaluating the evolution of the parameters considering a different number of modes of vibration is relevant. As such, for the composite beams B and C, the values of the parameters are determined considering 1, 2 and 3 vibration modes. This procedure is implemented using for the first step *fmincon* and the second step *patternsearch* since it conducts to results that exhibit satisfactory correlation values with a smaller computational time.

Composite Beam B

For the evaluation of the performance of the identification method using different numbers of modes of vibration of the composite beam B, the following integration bandwidths are used:

Table 6.33: Integration bandwidths used in the 2nd step of the identification method for the composite beam B.

Number of Modes of Vibration	Integration Bandwidth [Hz]
1	[0 100]
2	[0 250]
3	[0 550]

The results obtained using $FRF_{220,128}$ of the fractional derivative model parameters are summarised in table 6.34.

Table 6.34: Fractional derivative model parameters considering 1, 2 and 3 modes of vibration for $FRF_{220,128}$.

Parameter		1 Mode	2 Modes	3 Modes
E_0	/Pa	1.6211×10^6	1.4549×10^6	1.1477×10^6
E_∞	/Pa	7.6004×10^8	6.5834×10^8	3.5455×10^8
τ	/s	4.6569×10^{-7}	3.9301×10^{-7}	6.1182×10^{-7}
α		5.8385×10^{-1}	5.7791×10^{-1}	5.1385×10^{-1}

In figure 6.56 are shown the generated FRFs as opposed to the one obtained experimentally.

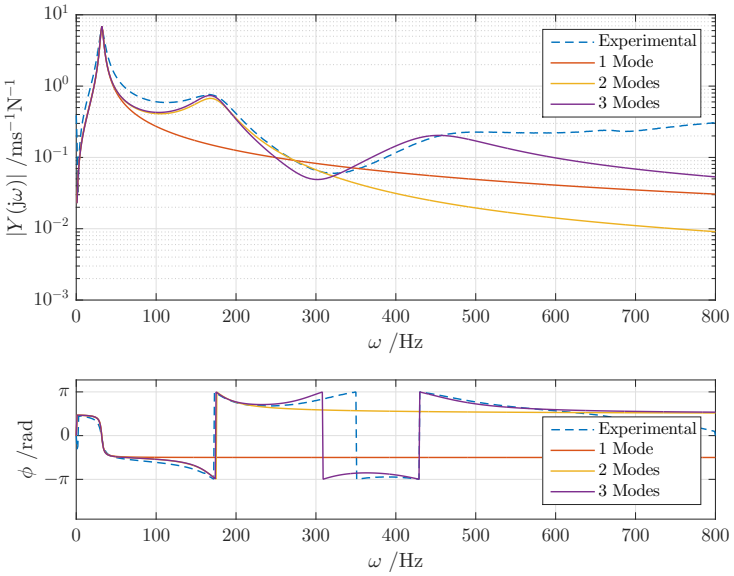

Figure 6.56: Experimental and identified $FRF_{220,128}$ using 1, 2 and 3 modes of vibration.

Composite Beam C

For the composite beam C, the integration bandwidths used are listed in table 6.35.

Table 6.35: Integration bandwidths used in the 2nd step of the identification method for the composite beam C.

Number of Modes of Vibration	Integration Bandwidth [Hz]
1	[0 50]
2	[0 150]
3	[0 400]

Table 6.36: Fractional derivative model parameters considering 1, 2 and 3 modes of vibration for $FRF_{260,172}$.

Parameter		1 Mode	2 Modes	3 Modes
E_0	/Pa	1.4542×10^6	1.2893×10^6	1.0936×10^6
E_∞	/Pa	7.6910×10^8	9.4758×10^9	4.8689×10^8
τ	/s	2.9082×10^{-7}	1.0548×10^{-7}	4.5281×10^{-7}
α		5.7924×10^{-1}	5.3832×10^{-1}	5.3970×10^{-1}

In the following figure, the FRF generated using different number of modes considered is illustrated in comparison to the one obtained experimentally.

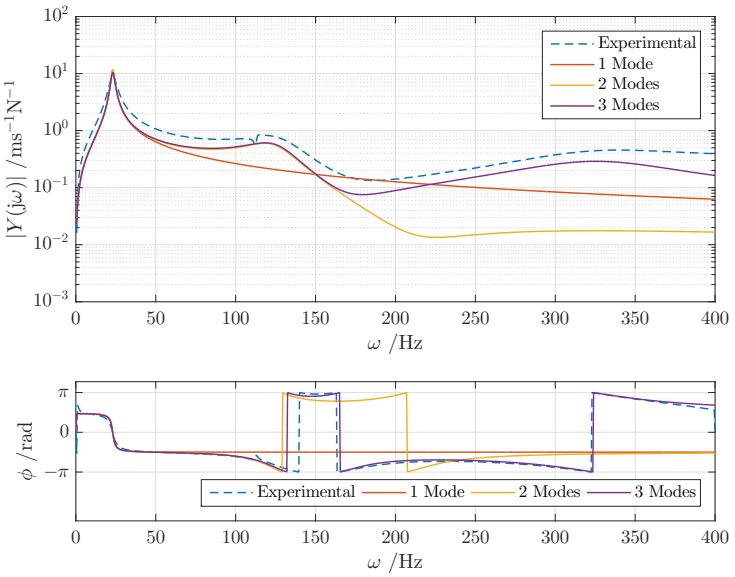

Figure 6.57: Experimental and identified $FRF_{260,172}$ using 1, 2 and 3 modes of vibration.

In contrast to what is expected, increasing the number of modes considered to calculate the numerical FRF does not lead to better correlation results on the previous modes of vibration. In fact, it is verified that increasing the number of modes considered, which extends the dimension of the eigenproblem and therefore leads to a higher number of function evaluations in both first and second steps, results in added computational time with just a slight change in the resulting parameters.

However, it is noteworthy that the experimental functions that evidence a frequency bandwidth that includes 3 modes of vibration are determined with a smaller frequency resolution than those of smaller frequency bandwidths. The resolution of the experimental FRFs is imposed by the FFT analyser and interferes with the accuracy of the minimisation process.

In conclusion, it is presumed that the application of the current identification method is as efficient when only a single mode of vibration is used. In other words, the increase of the dimension of the problem and the decrease of resolution in frequency when a higher number of modes is considered hinders the minimisation process.

6.4 Conclusions

The identification method implemented and evaluated in the current chapter is quite a numerically complex method, as it requires the iterative identification of the natural frequencies of the damped system, which entails the solution of multiple eigenvalue problems. Hence, it shows a high computational cost and several function evaluations.

It is noticeable that, in spite of the function to be minimised being only relative to the magnitude of the FRF generated, the phase of the function generated is almost coincident with the one determined experimentally. This fact reinforces that the dynamic information of a system is mainly present in the magnitude of the FRF.

Regarding the application of such method on the samples tested experimentally, it is perceptible the high level of coherence attained for lightly damped systems, as the base aluminium beams, conducting to precise results and almost total superposition of the frequency response functions. It could be a result of a smaller number of updating parameters (2 instead of 4) or the smaller loss factor, and evidently, damping ability of the aluminium.

As for the application of the identification method on the composite beams, the results reached do not acquire the level of correlation of the base beams. Nonetheless, minimum values of 0.8 using Local Amplitude Criterion are obtained, which validates the application of the method on sandwich-type samples. It is also noteworthy that the least precise results are obtained for composite beam C, which could also be related to defects on the experimental sample, leading to worst experimental results, as it shows the most prominent disturbance around the second mode of vibration.

The implementation of the second step using an integral minimisation function leads to a great robustness in the presence of experimental noise or even the distortion exhibited around the second mode of vibration.

As to more specific conclusions, it is noticeable a good agreement in the results combined with small computational times when using a single mode of vibration to numerically generate the FRF. Furthermore, it is established that the initial parameters should be carefully chosen and if possible different combinations should be tested to guarantee the accuracy of the results.

Chapter 7

Direct Frequency Response Identification Method

7.1 Introduction

In the current chapter, an alternative inverse method of determining the four parameters of the fractional derivative model of the viscoelastic material is developed and implemented.

This method, based on the one proposed by Martinez-Agirre and Elejabarrieta (2011), minimises the difference between frequency response functions determined experimentally and the ones calculated numerically using a direct frequency analysis. The minimisation process is evaluated at certain discrete frequencies, termed control frequencies, located in the resonance bandwidth and selected by the user.

7.2 Finite Element Model

The finite element model of the composite beam is based on a *Layerwise* beam theory, being each layer analysed using a *Timoshenko* formulation. The beam is discretised using linear elements with two nodes.

As referred in previous chapters, the differential equations of motion can be expressed in matrix form in the following manner:

$$[M]\{\ddot{x}\} + [K^*(\omega)]\{x\} = \{F\}, \tag{7.1}$$

where $[M]$ is the mass matrix, $[K^*]$ the complex stiffness matrix and $\{x\}$ and $\{F\}$ are the displacement and force vectors, respectively. The stiffness matrix is generated with a unitary and factorised complex modulus, meaning that in the finite element model, a frequency independent stiffness matrix is calculated. The frequency dependence is introduced by multiplying the complex modulus obtained from the fractional derivative model by the viscoelastic component of the stiffness matrix.

Considering that the beam is subjected to a steady-state harmonic excitation, writing equation (7.1) in the frequency domain results as follows:

$$\left[-\omega^2[M] + [K^*(\omega)]\right]\{\bar{X}(\mathrm{j}\omega)\} = \{F\}. \tag{7.2}$$

7.3 Numerical Frequency Response Function

In the current method the frequency response function is obtained at each control frequency, updating the stiffness matrix.

The receptance resultant from the application of a unitary load in the degree of freedom j, $\{\alpha_j(\mathrm{j}\omega)\}$, can be calculated solving the system of equations (7.2).

The experimentally determined FRF are mobilities, as such, in order to numerically obtain such function it is necessary to derivate $\alpha_j(\omega)$ in the frequency domain:

$$\{Y_j(\mathrm{j}\omega)\} = \mathrm{j}\omega\{\alpha_j(\mathrm{j}\omega)\}. \tag{7.3}$$

The numerical FRF corresponds to the mobility on the free end of the beam, l, resultant of the application of an excitation in the degree of freedom j as evidenced in equation (7.4).

$$FRF_{num} = Y_{lj}(\mathrm{j}\omega). \tag{7.4}$$

7.3.1 Control Frequencies

The selection of the control frequencies where the numerically determined FRF and the experimentally obtained FRF will be minimised, must satisfy a few requirements advised in (Martinez-Agirre and Elejabarrieta, 2011). The control frequencies must be located in the resonance bandwidths, since they define the dynamic response of the system and a good signal-to-noise ratio is assured. In the mentioned article, the algorithm is developed using displacement transmissibility functions and it is advised to use control frequencies located in the bandwidth defined by the local minimum and maximum of the real part of such function. Since the functions used in the current work are mobilities, whose real part contains only a local maximum at the resonant frequency, it will be assured that the control frequencies are situated in a range defined by the local maximum and minimum of the imaginary part of the FRF.

Some caution must be taken in order to avoid compromised frequency bands where the experimental noise is significant. The number of discrete frequencies used to minimise the functions is optional. Martinez-Agirre and Elejabarrieta (2011) recommend a minimum of three points at each resonance and indicate that a higher number of frequencies leads to better results.

7.4 Identification Method

The identification method consists of solving the system of equations expressed in (7.2) for a set of fractional derivative model parameters, updating the stiffness matrix at each control frequency. The model's parameters are then iterated to minimise the difference of the FRF obtained numerically and experimentally. The minimisation function, determined both in real and imaginary parts is as follows:

$$f_{min} = \sum_{c=1}^{n} \left| \frac{FRF_{num}(\omega_c) - FRF_{exp}(\omega_c)}{FRF_{exp}(\omega_c)} \right|, \tag{7.5}$$

where the subscript *num* and *exp* denote, respectively, the numerical and experimental frequency response functions and ω_c indicates the control frequencies selected. A diagram of the method is illustrated in figure 7.1.

The algorithm is implemented in the software `Matlab`® using a minimisation function available on the `Optimization Toolbox`®. The function used is based on the Nelder-Mead simplex algorithm and is called *fminsearch*. As this algorithm is an unconstrained one, in order to validate the solution obtained, the thermodynamic constraints must be verified which results in: all the parameters must take a positive non-null value, $E_\infty > E_0$ and $\alpha < 1$ (Bagley and Torvik, 1986).

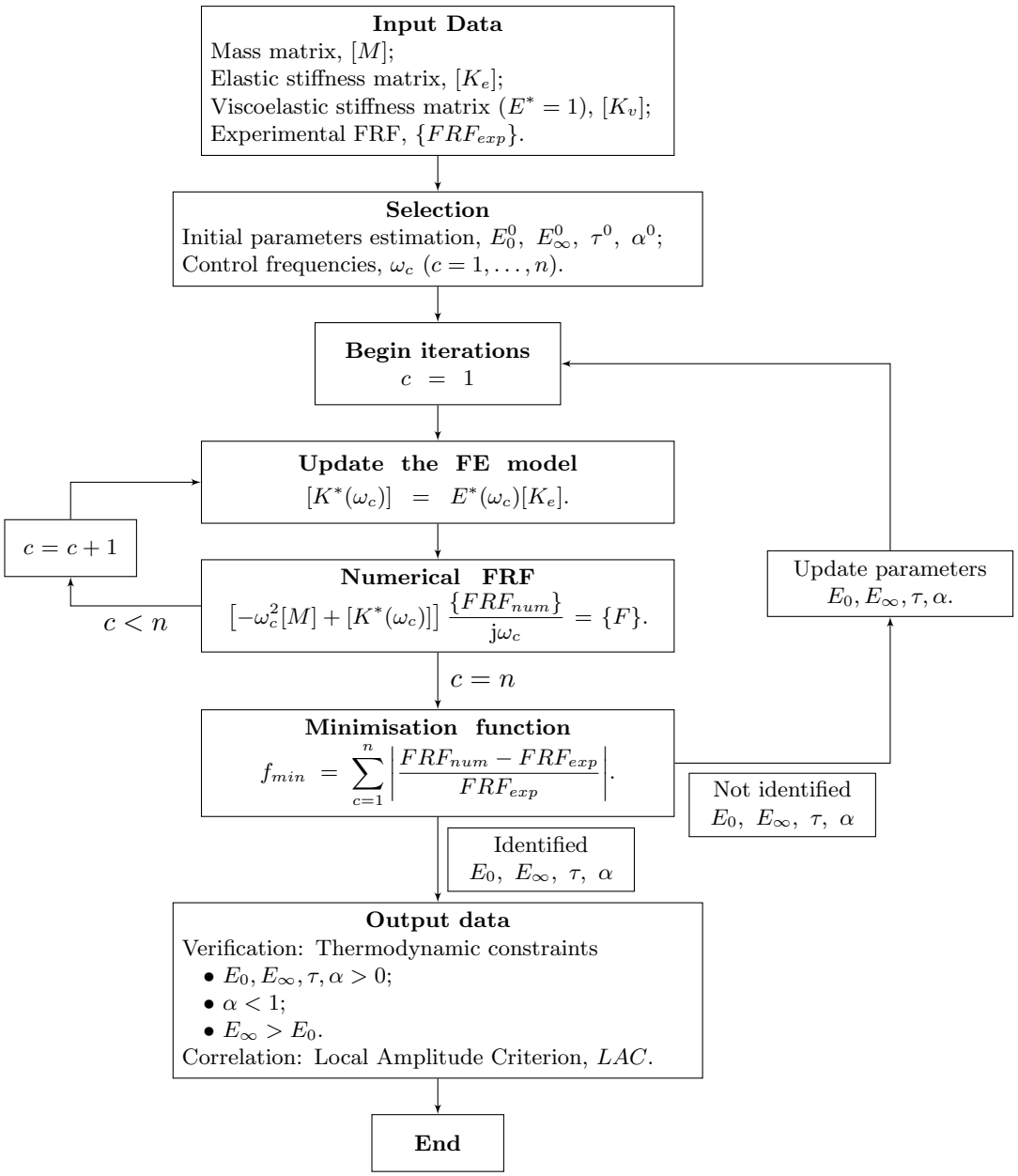

Figure 7.1: Diagram of the Direct-Frequency Response Identification Method.

Chapter 8

Direct Frequency Response Method Application

8.1 Introduction

In the ongoing chapter, the direct frequency response method is applied using the experimentally determined FRFs in order to obtain the mechanical properties of the bare aluminium beam and the fractional derivative model parameters of the viscoelastic material 3M ISD112. The dynamic properties of such material are then attained from the fractional derivative model parameters and their evolution within the experimental frequency bandwidth is determined.

It is also intended to evaluate the performance of the current algorithm when a different number of modes of vibration is considered and when different control frequencies are used.

Likewise to the algorithm implemented in the previous identification method, several minimisation functions are tested. However, the only function that returns satisfactory results is *fminsearch*.

8.2 Base Beam results

The application of the current method for the determination of the base beam properties, E and η, is evaluated using a single mode of vibration and 5 control frequencies located in the frequency bandwidth defined by [23.75 24.75] Hz, with a sampling frequency of $\Delta f = 0.25$.

The initial parameters supplied for initialising the method are listed in table 8.1.

Table 8.1: Initial parameters for the identification method for the bare beam.

Parameter	Value
E /Pa	69×10^9
η	1×10^{-3}

8.2.1 $FRF_{180,44}$

Testing $FRF_{180,44}$ in the identification process, leads to the determination of the parameters summarised in table 8.2.

Table 8.2: Identified parameters using $FRF_{180,44}$

Parameter	Value
E /Pa	60.2907×10^{9}
η	6.0000×10^{-3}

The representation of both the numerically generated and experimentally determined functions is present in figure 8.1.

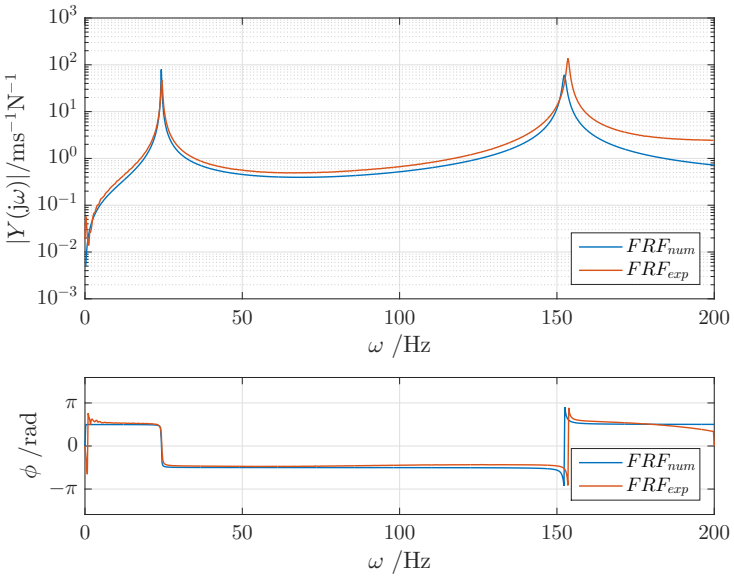

Figure 8.1: Experimental and identified $FRF_{180,44}$.

The quantitative comparison of the two FRF is performed using LAC. The resulting graph is present in figure 8.2.

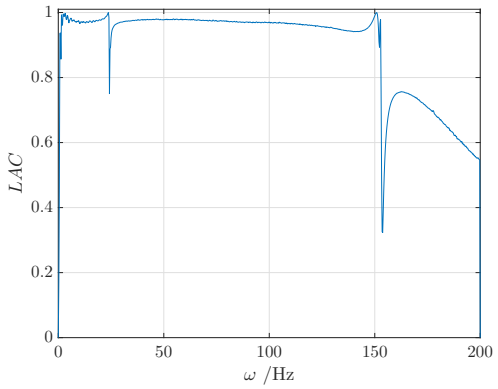

Figure 8.2: LAC for the $FRF_{180,44}$.

8.2.2 $FRF_{180,108}$

Using the $FRF_{180,108}$ leads to the results listed in table 8.3.

Table 8.3: Identified parameters using $FRF_{180,108}$

Parameter	Value
E /Pa	60.3354×10^9
η	5.5000×10^{-3}

The experimental and the generated FRF are shown in figure 8.3.

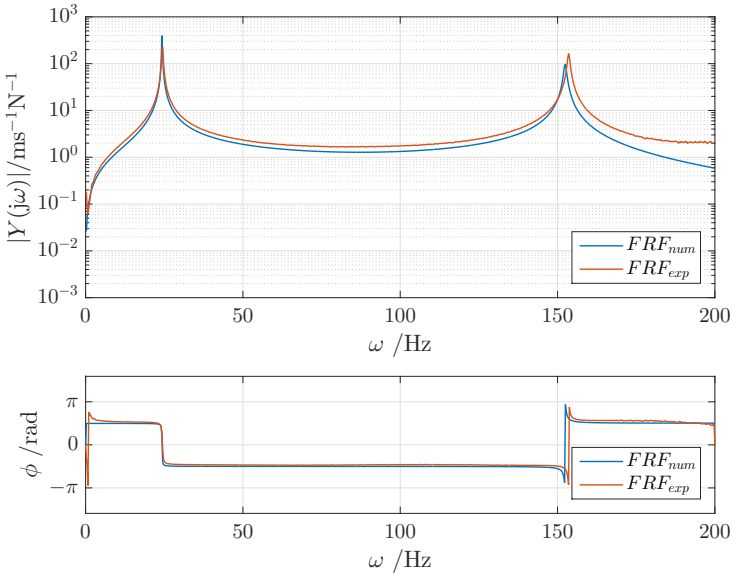

Figure 8.3: Experimental and identified $FRF_{180,108}$.

In figure 8.6 is depicted the result of the comparison of such functions using the LAC.

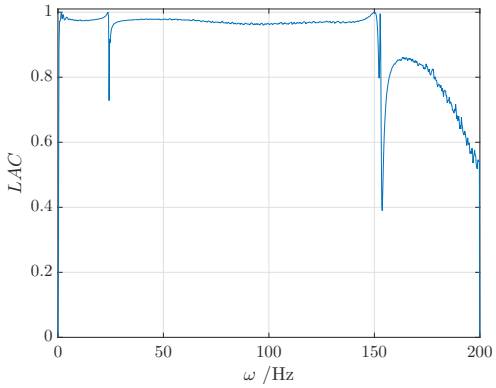

Figure 8.4: LAC for the $FRF_{180,108}$.

8.2.3 $FRF_{180,180}$

When the identification method is evaluated with the direct FRF, the results reached are the ones summarised in table 8.4.

Table 8.4: Identified parameters using $FRF_{180,180}$

Parameter	Value
E /Pa	61.9204×10^{9}
η	8.3000×10^{-3}

The FRF are then represented in figure 8.5 and compared using the LAC in figure 8.6.

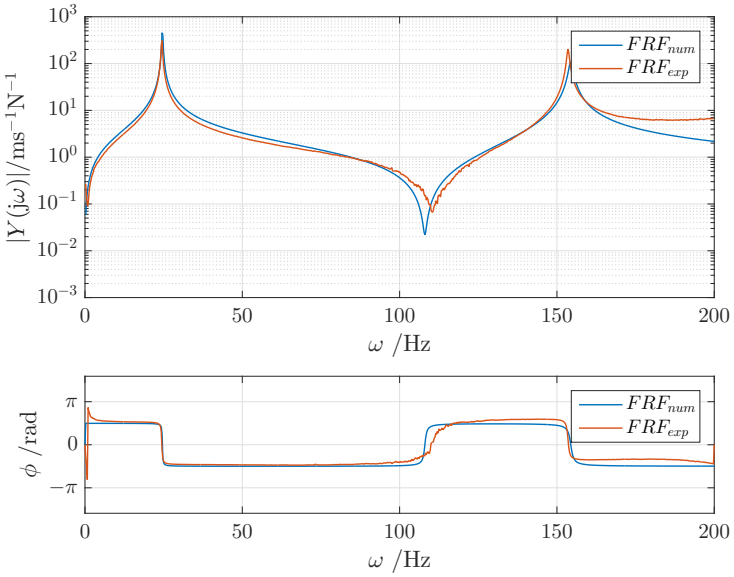

Figure 8.5: Experimental and identified $FRF_{180,180}$.

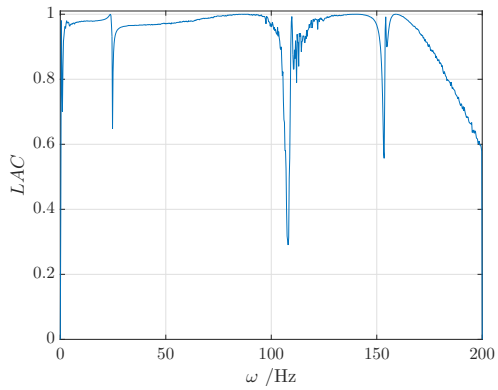

Figure 8.6: LAC for the $FRF_{180,180}$.

8.2.4 Notes on the bare beam results

The minimisation process using FRFs of the bare beam shows an extreme dependence on the number of control frequencies selected.

The selection of a single mode of vibration proves to be sufficient to accurately determine the base beam parameters. Nonetheless, LAC indicates a lower correlation in the second natural frequency bandwidth. As for the direct FRF, it is additionally detectable a lower correlation in the vicinity of the antiresonance.

The identified modulus of elasticity, E, and loss factor, η, are obtained as the average of the values determined with each frequency response function and are listed in table 8.5.

Table 8.5: Determined properties of the aluminium bare beam.

Parameter		Value
E	/Pa	61.0000×10^{9}
η		6.6000×10^{-3}

8.3 Composite Beam results

In the current chapter, the application of the direct frequency response method is evaluated considering a single mode of vibration. The minimisation function is calculated in 15 control frequencies located in the resonance bandwidth and between the local maximum and minimum of the imaginary component of the FRFs.

For each composite beam, three FRF are used to identify the fractional derivative model parameters which corresponds to the application of the impact in different degrees of freedom and the measurement of the response in the free end of the beam.

The initial parameters supplied to start the minimisation process, just as the ones used in the previous identification method, are listed in table 8.6.

Table 8.6: Initial parameters for the composite beams.

Parameter		Identified Parameter
E_0	/Pa	1×10^{6}
E_∞	/Pa	1×10^{9}
τ	/s	1×10^{-6}
α		1×10^{-9}

8.3.1 Composite Beam A

For the composite beam A the frequency bandwidth of the first mode of vibration evaluated is located between [43.5 50.5] Hz, with a $\Delta f = 0.5$.

The application of the current method on the $FRF_{180,80}$ leads to the results for the parameters presented in table 8.7:

Table 8.7: Evaluation of the direct frequency response identification method using $FRF_{180,80}$.

Parameter		Identified Parameter
E_0	/Pa	9.2517×10^{5}
E_∞	/Pa	8.3209×10^{8}
τ	/s	1.0157×10^{-6}
α		6.7042×10^{-1}

The representation of the synthesised FRF and the one obtained experimentally is evidenced in figure 8.7.

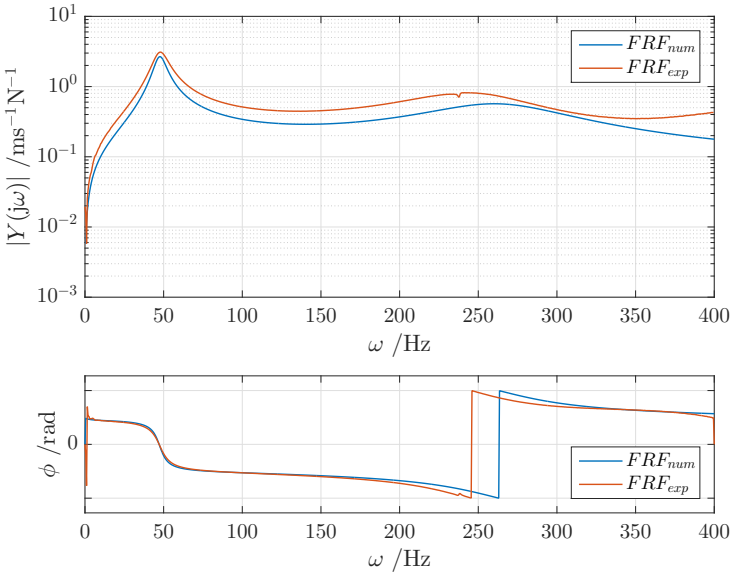

Figure 8.7: Experimental and identified $FRF_{180,80}$.

The quantitative comparison of the two functions is performed using LAC and the result of its application is presented in figure 8.8.

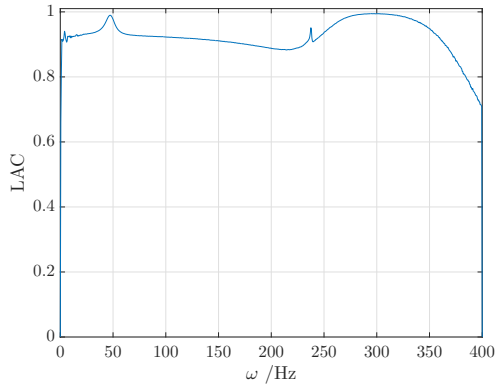

Figure 8.8: LAC for the $FRF_{180,80}$.

Using $FRF_{180,108}$, the resultant parameters of the application of the method are as follows in table 8.8.

Table 8.8: Evaluation of the direct frequency response identification method using $FRF_{180,108}$.

Parameter		Identified Parameter
E_0	/Pa	4.8052×10^5
E_∞	/Pa	6.6394×10^8
τ	/s	1.5245×10^{-6}
α		6.7230×10^{-1}

The graphs of the experimental FRF and numerical one are illustrated in figure 8.9. The level of correlation attained in both functions is present in figure 8.10.

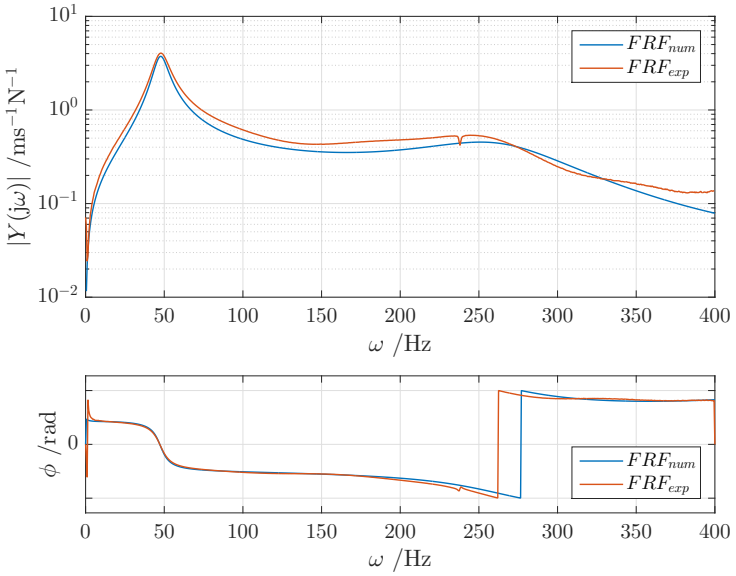

Figure 8.9: Experimental and identified $FRF_{180,108}$.

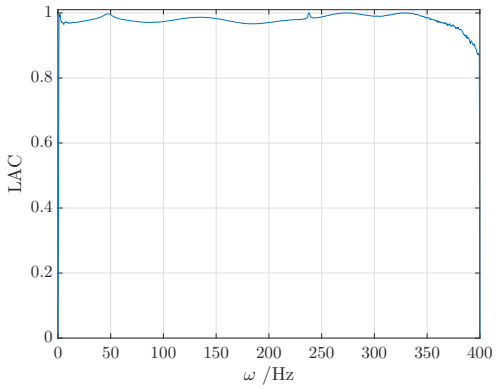

Figure 8.10: LAC for the $FRF_{180,108}$.

Using the direct frequency response function, the following parameters are determined:

Table 8.9: Evaluation of the direct frequency response method using the $FRF_{180,180}$.

Parameter		Identified Parameter
E_0	/Pa	6.6773×10^6
E_∞	/Pa	8.6970×10^8
τ	/s	1.0054×10^{-6}
α		6.7889×10^{-1}

The graphical results are demonstrated in both figure 8.11 and figure 8.12.

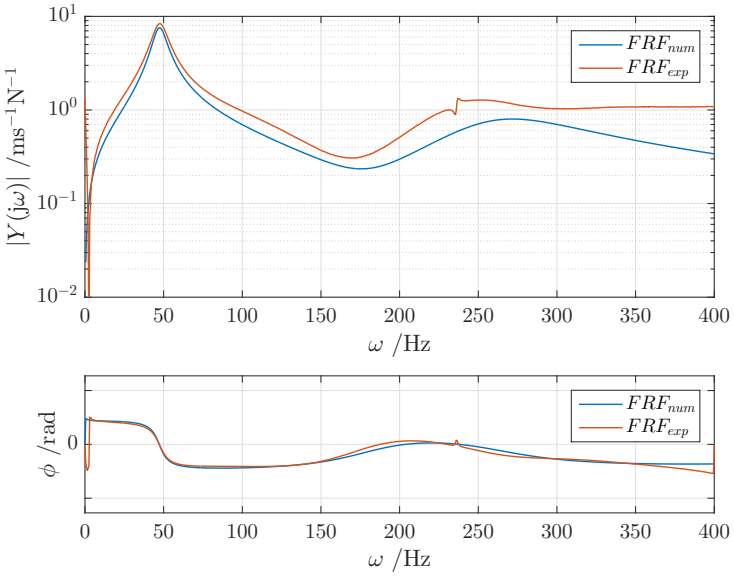

Figure 8.11: Experimental and identified $FRF_{180,180}$.

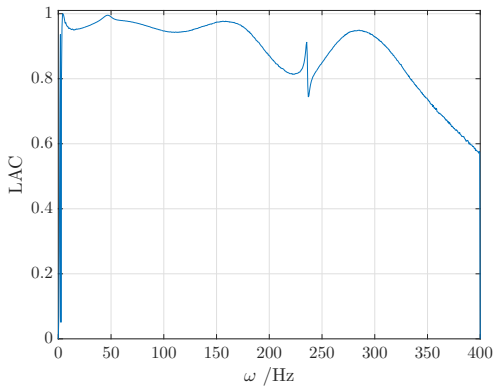

Figure 8.12: LAC for the $FRF_{180,180}$.

8.3.2 Composite Beam B

The application of the current identification method is performed for composite beam B using 15 control frequencies located in the bandwidth of [29 36] Hz, which corresponds to the first mode of vibration. The sampling frequency is, similarly to composite beam A, $\Delta f = 0.5$ Hz.

The results attained using $FRF_{220,88}$ are listed in table 8.10.

Table 8.10: Evaluation of the direct frequency response method using $FRF_{220,88}$.

Parameter		Identified Parameter
E_0	/Pa	7.4320×10^5
E_∞	/Pa	5.5540×10^8
τ	/s	6.5895×10^{-7}
α		6.0852×10^{-1}

Both FRF are depicted in figure 8.13 and the results of the quantitative comparison using the LAC is illustrated in figure 8.14.

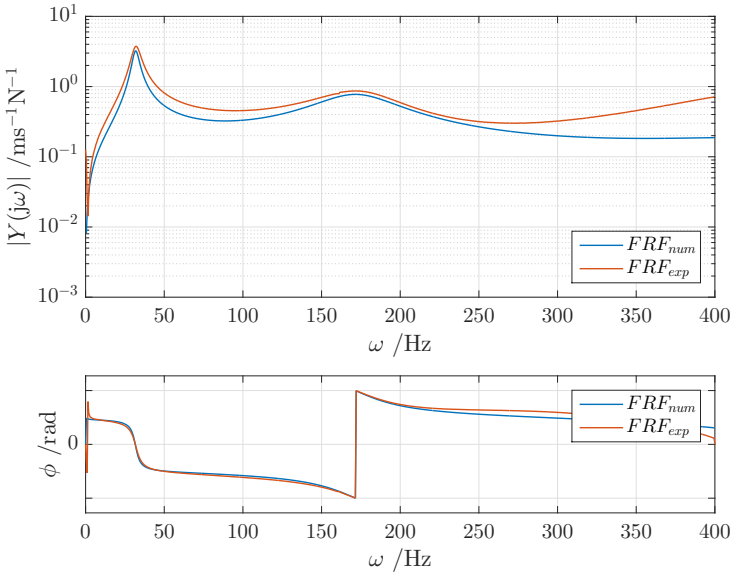

Figure 8.13: Experimental and identified $FRF_{220,88}$.

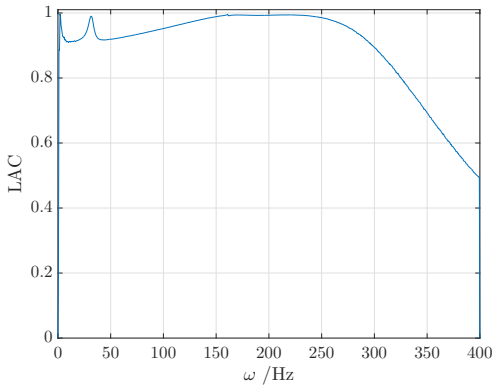

Figure 8.14: LAC for the $FRF_{220,88}$.

Using $FRF_{220,128}$ leads to the results exhibited in table 8.11.

Table 8.11: Evaluation of the direct frequency response method using $FRF_{220,128}$.

Parameter		Identified Parameter
E_0	/Pa	1.0490×10^6
E_∞	/Pa	9.6279×10^8
τ	/s	1.2114×10^{-6}
α		7.2407×10^{-1}

Figure 8.15 and figure 8.16 illustrate the graphical results of the direct frequency response method.

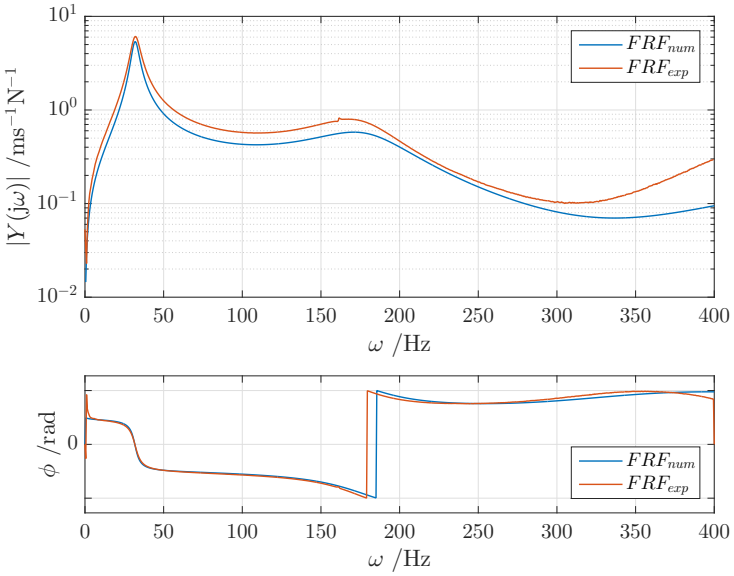

Figure 8.15: Experimental and identified $FRF_{220,128}$.

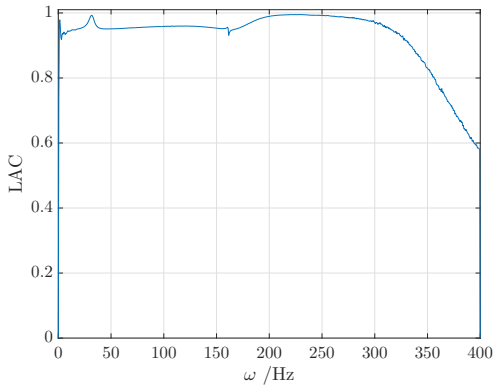

Figure 8.16: LAC for the $FRF_{l=220,l=128}$.

Using the direct frequency response function, the fractional derivative parameters that minimise experimental and the numerical FRF are summarised in table 8.12.

Table 8.12: Evaluation of the direct frequency response method using $FRF_{220,220}$.

Parameter		Identified Parameter
E_0	/Pa	9.3704×10^5
E_∞	/Pa	6.6171×10^8
τ	/s	6.6001×10^{-7}
α		6.3874×10^{-1}

Numerical and experimental FRF are illustrated in figure 8.17 and LAC results are present in figure 8.18.

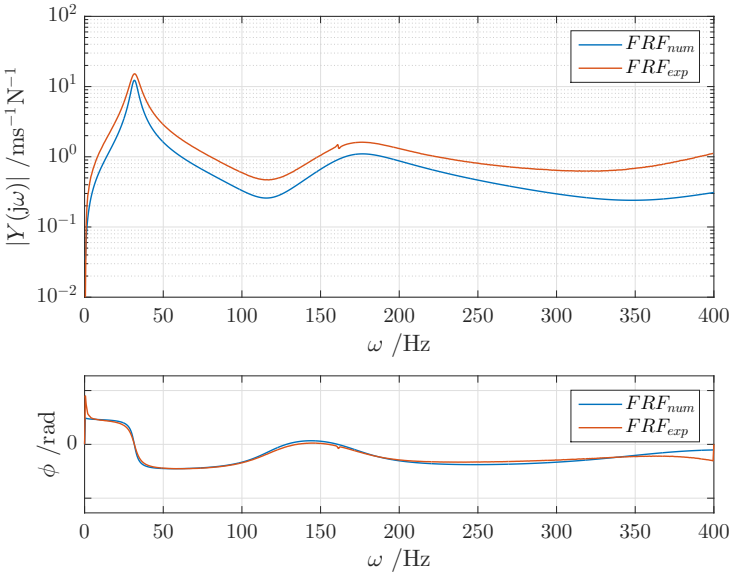

Figure 8.17: Experimental and identified $FRF_{220,220}$.

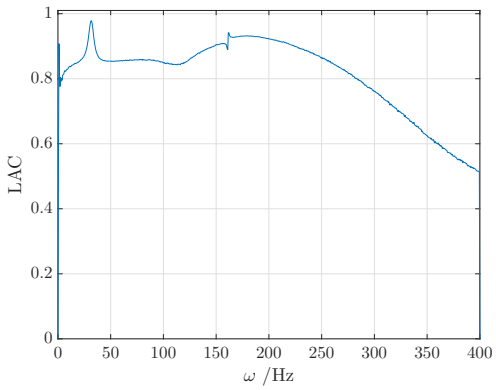

Figure 8.18: LAC for the $FRF_{220,220}$.

8.3.3 Composite Beam C

The application of the direct-frequency response identification method is evaluated for composite beam C using 15 control frequencies located in first resonance bandwidth: [22.25 25.75] Hz using a sampling frequency of $\Delta f = 0.25$ Hz. The results for such beam are shown in the current chapter following a similar procedure as the one used for the previous composite beams.

Using $FRF_{260,108}$ the parameters reached are the ones exposed in table 8.13.

Table 8.13: Evaluation of the direct frequency response method using $FRF_{260,108}$.

Parameter		Identified Parameter
E_0	/Pa	5.5936×10^5
E_∞	/Pa	6.9704×10^8
τ	/s	1.1918×10^{-6}
α		6.3660×10^{-1}

The graph of both FRFs is present in figure 8.19.

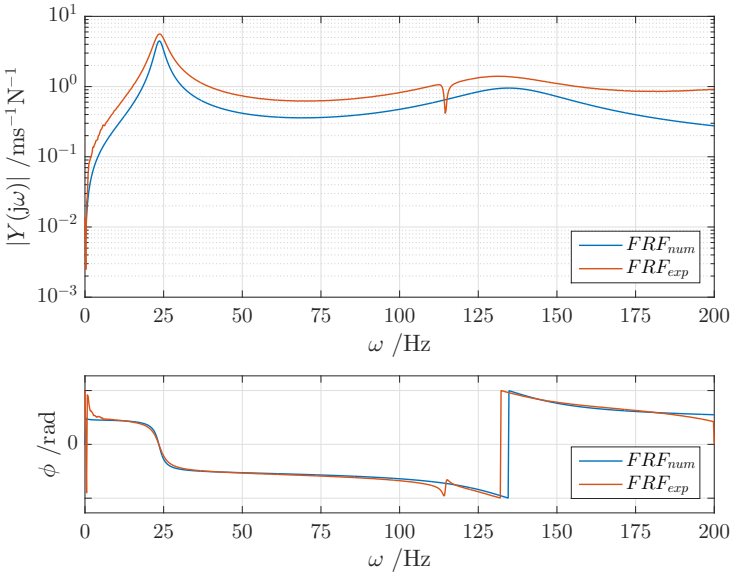

Figure 8.19: Experimental and identified $FRF_{260,108}$.

Performing the comparison of the two functions using LAC originates the results shown in figure 8.20.

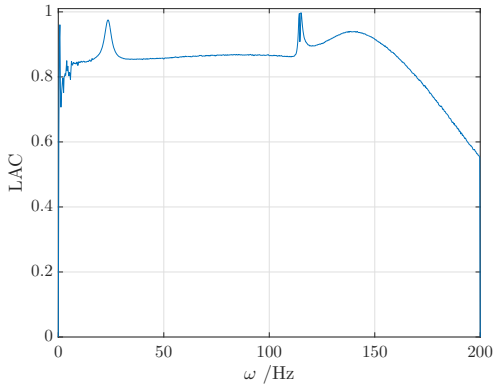

Figure 8.20: LAC for the $FRF_{260,108}$.

The application of function $FRF_{260,172}$ leads to the parameters written in table 8.14.

Table 8.14: Evaluation of the direct frequency response method using $FRF_{260,172}$.

Parameter		Identified Parameter
E_0	/Pa	8.2516×10^{5}
E_∞	/Pa	7.9945×10^{8}
τ	/s	9.7086×10^{-7}
α		6.8384×10^{-1}

Both FRFs are represented in figure 8.21 and the correlation level is indicated in figure 8.22 using the LAC.

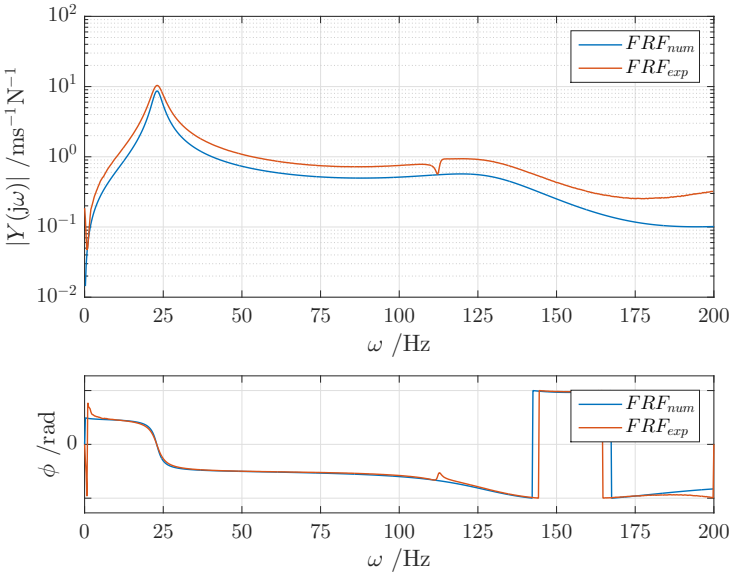

Figure 8.21: Experimental and identified $FRF_{260,172}$.

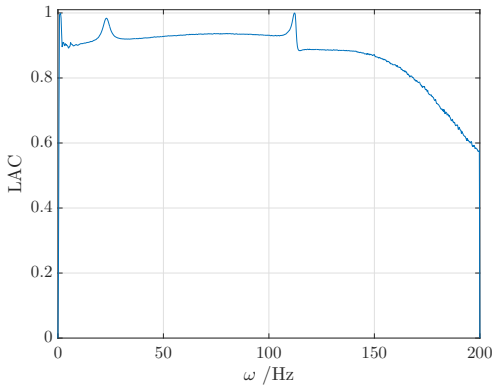

Figure 8.22: LAC for the $FRF_{260,172}$.

Using the direct FRF, the fractional derivative parameters reached are the ones present in table 8.15.

Table 8.15: Evaluation of the direct frequency response method using $FRF_{260,260}$.

Parameter		Identified Parameter
E_0	/Pa	4.4985×10^5
E_∞	/Pa	1.1295×10^9
τ	/s	1.5428×10^{-6}
α		7.0920×10^{-1}

The method leads, then, to the FRFs shown in figure 8.23 whose quantitative comparison is performed using the LAC and shown in figure 8.24.

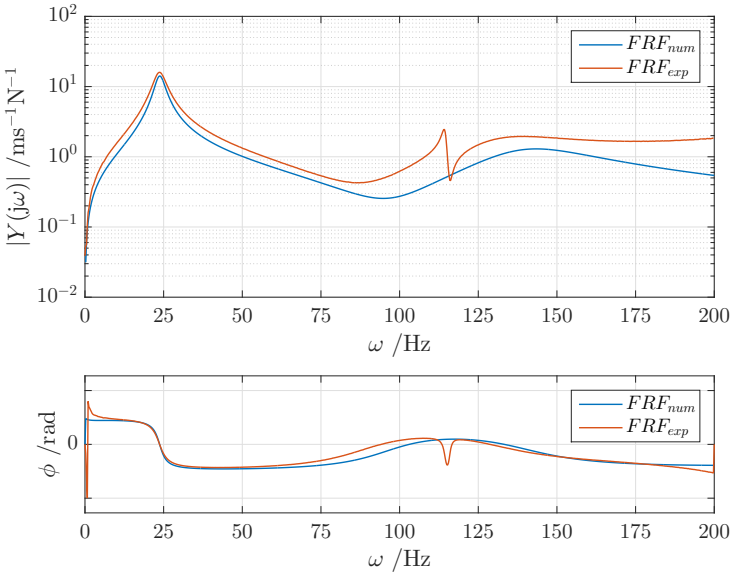

Figure 8.23: Experimental and identified $FRF_{260,260}$.

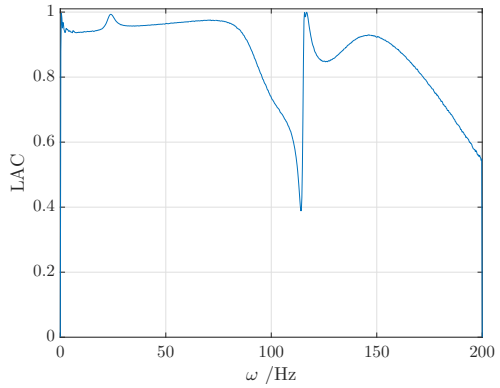

Figure 8.24: LAC for the $FRF_{260,260}$.

8.3.4 Notes on the results obtained for the composite beams

The application of the direct frequency response method on the composite beams shows an extreme dependence both on the frequencies of control selected and on the initial parameters given, as evidenced for the base beams.

When comparing the fractional derivative model parameters obtained for the same composite beam using different excitation points, slight differences between the values are noticeable. These differences are, however, magnified when comparing the values obtained for the various composite beams.

As for the comparison between the numerical and experimental FRFs, it is evident that the worst correlation level is attained for composite beam C, similarly to what is verified using the two-step identification method. Thus, it may be a result of defects on the sample which leads to poor experimental results. It is also noticeable that both functions diverge towards the end of the frequency bandwidth.

8.4 Identified Storage Modulus and Loss Factor

The frequency dependent properties identified for each composite beam using the distinct FRFs are present in figures 8.25 to 8.27.

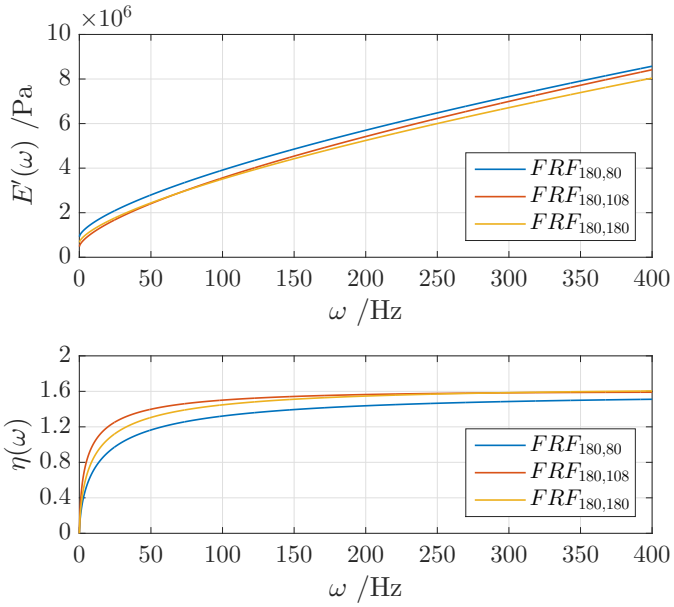

Figure 8.25: Identified storage modulus and loss factor of composite beam A.

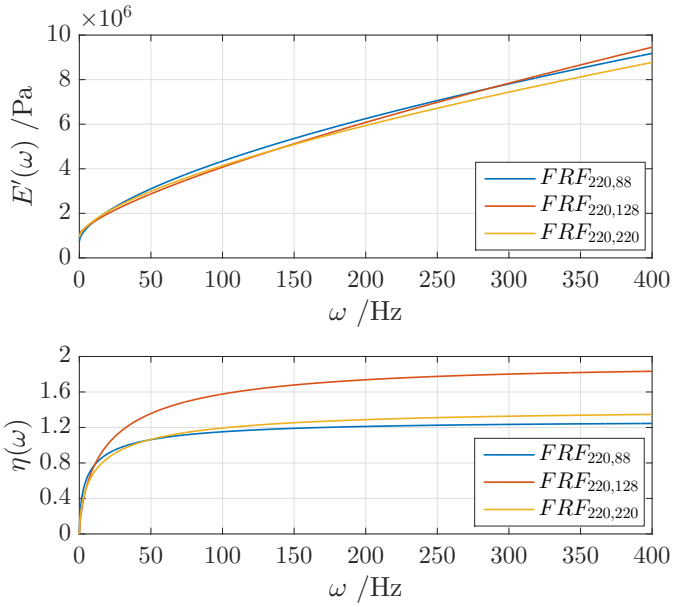

Figure 8.26: Identified storage modulus and loss factor of composite beam B.

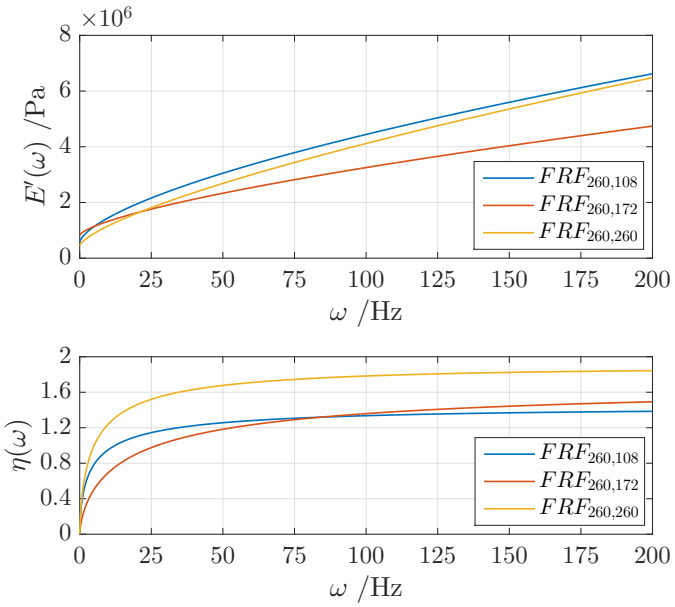

Figure 8.27: Identified storage modulus and loss factor of composite beam C.

The results obtained for composite beam A are quite impressive, as the three FRFs lead to similar results of storage modulus, $E'(\omega)$, and of loss factor, $\eta(\omega)$. As for the remaining composite beams, the frequency dependent properties reached are not coincident for all the FRFs.

The final values of the fractional derivative model parameters are then selected, similarly to what was performed for the two-step identification method, based on the FRF that exhibited the best correlation values. For the direct frequency response method, such function is the $FRF_{180,108}$ of composite beam A and the parameters' values are summarised in table 8.16. The storage modulus and loss factor identified are shown in figure 8.28.

Table 8.16: Identified fractional derivative model parameters for the viscoelastic material 3M ISD112 using the direct frequency response method.

Parameter		Value
E_0	/Pa	4.8052×10^5
E_∞	/Pa	6.6394×10^8
τ	/s	1.5245×10^{-6}
α		6.7230×10^{-1}

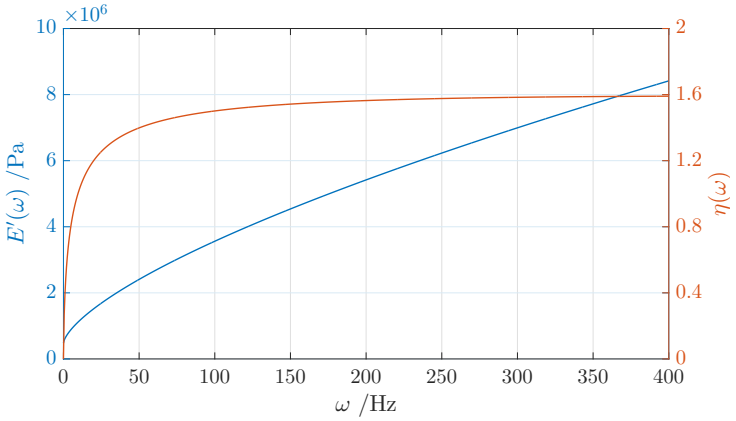

Figure 8.28: Identified storage modulus and loss factor using the Direct Frequency Response Method.

By way of comparison, in figure 8.29, the identified properties using both identification methods are represented. It is noticeable that the dynamic properties show the same tendency for increasing values of frequency. However, the numeric values reached for both $E'(\omega)$ and $\eta(\omega)$ are not coincident on both methods.

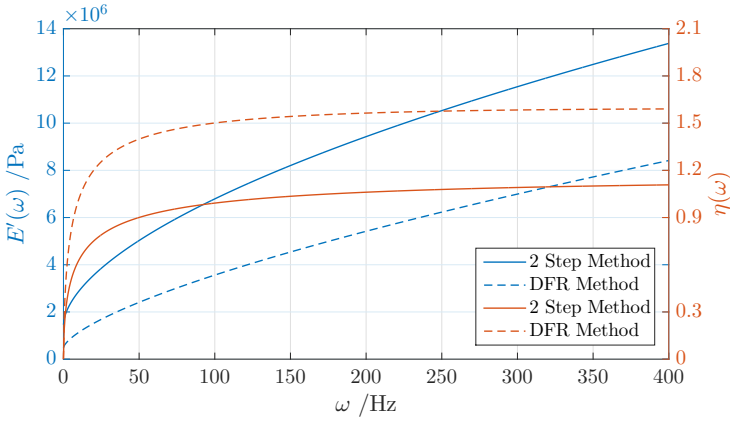

Figure 8.29: Identified properties from both identification methods implemented.

8.5 Influence of the number of control frequencies

Experiment shows that the identified parameters are quite dependent on the control frequencies chosen. Employing more that 15 control frequencies leads to a complete deterioration of the results. Moreover, the frequency range limited by the local maximum and minimum of the imaginary part of the FRF, for the sampling frequencies available, does not contain more than 15 frequencies. As such, two alternatives are tested:

- 3 control frequencies that correspond to the local maximum and minimum of the imaginary part of the mobilities and the resonant frequency;
- 9 control frequencies located in the local maximum and minimum of the imaginary part and containing the resonant frequency.

In order to portray the behaviour of the current method when a different number of control frequencies is used, the results of two FRFs will be shown in the current chapter: $FRF_{180,108}$ of composite beam A and $FRF_{220,128}$ of composite beam B. The remaining FRFs exhibit a similar behaviour and therefore their results are omitted.

As for the $FRF_{180,108}$, the results are shown in figure 8.30, where the plot of the generated FRF using 3, 9 and 15 control frequencies is illustrated as opposed to the one determined through experiment. The parameters obtained are listed in table 8.17.

Table 8.17: Identified parameters using a different number of control frequencies for $FRF_{180,108}$.

Parameter		3 Control Frequencies	9 Control Frequencies	15 Control Frequencies
E_0	/Pa	7.3158×10^5	5.8017×10^5	4.8052×10^5
E_∞	/Pa	9.6339×10^8	1.3243×10^9	6.6394×10^8
τ	/s	8.7240×10^{-7}	7.0359×10^{-7}	1.5245×10^{-6}
α		6.7039×10^{-1}	6.9435×10^{-1}	6.7230×10^{-1}

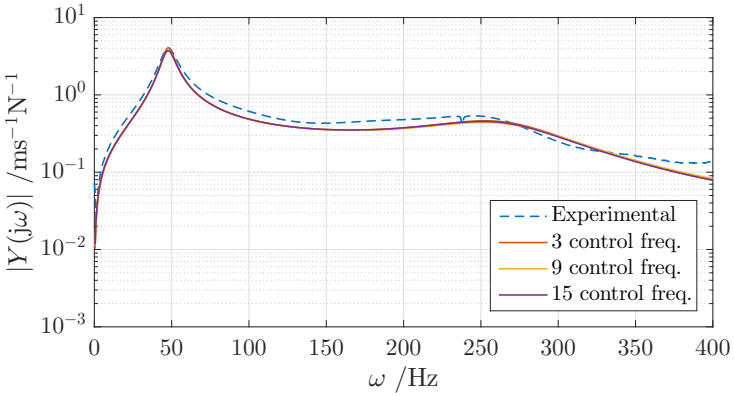

Figure 8.30: Influence of the number of modes in $FRF_{180,108}$.

Upon initial inspection of the graph illustrated in figure 8.30, the three generated functions seem undistinguishable. However when analysing the first resonant frequency bandwidth in detail, is verified that the lowest number of control frequencies leads to a better result in such range - figure 8.31.

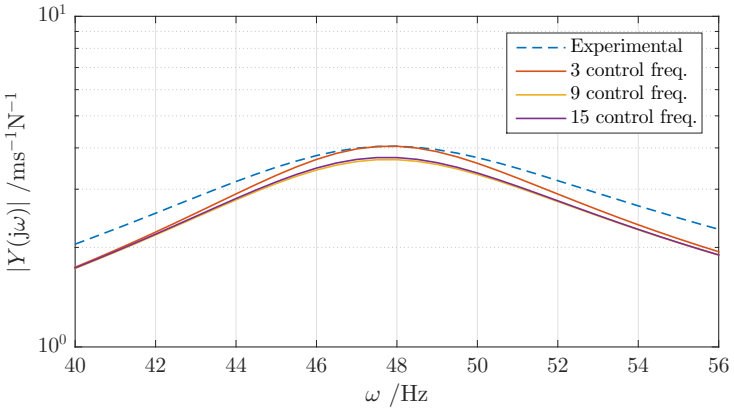

Figure 8.31: Detail of the first resonance frequency bandwidth of $FRF_{180,108}$.

For the $FRF_{220,128}$ the same occurrence is verified, the results attained when using merely

3 control frequencies lead to a generated FRF closer to the experimental function in the first natural frequency bandwidth, as shown in figure 8.32 and 8.33. The identified parameters are summarised in table 8.18.

Table 8.18: Identified parameters using a different number of control frequencies for $FRF_{220,128}$.

Parameter		3 Control Frequencies	9 Control Frequencies	15 Control Frequencies
E_0	/Pa	1.1455×10^6	8.7520×10^5	1.0490×10^5
E_∞	/Pa	6.7953×10^8	8.2266×10^8	9.6278×10^8
τ	/s	1.1546×10^{-6}	9.7854×10^{-7}	1.2114×10^{-6}
α		6.7638×10^{-1}	6.8358×10^{-1}	7.2407×10^{-1}

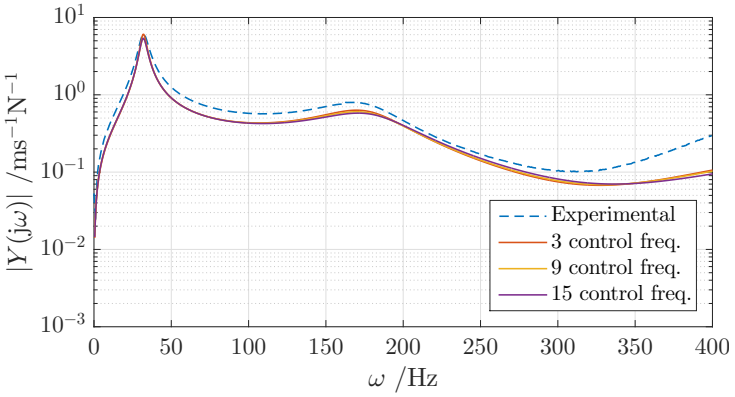

Figure 8.32: Influence of the number of modes in $FRF_{220,128}$.

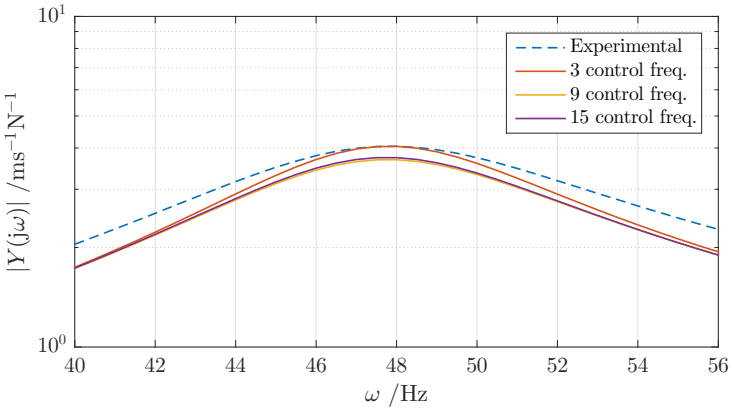

Figure 8.33: Detail of the first resonance bandwidth $FRF_{220,128}$.

To summarise, the application of the direct frequency response identification method is preferred when the minimisation function is evaluated in a small number of control frequencies. Even though, it shows only a slight improvement in terms of the results reached, the iteration time diminishes considerably.

8.6 Influence of the number of modes considered

In the current section, the direct frequency response identification method is applied using control frequencies located in two different resonant bandwidths.

Most of the FRFs obtained experimentally show a small disturbance around the second mode of vibration which must be avoided in order to accurately apply the current identification method.

The evaluation of the two modes of vibration in composite beam B is performed using $FRF_{180,108}$, leading to the results represented in figure 8.34. The frequency bandwidth considered on the first mode is [44 51] Hz and on the second mode is [247 254] Hz.

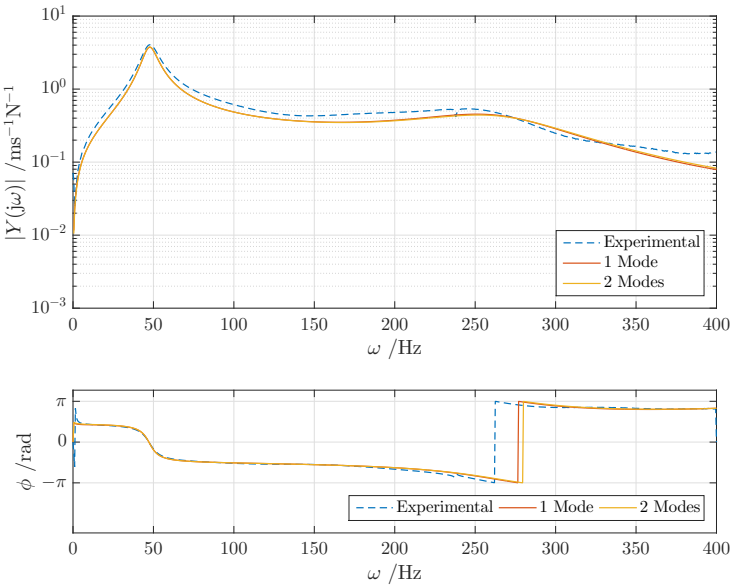

Figure 8.34: Influence of the number of modes in $FRF_{180,108}$.

Using $FRF_{220,128}$ for different number of modes considered leads to the results illustrated in figure 8.35. The control frequencies located in the first mode of vibration belong to the interval defined by [29 36] Hz, whereas the control frequencies of the second mode are located between [172.5 179.5] Hz.

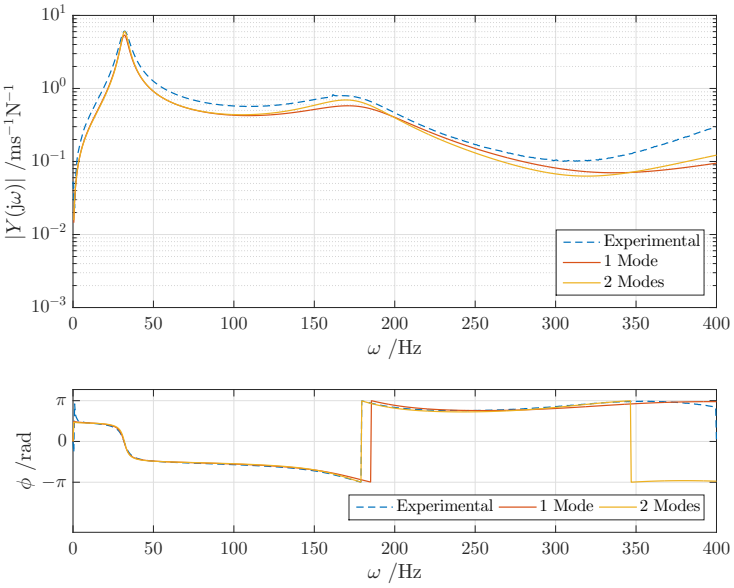

Figure 8.35: Influence of the number of modes in $FRF_{220,128}$.

The preceding results indicate that using a higher number of modes of vibration does not

improve the correlation between the numerical and the experimental FRFs, in fact, the generated functions using one and two modes of vibration are quite coincident.

8.7 Conclusions

The direct frequency response method is a conceptually simple method that only requires the evaluation of the minimisation function in a small number of control frequencies in order to obtain the fractional derivative model parameters.

As for the application of the current method in lightly damped systems, such as the bare aluminium beams, satisfactory levels of correlation are reached. Nonetheless, a slight disagreement between the numerically generated and experimental FRFs is visible around the second mode of vibration. Additionally, for the case of the direct FRF, it is perceivable that the anti-resonant bandwidth evidences a lower level of correlation. Indeed, that is a result of a small signal-to-noise ratio in such frequency bandwidth.

The employment of the current method in the sandwich beam's FRFs is more laborious and results in higher iteration times than that of the base beams. Furthermore, the levels of correlation between the functions are not as impressive. It is verified that, for the entire FRFs tested, the attained results are close to the experimental function, however, they show a slight deviation in magnitude that almost remains constant throughout the entire frequency bandwidth. It is seemingly resultant of the minimisation function that is not capable of finding a more fitted solution and converges on a local minimum.

The identified values of the frequency dependent properties of the viscoelastic material using the FRFs of composite beam A show a remarkable similarity in terms of both, storage modulus, $E'(\omega)$ and loss factor, $\eta(\omega)$. On the contrary, the ones resultant of composite beams B and C seem to be less precise.

As for more particular conclusions, throughout the validation of the method is perceptible that it shows a high dependence on both the initial estimation of the parameters and on the number of control frequencies on which the function is minimised. In fact, it is also concluded that an increase in the number of frequencies evaluated does not contribute to a better fitted solution. Using three control frequencies, as suggested by Martinez-Agirre and Elejabarrieta (2011), results in well correlated functions. The distribution of such control frequencies over two modes of vibration does not influence the final result. That is, the amplitude and phase information of the first mode of vibration, which is indubitably the one of most relevance, is sufficient to characterise the viscoelastic material in a broad range of frequencies.

Chapter 9

Transient Response

9.1 Introduction

As referred to in previous chapters, the dynamic analysis of composite structures that include a viscoelastic layer can be performed both in time or frequency domains. The first approach, however, usually conducts to viscoelastic models with higher order time derivatives that difficult the resolution of the differential equations of motion. Even though the introduction of models using fractional calculus decreases the order of the derivative term, the use of frequency domain constitutive models is the preferred method. That is because the mathematical formulation of the material's properties and the resolution of the equations of motion becomes simpler since operations such as integration and differentiation are transformed in division and multiplication by a $j\omega$ term. A consequence of the aforementioned is a lack of investigation of the efficiency of viscoelastic damping treatments in the time domain transient response when compared to the frequency response (Barkanov et al., 2000; Granger and Ross, 2009).

Alternatively, the transient response can be obtained firstly in the frequency domain and secondly in the time domain by means of an inverse Fourier transform. Thus preserving the simplicity of the frequency domain constitutive models and the DFA for the determination of the frequency displacement phasor (Khalfi and Ross, 2013).

Bearing such in mind, the current chapter aims to determine the transient response for composite beams with viscoelastic treatments, when the excitation for several load configuration. The implemented method is tested and validated with analytical solutions for a simple damped one DOF system and then hypothesised for the case of composite beams with different viscoelastic treatments.

9.2 Fourier Transform

Fourier transform represents the ground of frequency analysis in which every signal is analysed as a superposition of simpler waveform functions of different frequencies commonly written in the form of complex exponentials.

Thereby, the Fourier transform of a given signal in the time domain leads to its spectrum in the frequency domain. The analysis of the Fourier transform as a conversion between time and frequency domains is quite limiting, as the Fourier analysis can be performed in a wide number of problems, however, such is the case of the current work. As such, the terms time domain and input signal and frequency domain and output signal are from now on used interchangeably.

The reverse process, that is, the generation of a signal from its constituent exponentials can be performed using the inverse Fourier transform (Randall, 1987).

The underlying mathematical integral formulation of the Fourier transform and of the inverse Fourier transform is present in equation (9.1) and equation (9.2), respectively.

$$\mathfrak{F}[f(t)] = G(\omega) = \int_{-\infty}^{\infty} f(t)\mathrm{e}^{-\mathrm{j}\omega t}\ \mathrm{d}t. \tag{9.1}$$

$$\mathfrak{F}^{-1}[G(\omega)] = f(t) = \int_{-\infty}^{\infty} G(\omega)\mathrm{e}^{\mathrm{j}\omega t}\ \mathrm{d}\omega. \tag{9.2}$$

When the time domain and frequency domain functions are expressed as a form of discrete equally spaced terms in time or frequency, the integral formulation is replaced by the correspondent discrete formulation of the Fourier's transform. The discrete formulation is commonly expressed in literature, for N sampling points, in the following manner:

$$\mathfrak{F}[f(t)] = G(\omega_k) = \frac{1}{N}\sum_{n=0}^{N-1} f(t_n)\mathrm{e}^{-\mathrm{j}\frac{nk}{N}}, \tag{9.3}$$

$$\mathfrak{F}^{-1}[G(\omega)] = f(t_n) = \sum_{k=0}^{N-1} G(\omega_k)\mathrm{e}^{\mathrm{j}\frac{nk}{N}}, \tag{9.4}$$

where the parameter n is relative to a generic term of the time vector and assumes values from $n = 0, 1, \ldots, N-1$. The term k is relative to the frequency ω_k and assumes values between the interval $-\frac{N}{2} \leq k \leq -\frac{N}{2} - 1$ for an even number of sampling points and $-\frac{N}{2} \leq k \leq -\frac{N}{2}$ for an odd number of sampling points (Hover and Chin, 2009; Thrane, 1979).

The determination of the discrete forms of the Fourier transform is obtained in the current work using a Fast Fourier Transform (FFT) algorithm. In `Matlab`® this algorithm corresponds to the function *fft* for the Fourier transform and the function *ifft* for the inverse Fourier transform. The FFT algorithm represents a more efficient calculation procedure to obtain the discrete Fourier transform than the direct evaluation of equations (9.3) and (9.4) for the case of N being written as a power of two.

The computation of the FFT using `Matlab`® is performed according to the following expressions:

$$G(\omega_k) = \sum_{n=0}^{N-1} f(t_n)\mathrm{e}^{\frac{-\mathrm{j}kn}{N}}, \tag{9.5}$$

$$f(t_n) = \frac{1}{N}\sum_{k=0}^{N-1} G(\omega_k)\mathrm{e}^{\frac{\mathrm{j}kn}{N}}. \tag{9.6}$$

From equation (9.5) is noticeable that the FFT definition does not include the factor $\frac{1}{N}$ present in equation (9.3) and that such factor is corrected in the inverse Fourier transform (Bracewell, 2000; Hover and Chin, 2009). However, if the evaluation of the discrete Fourier transform is to be implemented as an approximation of the continuous formulation, expressed in equation (9.1), the correct scaling of the result of the evaluation of the *fft* function in `Matlab`® is obtained by multiplying the result by the sampling period of the function, Δt.

In most practical cases, the input series, which corresponds to the function values written in the time domain, are real values and the output series will be complex values. Thus, the imaginary components of the input series is zero and consequently the output's negative frequency spectrum values correspond to the complex conjugate of the positive frequency values. The FFT algorithm already takes the aforesaid considerations into account thus contributing to the increase of the computational efficiency (Randall, 1987).

9.3 Method Description

For the case of a system with n degrees of freedom and a viscoelastic damping treatment, such as the composite beams tested in the current work, the equations of motion in the frequency domain can be written as evidenced in equation (9.7).

$$-\omega^2[M]\{\bar{X}(\omega)\} + [K^*]\{\bar{X}(\omega)\} = \{F\}, \tag{9.7}$$

where $[K^*]$ is a complex frequency dependent stiffness matrix, $[M]$ is the mass matrix and $\{F\}$ is the load vector. The exterior load is mathematically formulated as a rectangular pulse in the time domain according to the following equation:

$$f(t) = \begin{cases} F_0, & t \leq t_c \\ 0, & t \geq t_c \end{cases}, \tag{9.8}$$

where F_0 is the magnitude of the applied load and t_c the actuation time of the transient.

The force is converted to the frequency domain using Fourier's transform as evidenced in equation (9.9).

$$F(\omega) = \mathfrak{F}[f(t)]. \tag{9.9}$$

Since the evaluation of the Fourier transform is performed using an FFT algorithm that requires an input vector at discrete periods of time, equation (9.8) needs to be sampled. The number of sampling points, N, and the time increment, Δt are then defined which conducts to a sampling frequency - Nyquist frequency - of $f_s = \frac{1}{\Delta t}$.

According to the Nyquist sampling theorem, in order to avoid the introduction of error due to the misidentification of the signal's frequency - refered to as *aliasing* - the sampling frequency should be greater than or equal to twice the maximum value of frequency evaluated. Additionally, the frequency spectrum of the output signal of the Fourier transform includes negative frequencies, a 0 Hz frequency and positive frequencies. Hence, the frequency domain can be defined as a symmetric domain of $[-\Omega, \Omega]$ and, consequently, the frequency increment to sample such domain can be determined:

$$\Delta\omega = \frac{2\pi}{\Delta t(N-1)} \text{ [rad/s]}. \tag{9.10}$$

The sampled frequencies considered differ when an odd or even number of sampling points are used. The frequency vector is organised in a particular manner: first introducing the null and positive frequencies and then the negative frequencies. The frequency vector is expressed in equation (9.11).

$$\begin{cases} \omega = \left\{ \begin{array}{ccccccc} 0 & 1 & \dots & \frac{N-1}{2} & \frac{1-N}{2} & \dots & -1 \end{array} \right\} \Delta\omega, & \text{for an odd N.} \\ \omega = \left\{ \begin{array}{ccccccc} 0 & 1 & \dots & \frac{N}{2}-1 & \frac{-N}{2} & \dots & -1 \end{array} \right\} \Delta\omega, & \text{for an even N.} \end{cases} \tag{9.11}$$

The result of the Fourier transform expressed in equation (9.9) is placed in the load vector, $\{F\}$, in the corresponding degree of freedom. The system of equations is then solved and the displacement phasor vector, $\bar{X}(\omega)$, is determined. The transient response in the time domain with null initial conditions is finally reached according to equation (9.12).

$$x(t) = \mathfrak{F}^{-1}[\bar{X}(\omega)]. \tag{9.12}$$

A flowchart of the implemented method is shown in figure 9.1.

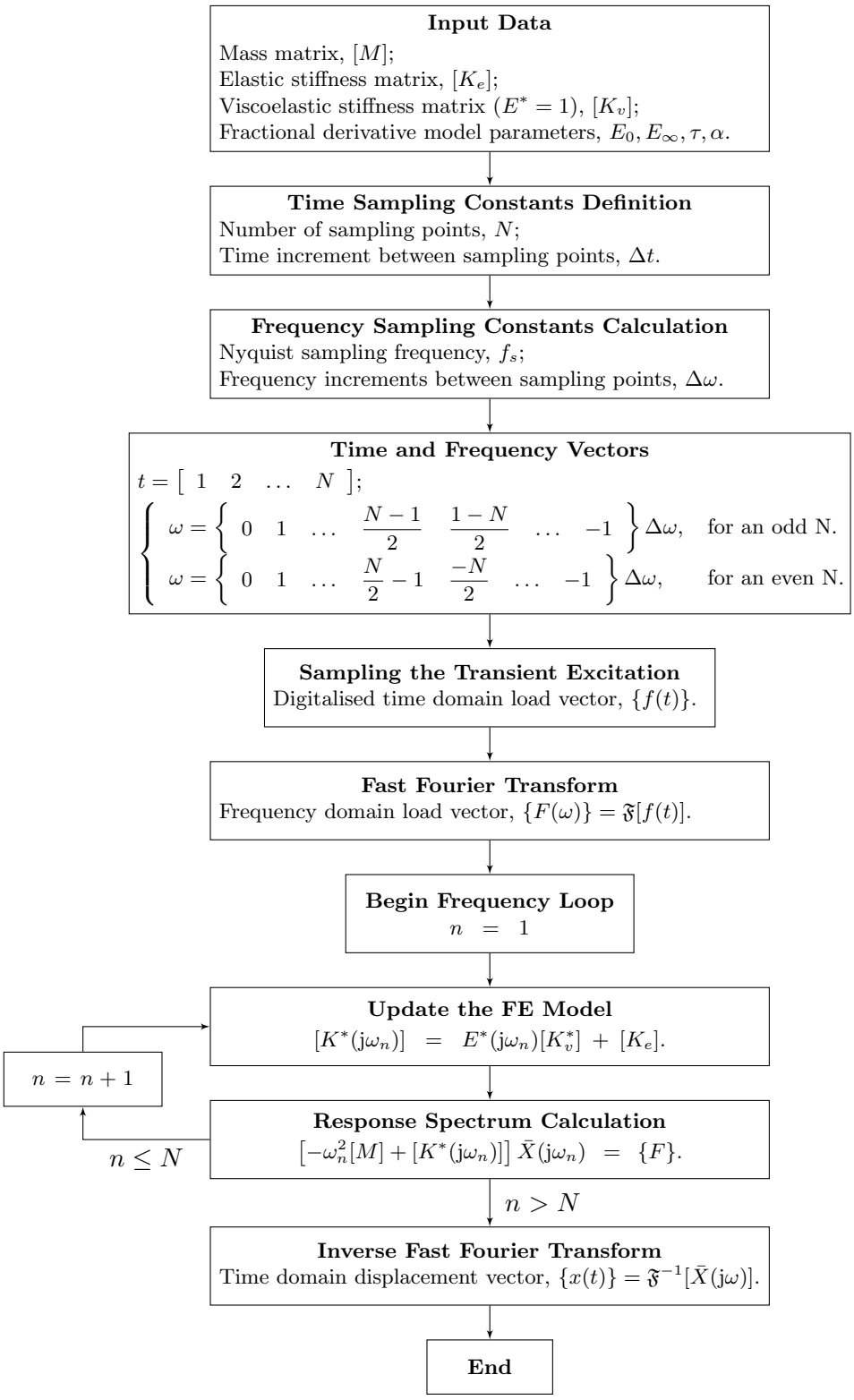

Figure 9.1: Diagram of the implemented method.

9.3.1 Causality

The application of such method on viscoelastic materials can lead to non-causal transient responses, which are identified by the fact that in $t = 0$ s the system assumes a non-zero displacement even though null initial conditions are considered. Thus, evidencing a physically incoherent behaviour.

Barkanov (1999) attributes the major cause of non-causality effects to the mathematical model of the viscoelastic material. That is, when the viscoelastic properties are assumed to be frequency independent, the results are unrealistic and non-causal responses are attained. As such, the model implemented must take into account the dependence of the properties with frequency as well as guarantee a real time domain behaviour (Granger and Ross, 2009).

In the work of Granger and Ross (2009), where a frequency dependent viscoelastic model is implemented, the non-causality effects are attributed to the FFT. It is stated that the response of the system must completely dissipate during the simulation time otherwise, the system will exhibit a non-causal displacement for $t = 0$ s. As one can anticipate, for lightly damped structures, a considerable number of sampling points must be selected - if one wishes to maintain the time resolution - in order to get a greater simulation time. Inevitably leading to time and memory consuming simulations.

9.4 One DOF system with viscous damping

Concerning the validation of the method previously detailed, a discrete one degree of freedom system, as illustrated in figure 9.2, is considered.

The analysis of the transient response using the Fourier transform for undamped systems produces poor results as a consequence of the discontinuity of the displacement phasor, $\bar{X}(\omega)$, present on the resonance frequency. Therefore, a proportionally damped system is hypothesised.

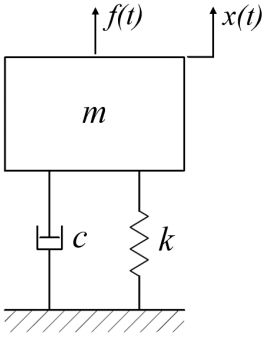

Figure 9.2: Vibratory system of one DOF.

The equation of motion of such system in the frequency domain is expressed as follows:

$$-\omega^2 m\bar{X}(\omega) + \mathrm{j}\omega cX(\omega) + k\bar{X}(\omega) = F, \tag{9.13}$$

where k is the stiffness constant of the elastic component, c the damping constant, m is the value of the discrete mass and F the exterior load.

The analytical transient response to a rectangular pulse, as the one formulated in equation (9.8), is determined using the Duhamel convolution integral in the time domain and is expressed in equation (9.14) for $0 < t \leq t_c$ and in equation (9.15) for $t > t_c$.

$$x(t) = \frac{F_0}{k}\left[1 - \mathrm{e}^{-\xi\omega_n t}\left(\frac{\xi}{\sqrt{1-\xi^2}}\sin\omega_d t + \cos w_d t\right)\right], \tag{9.14}$$

$$\begin{aligned} x(t) = &\frac{F_0}{k}\mathrm{e}^{-\xi\omega_n t}\left[-\cos\omega_d t - \frac{\xi}{\sqrt{1-\xi^2}}\sin\omega_d t\right. \\ &\left.+\mathrm{e}^{\xi\omega_n t_c}\left(\cos\omega_d(t-t_c) + \frac{\xi}{\sqrt{1-\xi^2}}\sin\omega_d(t-t_c)\right)\right], \end{aligned} \tag{9.15}$$

where ξ is the damping ratio, ω_n the undamped natural frequency and ω_d the damped natural frequency.

The system's properties are summarised in table 9.1. The numerical treatment is performed using $N = 2^{10}$ sampling points and a time increment of $\Delta t = 0.01$ s. The sampling constants are selected so that the response of the system vanishes in the time domain considered.

Table 9.1: 1 DOF system properties.

Property		Value
m	/kg	5
k	/Nm^{-1}	500
c	/Nsm^{-1}	15

The unitary rectangular pulse with an actuation time of $t_c = 4$ s is shown in figure 9.3a in the time domain and in figure 9.3b in the frequency domain.

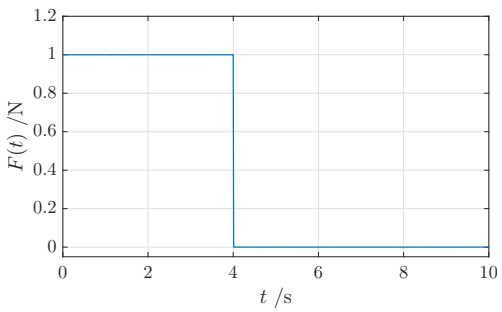

(a) Applied pulse in the time domain.

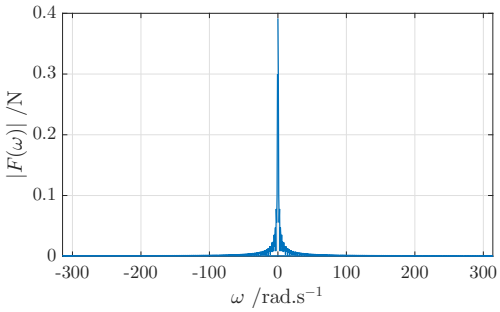

(b) Rectangular pulse in the frequency domain.

Figure 9.3: Impulsive force in time and frequency domains.

The transient response attained after the application of the inverse Fourier transform is evidenced in figure 9.4. As is perceptible, the correlation between the analytical solution using Duhamel's integral and the response resultant of the Fourier transform is almost perfect.

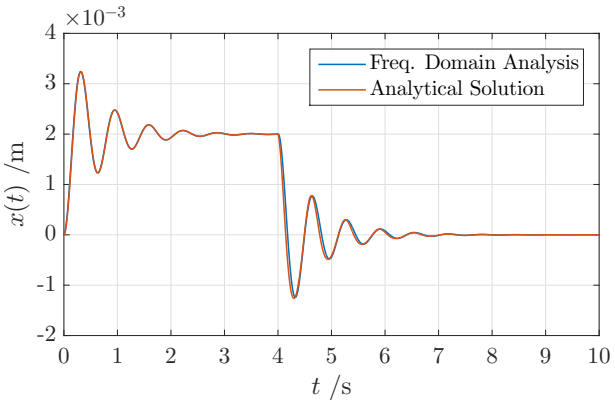

Figure 9.4: Transient response of the 1 DOF system.

The representation of the maximum response for different durations of the rectangular pulse and for several damping ratios using the implemented method is plotted in figure 9.5.

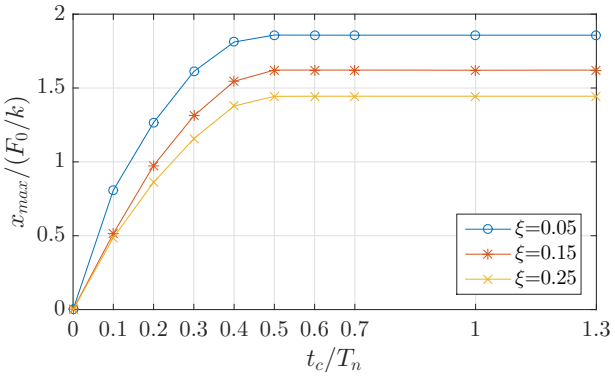

Figure 9.5: Transient response spectrum to the rectangular pulse for different damping ratios.

The result attained is coherent since, for $t_c < \frac{T_n}{2}$, an increase in the transient time conducts to superior amplitude responses, whereas, for $t_c \geq \frac{T_n}{2}$, the maximum response remains constant for increasing actuation periods. It can be assumed the validity of the implemented methodology for obtaining the response of damped systems.

9.5 Composite structures

The transient response of composite beams with viscoelastic damping treatments will be evaluated in the current chapter. The beam is considered to be clamped at the root end and free at the opposite one and the viscoelastic material contemplated is the 3M ISD112 whose properties are identified using the two-step identification method and are summarised in table 9.2. The transient response is then determined at the free end of each beam. The host structure and constraining layers are assumed to be aluminium whose Young's modulus is, as identified in previous chapters, $E = 61$ GPa.

Table 9.2: 3M ISD112 fractional derivative model parameters.

Parameter		Value
E_0	/Pa	1.4540×10^6
E_∞	/Pa	1.0474×10^9
τ	/s	3.9301×10^{-7}
α		5.7791×10^{-1}

The numerical treatment is performed using a constant time increment of $\Delta t = 0.001$ s. The number of sampling points of the continuous functions is selected according to the time range necessary do show the complete dissipation of the transient response of the system.

The unitary transient load considered is applied at the free end of the beam and has a duration of 1 s. The temporal and frequency representation of the exterior load are shown in figure 9.6a and figure 9.6b, respectively.

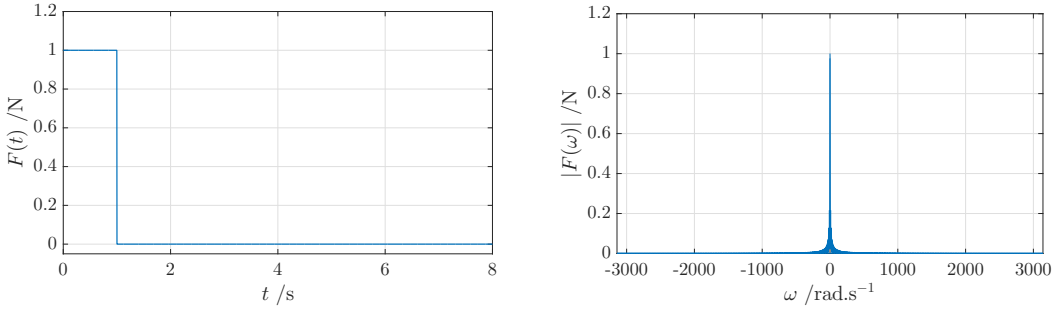

(a) Applied pulse in the time domain. (b) Rectangular pulse in the frequency domain.

Figure 9.6: Impulsive force in time and frequency domains.

The response at the free end of the beam is evaluated for different viscoelastic treatments: free layer damping treatments, constrained layer damping treatments and integrated layer damping treatments. Thus allowing to compare the damping efficiency of different treatment configurations.

The beams considered have a length, l, of 250 mm and a cross section width, b, of 15 mm. For finite element model application the beams are divided in 50 elements of 5 mm each.

The free layer damping treatment considered is illustrated in figure 9.7. The dimensions of the composite structure are summarised in table 9.3.

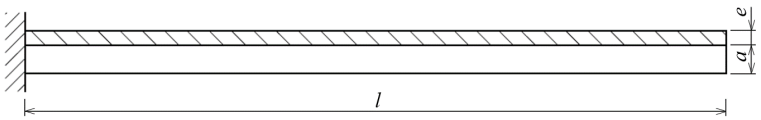

Figure 9.7: Illustration of the composite beam with a free layer viscoelastic treatment.

Table 9.3: Dimensions of the considered beam with a free layer viscoelastic treatment.

Dimension	Value [mm]
l	250
a	2
e	0.250
b	15

For transient response determination, $N = 2^{21}$ sampling points are considered and the result is represented in figure 9.8.

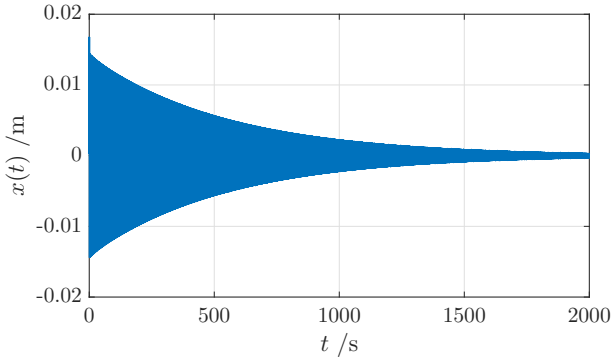

Figure 9.8: Transient response of a beam with a FLD treatment with $e = 0.250$ mm.

It is noticeable a decay in the response of the structure, however, a long period of time - more than 2000 s - is necessary to completely halt the oscillatory movement. An increase of efficiency of the damping treatment is expected for thicker viscoelastic layers. As such, in figure 9.9 is shown the response of the considered beam when a thicker layer of viscoelastic material is applied, that is, $e = 0.375$ mm.

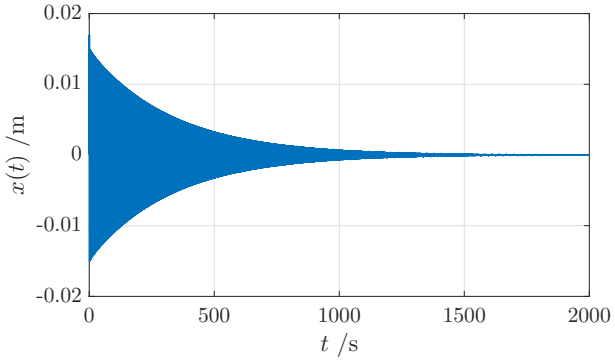

Figure 9.9: Transient response of a beam with a FLD treatment with $e = 0.375$ mm.

It is confirmed that the transient response possesses a faster amplitude decrease even though the maximum amplitude reached is similar to the one where a thinner viscoelastic layer is applied. That indicates a greater energy dissipation which results in a more efficient damping treatment.

In order to induce a higher deformation of the viscoelastic material, a restraining metallic layer can be placed. The beam with a CLD treatment considered is illustrated in figure 9.10. The dimensions of the composite structure are shown in table 9.4.

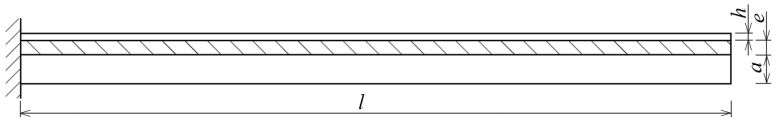

Figure 9.10: Illustration of the composite beam with a constrained viscoelastic treatment.

Table 9.4: Dimensions of the considered beam with a constrained viscoelastic treatment.

Dimension	Value [mm]
l	250
b	15
a	2
e	0.125
h	0.250

The transient response is attained with 2^{13} sampling points and is shown in figure 9.11.

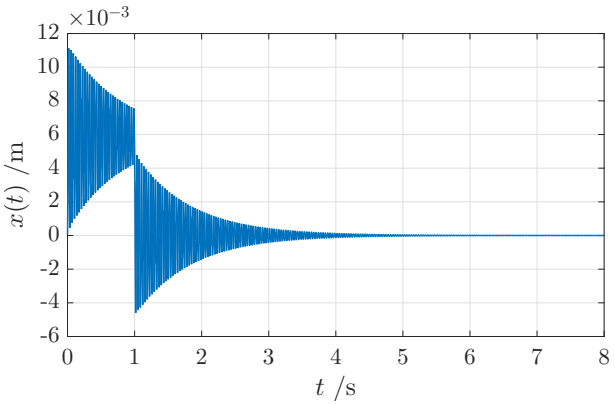

Figure 9.11: Transient response of a beam with a CLD treatment with $e = 0.125$ mm.

It is perceivable that the time necessary to extinguish the vibration of the beam is considerably inferior, only approximately 8 s, when compared to the time domain necessary for beams with an FLD treatment. Thereby, a higher damping capacity is attained with smaller thicknesses of the viscoelastic layer.

Considering twice the thickness of the viscoelastic material, which corresponds to 0.250 mm, a greater energy dissipation is achieved and, therefore, a faster response decay is visible in figure 9.12.

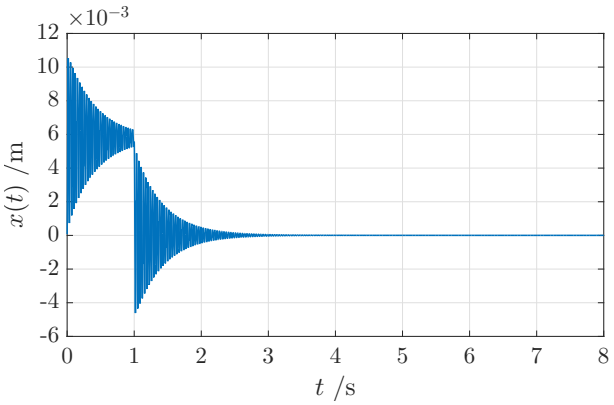

Figure 9.12: Transient response of a beam with a CLD treatment with $e = 0.250$ mm.

In figure 9.13, the transient response of both beams with CLD treatments considered are shown in greater detail to accurately confirm the effects of the thickness on the damping properties of the system.

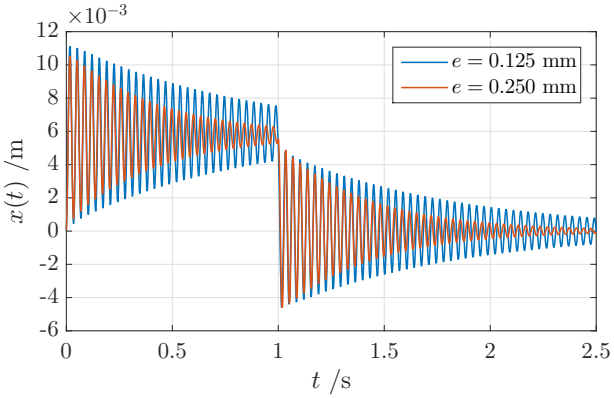

Figure 9.13: Transient response of CLD beams with two viscoelastic layer's thicknesses.

Contemplating the effects of the variation of the thickness of the restraining layer, a beam with an ILD treatment is evaluated, that is, the limit case where the restraining layer is as thick as the host structure. The beam's dimensions are identified in figure 9.14 and its numeric values summarised in table 9.5.

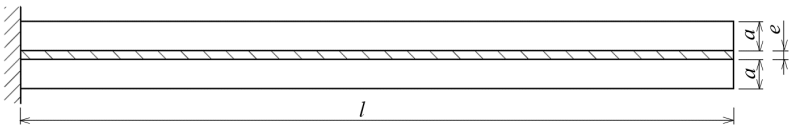

Figure 9.14: Schematic illustration of the composite beam with an integrated layer damping treatment.

Table 9.5: Dimensions of the considered beam with an integrated viscoelastic treatment.

Dimension	Value [mm]
l	250
e	0.125
h	2
b	15

The resulting transient response to the rectangular pulse considered is shown in figure 9.15. The time bandwidth plotted is inferior to the one shown for the beams with CLD treatments in order to more evidently show the transient behaviour of the system, although $N = 2^{13}$ sampling points are used also.

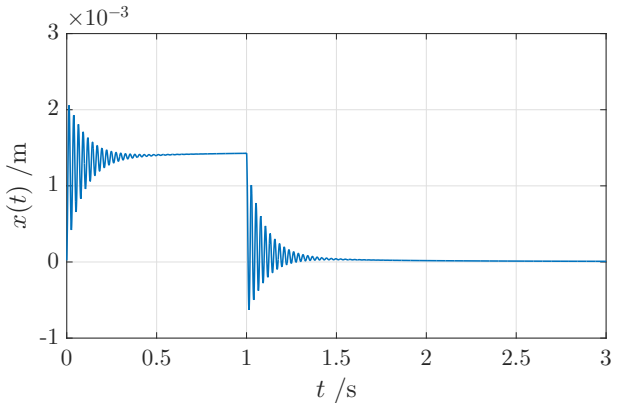

Figure 9.15: Transient response of a beam with an ILD treatment.

It is noticeable that the efficiency of the viscoelastic treatment has dramatically increased: the response of the system is vanished within the transient load application period.

In this configuration, the increase of the thickness of the restraining layer to a value similar to the thickness of the host beam, leads to a sandwich structure in which the viscoelastic layer is placed in the neutral plane of bending. In this plane is where the maximum shear deformation occurs, thus conducting to the maximum deformation of the viscoelastic layer, which explains its high efficiency.

9.5.1 Different load configurations

In view of approximating the numerical excitation force to the impulse that can experimentally be induced in the system, two transient loads are considered as opposed to the rectangular pulse previously suggested: a triangular transient pulse and half a sine wave pulse. For the evaluation of the response of a composite structure with a viscoelastic material to such exterior loads, the previously considered beam with a CLD treatment and a viscoelastic thickness of $e = 0.250$ mm is treated.

The triangular load is described in equation (9.16) and illustrated in figure 9.16:

$$f(t) = \begin{cases} \dfrac{F_0}{t_1} & 0 \leq t \leq t_1 \\ -\dfrac{F_0}{t_2 - t_1} t + \dfrac{F_0}{1 - \dfrac{t_1}{t_2}} & t_1 \leq t \leq t_2 \\ 0 & t \geq t_2 \end{cases} \tag{9.16}$$

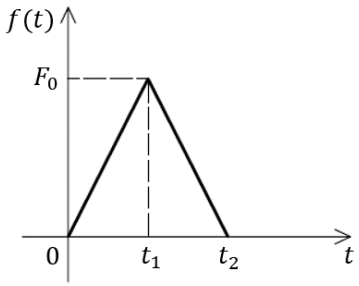

Figure 9.16: Triangular impulse.

The numerical treatment is performed using 2^{13} sampling points and a time increment of $\Delta t = 0.001$ s. It is considered a unitary impulse ($F_0 = 1$ N) where $t_1 = 0.05$ s and $t_2 = 0.1$ s. The induced loads are shown in the time and frequency domain in figures 9.17a and 9.17b, respectively.

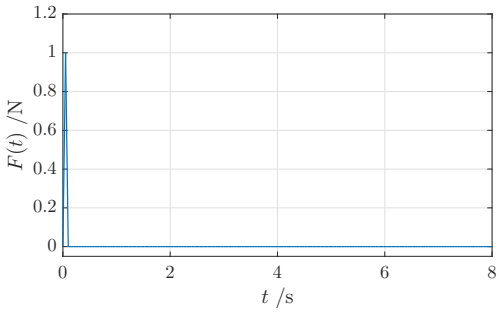

(a) Applied pulse in the time domain.

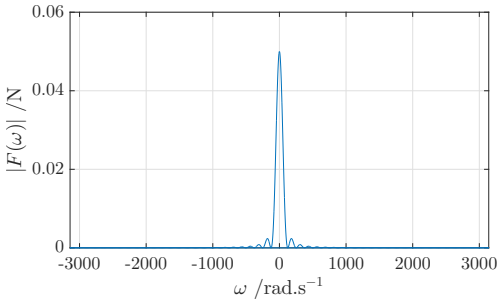

(b) Applied pulse in the frequency domain.

Figure 9.17: Triangular impulsive force in time and frequency domains.

The transient response is then shown in figure 9.18 for the entire simulation time considered. In figure 9.19 is shown a detail of the first 0.5 s of oscillatory movement.

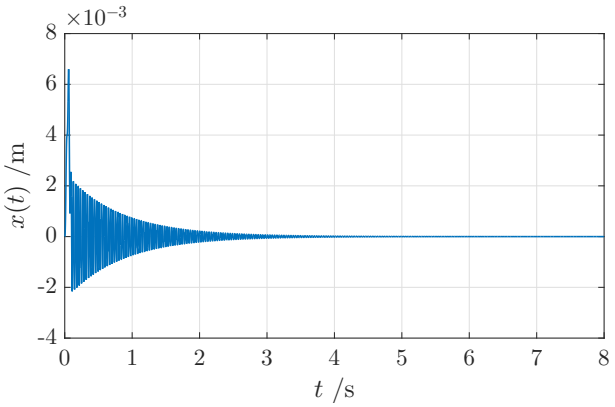

Figure 9.18: Transient response of a beam with a CLD treatment with $e = 0.250$ mm for a triangular impulse.

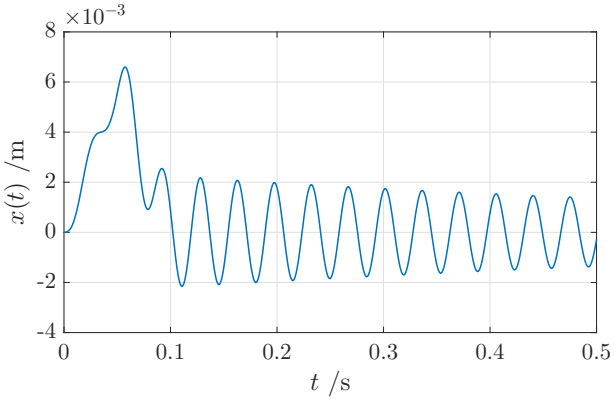

Figure 9.19: Detailed transient response of a beam with a CLD treatment with $e = 0.250$ mm for a triangular impulse.

It can be verified that the duration of the transient load is superior to half of the system's vibration period. Therefore, the system acquires the maximum amplitude response within such period.

As previously stated, the method is also evaluated using half a sine wave, which is described by the following equation:

$$f(t) = \begin{cases} F_0 \sin \dfrac{\pi}{t_c} t, & 0 \leq t \leq t_c \\ 0 & t \geq t_c \end{cases} \tag{9.17}$$

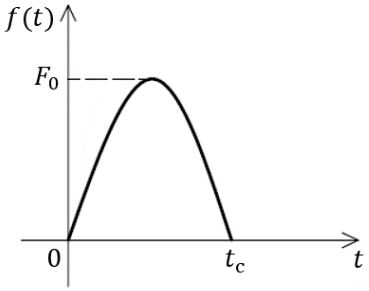

Figure 9.20: Half sine wave impulse.

The numerical treatment is performed using 2^{13} sampling points and a time increment of $\Delta t = 0.001$ s. It is considered an unitary impulse with a duration time of $t_c = 0.1$ s.

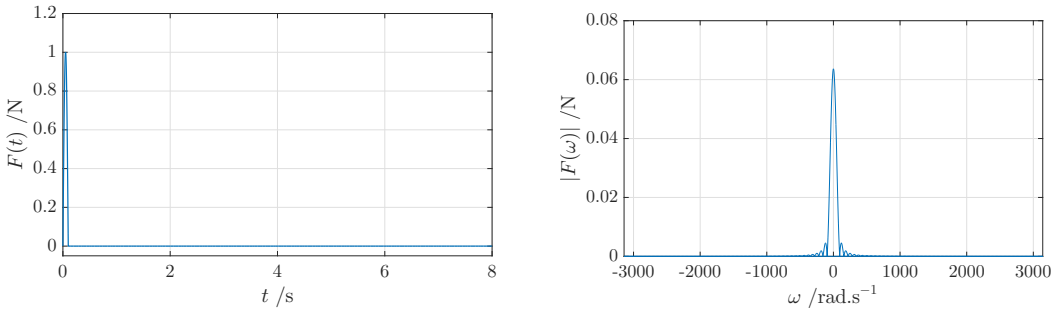

(a) Applied pulse in the time domain.

(b) Applied pulse in the frequency domain.

Figure 9.21: Half sine wave impulsive force in time and frequency domains.

The transient response attained is shown in figure 9.22.

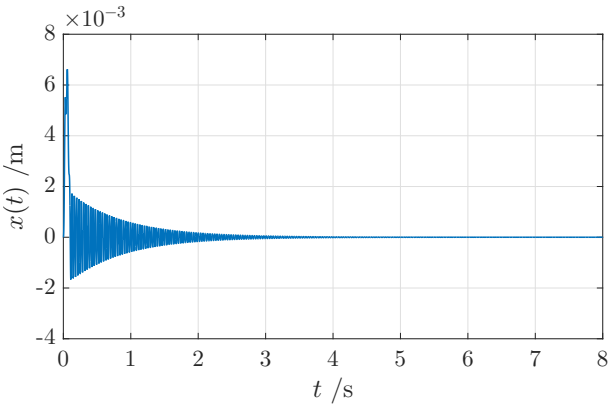

Figure 9.22: Transient response of a beam with a CLD treatment with $e = 0.250$ mm for a half sine wave impulse.

In figure 9.23 the transient response is shown in greater detail.

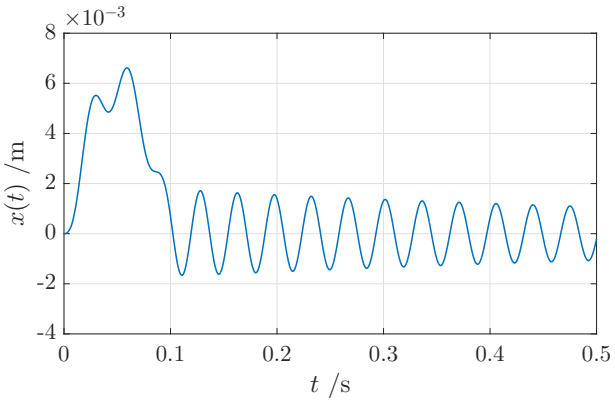

Figure 9.23: Detailed transient response of a beam with a CLD treatment with $e = 0.250$ mm for a triangular impulse.

9.6 Partial Treatments

In the current section, the transient response of composite beams with different partial treatment configurations is addressed. For that, several composite beams with CLD partial treatments are considered. Such beams are assumed to be clamped at the root end and free at the opposite one and the response is determined at the free end of the beam. The viscoelastic material considered is the 3M ISD112, whose parameters of the fractional derivative model are listed in table 9.2 of the previous section.

The length of the host beam, l, the thickness of the host beam, a, the thickness of the viscoelastic dissipative layer, e, the thickness of the restraining aluminium layer, h, and the width of the cross section, b, are kept constant for all the composite beams considered and the numeric values are listed in table 9.6.

Table 9.6: Dimensions of the beams with partial CLD treatments.

Dimension	Value [mm]
l	250
a	2
e	0.250
h	0.250
b	15

For finite element model application, the beams are divided in 50 elements of 5 mm each. In order to apply the method on composite structures with partial damping treatments, the spatial *Layerwise* formulation needs to be modified. As such, the FEM code is changed in order to allow the attribution of a different number of degrees of freedom to each element according to the number of layers of the element.

The applied load is assumed to be a unitary rectangular pulse with $t_c = 1$ s, as the one evidenced in figure 9.6. The time increment considered on the sampling of the load is $\Delta t = 0.001$ s.

In order to quantitatively compare the treatment's efficiency, the forced response of the composite beam is evaluated and the logarithmic decrement, δ, is determined. The logarithmic decrement is determined using the amplitude values of the transient response within the time bandwidth of the transient application, δ_l, and also using the amplitude values on the free

response time bandwidth, δ_f.

For the δ_l, the maximum values of amplitude of the response located in a time bandwidth of [0 0.5] s are gathered. In order to calculate the logarithmic decrement, the values of amplitude must be relative to the static displacement, as evidenced in figure 9.24.

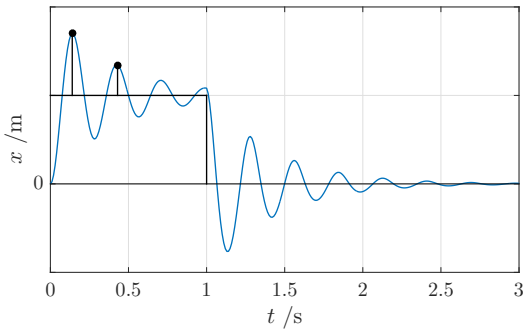

Figure 9.24: Maximum amplitude values of the response of the composite beam within the transient duration.

For the δ_f, the maximum values of the amplitude of the transient response located in a time bandwidth of [1 2] s are gathered, as evidenced in figure 9.25.

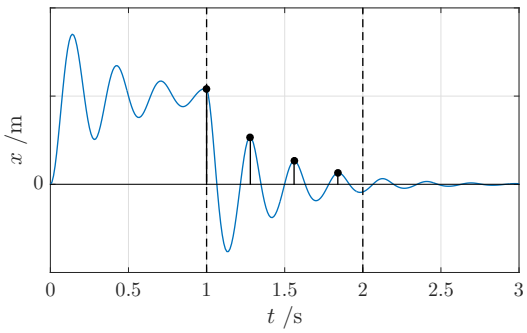

Figure 9.25: Maximum amplitude values of the free response of the composite beam.

The semi-logarithmic representation of such values as a function of the number of periods is linear. The approximation of such values to a linear function by means of a least square method allows to determine the logarithmic decrements, δ_l and δ_f, which correspond to the symmetric value of the slopes of the approximated linear functions. The logarithmic decrement is then used as an indicator of the damping level of the system, in the sense that higher values of δ imply a greater damping capacity.

9.6.1 Location of the partial treatment

With the intention of understanding the effects of the location of the partial damping treatment on the transient response of a clamped-free bending beam, three different situations are considered - figure 9.26. The length of the treatment is kept constant and corresponds to $l_t = 125$ mm.

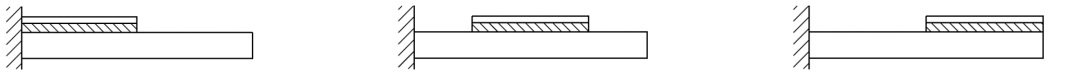

(a) Partial treatment at the root end of the beam.

(b) Partial treatment at the center of the beam.

(c) Partial treatment at the free end of the beam.

Figure 9.26: Composite beams with partial damping treatments on different locations.

For the configuration shown in figure 9.26a, the number of sampling points considered for sampling the rectangular pulse corresponds to $N = 2^{13}$.

The response spectrum of the free end of the beam can be seen in figure 9.27 for the entire frequency bandwidth. The highest value occurs at a null frequency and corresponds to the static displacement due to the application of a rectangular load. The secondary maximum values that can be identifiable in the graph correspond to the natural frequencies of the composite beam. In figure 9.27, the first natural frequency of the beam is visible and corresponds to 191.0039 rad.s^{-1}.

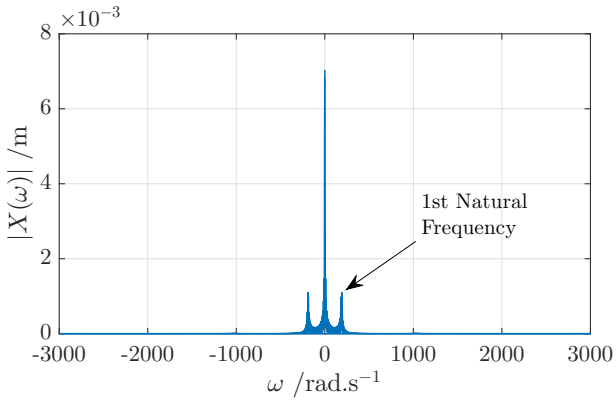

Figure 9.27: Response spectrum of a composite beam with a partial CLD treatment placed at the root end of the beam.

The transient response of the composite beam with a partial treatment placed at the root end is depicted in figure 9.28.

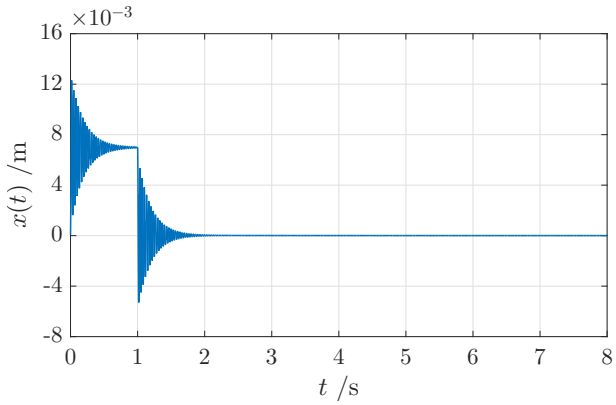

Figure 9.28: Transient response of a composite beam with a partial CLD treatment placed at the root end of the beam.

Comparing the attained response with the one relative to the beam with the complete damping treatment, which is evidenced in figure 9.12 of the previous section, it is noticeable that the

partial treatment is more efficient than the one where the viscoelastic layer is applied on the entire length of the beam. The logarithmic decrements calculated for the partial damping treatment correspond to $\delta_l = 0.1736$ and $\delta_f = 0.1602$ while the ones of a full length treatment are $\delta_l = 0.0803$ and $\delta_f = 0.0823$. The increase of efficiency is a consequence of the mass and stiffness reduction when the partial damping treatment is considered, but also, on the specific placement of the treatment. Since the shear deformation of the viscoelastic layer is a result of the bending deformation of the host and restraining layers, the energy dissipation is superior when the bending deformation is increased. For the particular case of a clamped-free composite beam, the maximum deformation is located at the root end and is null at the opposite end. Therefore, the portion of the treatment that corresponds to the second half of the bending beam does not induce a considerable energy dissipation when compared to the one closer to the root end. As such, it can be settled that such portion of the beam merely alters the deformation field and does not increase the damping properties.

For the configuration shown in figure 9.26b, the resulting transient response is shown in figure 9.29. The number of sampling points used is $N = 2^{13}$. The fundamental natural frequency, identifiable from the displacement phasor, corresponds to 147.3603 rad.s^{-1}.

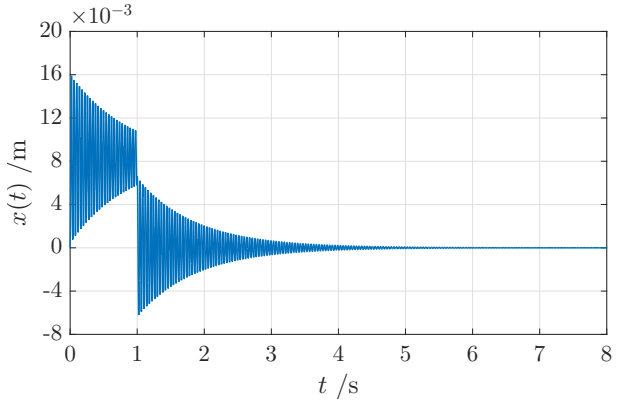

Figure 9.29: Transient response of a composite beam with a partial CLD treatment placed at the center of the beam.

The determined logarithmic decrements correspond to $\delta_l = 0.0452$ and $\delta_f = 0.0461$. Analysing the responses attained for both composite beams aforementioned and the determined values of the logarithmic decrements, it is understandable that placing the partial damping treatment at the root end of the beam represents the most efficient alternative. Such is, as previously referred, a consequence of the fact that the deformation is maximum at the root end and therefore induces the maximum deformation on the viscoelastic layer.

The transient response resultant of the application of a unitary rectangular pulse considering a partial damping treatment configuration as shown in figure 9.26c, is evidenced in figure 9.30. In order to completely dissipate the energy in the time bandwidth evaluated, 2^{16} sampling points are required. The first natural frequency of the composite beam is 158.7864 rad.s^{-1}.

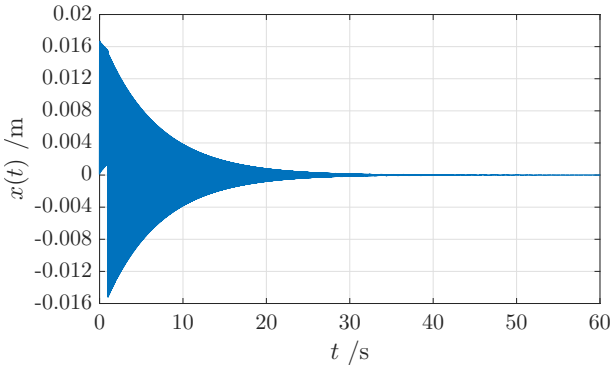

Figure 9.30: Transient response of a composite beam with a partial CLD treatment placed at the end of the beam.

As expected, the least efficient placement of the damping treatment is the one illustrated in figure 9.26c as it is placed in the portion of the beam where the deformation is negligible. Such conclusion is reinforced with the determination of the logarithmic decrement in the load phase and in the free vibration phase, that assume a value of $\delta_l = 0.0068$ and $\delta_f = 0.0067$, which is considerably inferior to the ones previously mentioned.

In table 9.7 are summarised the values of natural frequency and logarithmic decrements present in the current section as well as the addition of mass resultant of the application of the different partial treatments considered.

Table 9.7: Summary of the results attained for the partial damping treatments on different locations.

Configuration	Added Mass[a] [g]		Natural Frequency	δ_l	δ_f
	Viscoelastic Layer	Restraining Layer	[rad.s^{-1}]		
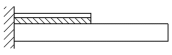	0.5344	1.1911	191.0039	0.1736	0.1602
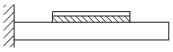	0.5344	1.1911	147.3603	0.0452	0.0461
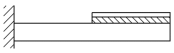	0.5344	1.1911	158.7864	0.0068	0.0067
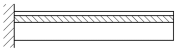	1.0688	2.3821	184.8673	0.0803	0.0823

[a] The mass of the host beam corresponds to 19.0575 g.

9.6.2 Length of the partial treatment

In order to evaluate the effects of the length of the partial damping treatment, l_t, three different configurations are evaluated. The schematic representation of such beams are shown in figure 9.31.

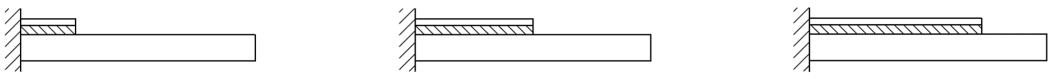

(a) $l_t = 50$ mm (b) $l_t = 125$ mm (c) $l_t = 190$ mm

Figure 9.31: Composite beams with partial damping treatments with different lengths.

The transient response of the beam illustrated in figure 9.31a, obtained using $N = 2^{13}$ sampling points is shown in figure 9.32. The first natural frequency corresponds to 166.4572 rad.s^{-1}.

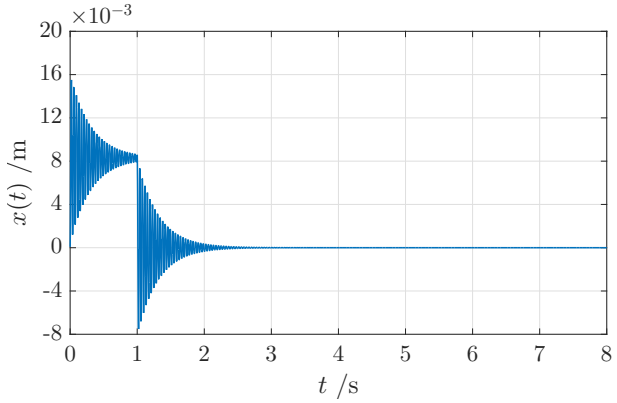

Figure 9.32: Transient response of a composite beam with a partial CLD treatment with l_t = 50 mm.

The transient response of a composite beam with the application of a viscoelastic and restraining layers of $l_t = 125$ mm of length is present in figure 9.28 of the previous section.

From the comparison of the responses obtained for both lengths considered, it is noticeable an increase of efficiency of the damping treatment when the length of the treatment changes from 50 mm to 125 mm. That result is confirmed with the calculation of the logarithmic decrements: for the configuration of figure 9.31a they take values of $\delta_l = 0.1201$ and $\delta_f = 0.1203$, while for the configuration of figure 9.31b correspond to $\delta_l = 0.1736$ and $\delta_f = 0.1602$. It is also visible that the increase of the length of the partial treatment conducts to an increase of the natural frequency of the composite beam.

Considering the beam portrayed in figure 9.31c and evaluating the method with, also, 2^{13} sampling points, the response is as evidenced in figure 9.33. The determined natural frequency corresponds to 191.7710 rad.s^{-1}.

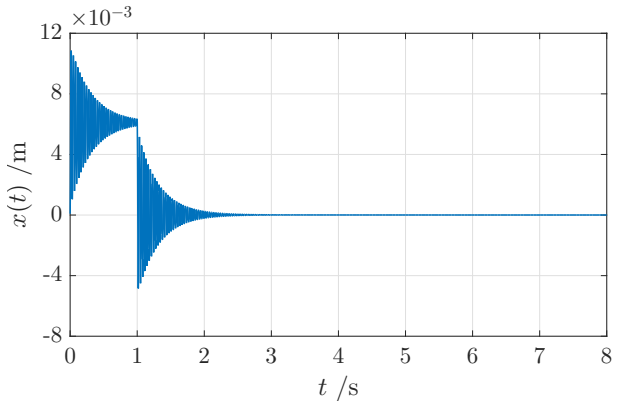

Figure 9.33: Transient response of a composite beam with a partial CLD treatment with l_t = 190 mm.

The logarithmic decrements determined from the evaluation of the response present in figure 9.33 correspond to $\delta_l = 0.1175$ and $\delta_f = 0.1026$. Analysing the three responses attained and the corresponding logarithmic decrements, is visible that the most efficient treatment is the one where half the length of the beam is covered with a viscoelastic layer. However, the three partial treatments considered in the current section lead to a superior damping capacity than

the one induced by a full length treatment. Such is a result of the negligible shear deformation of the viscoelastic material at the free end of the beam and also on the unfavorable change of the deformation field induced by the increase of mass and stiffness of the system. The first natural frequency showed a growing tendency when the length of the treatment is increased, thus the effect of the increase in the equivalent stiffness of the system due the restraining layer is higher than the effect of the increase in the mass of the system.

A summary of the results reached in the current section for the different partial treatments considered is present in table 9.8.

Table 9.8: Summary of the results attained for the partial damping treatments with different lengths.

Configuration	Added Mass[a] [g]		Natural Frequency	δ_l	δ_f
	Viscoelastic Layer	Restraining Layer	[rad.s^{-1}]		
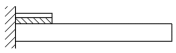	0.2138	0.4764	166.4572	0.1201	0.1203
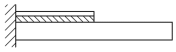	0.5344	1.1911	191.0039	0.1736	0.1602
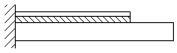	0.8123	1.8105	191.7710	0.1175	0.1026
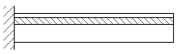	1.0688	2.3821	184.8673	0.0803	0.0823

[a] The mass of the host beam corresponds to 19.0575 g.

9.6.3 Discontinuous damping treatments

In the current section, two unconventional damping treatments are tested. These treatments consist on a discontinuous application of the viscoelastic layer with a discontinuous restraining layer or with a continuous restraining layer, as depicted in figure 9.34a and figure 9.34b. The thicknesses of the host, viscoelastic and restraining layers are the ones considered in the preceding sections and the dimensions of l_1 and l_2 of figure 9.34c are 30 mm and 55 mm, respectively.

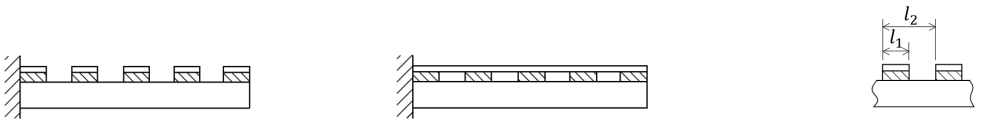

(a) Discontinuous restraining layer.

(b) Continuous restraining layer.

(c) Geometry of the treatment.

Figure 9.34: Composite beams with discontinuous damping treatments.

Analysing the treatment with a discontinuous restraining layer - figure 9.34a - and evaluating the method with 2^{13} sampling points, the resulting transient response is as shown in figure 9.35. The identified first natural frequency corresponds to 152.6497 rad.s^{-1}.

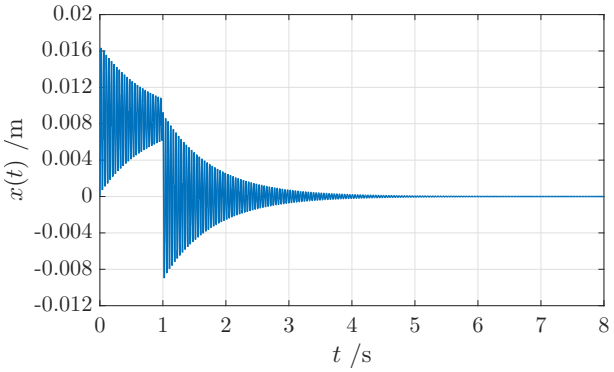

Figure 9.35: Transient response of a composite beam with a discontinuous viscoelastic and restraining layers.

Comparing the response of figure 9.35 with the one where a full length treatment is applied, it is noticeable a decrease of efficiency of the treatment, as the response is less damped in each cycle of vibration. Which is confirmed by the values of the logarithmic decrements, that are $\delta_l = 0.0803$ and $\delta_f = 0.0823$ for the full length treatment as opposed to $\delta_l = 0.0526$ and $\delta_f = 0.0527$ for the discontinuous treatment.

The introduction of a continuous restraining layer, as shown in figure 9.34b, leads to the response of figure 9.36.

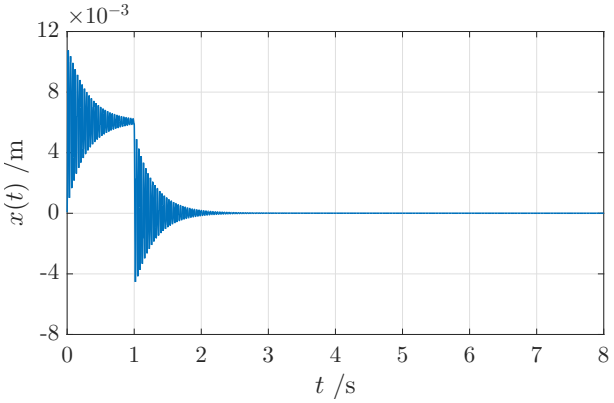

Figure 9.36: Transient response of a composite beam with a discontinuous viscoelastic layer and a continuous restraining layer.

The natural frequency of such composite beam corresponds to 179.4977 rad.s^{-1}, superior to the one where a discontinuous restraining layer is applied.

It is visible that the use of a complete restraining layer, where the coupling terms of the two metallic layers are not null, results in a greater damping capacity when compared to a treatment where a discontinuous restraining layer is applied. In fact, the discontinuous treatment with a continuous restraining layer conducts to greater damping capacity than the one where a full length viscoelastic layer is applied. Such result is confirmed with the calculation of the logarithmic decrements, that take values of $\delta_l = 0.1181$ and $\delta_f = 0.1175$.

In table 9.9 are listed the results attained in the current section.

Table 9.9: Summary of the results attained for the discontinuous damping treatments.

Configuration	Added Mass[a] [g]		Natural Frequency	δ_l	δ_f
	Viscoelastic Layer	Restraining Layer	[rad.s^{-1}]		
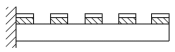	0.6413	1.4293	152.6497	0.0526	0.0527
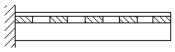	0.6413	2.3821	179.4977	0.1181	0.1175
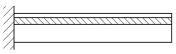	1.0688	2.3821	184.8673	0.0803	0.0823

[a] The mass of the host beam corresponds to 19.0575 g.

9.7 Conclusions

The implemented approach proves to be an effective method for the determination of the transient response of damped systems. The impulsive load can be modelled according to different mathematical expressions in order to more accurately reproduce an experimentally induced impact.

The analysis of the transient responses shows that using a fractional derivative model to express the frequency dependence of the viscoelastic material conducted to causal responses, whose displacement in $t = 0$ s is zero.

The time increment selected is a result of experiment, given that the vibration period of the resulting function is unknown. The number of sampling points is, however, selected in order to obtain a time domain in which the response of the system is completely extinguished. Thus, for the case of FLD treatments, a wide number of points is necessary and the computational time is excessive. As such, when a limiting number of simulations points is settled, for example, when the time domain load is determined experimentally and the number of points of the measuring device is narrow, CLD and ILD treatments represent the best testing option.

The transient responses attained are coherent since it confirmed that constrained layer damping treatments induce a greater energy dissipation as a consequence of the shear deformation of the viscoelastic material. Also, that increasing the thickness of the viscoelastic layer causes a greater damping capacity of the treatment.

Regarding the application of the method using composite beams with partial treatments, it is verified that the application of such treatments on the root end of the beam conducted to more efficient damping capacities than the ones attained using a full length treatment. From the options tested, the one of most efficiency is the one where 50% of the length of the beam is covered. Additionally, it is verified that the application of a treatment with a discontinuous viscoelastic layer and a continuous restraining layer leads to results similar to the ones where the viscoelastic layer is complete.

Chapter 10

Conclusion

10.1 Conclusions

It is widely acknowledged that an efficient mean of reducing sound and vibration of structures is through the application of damping treatments. Necessarily, the efficiency of such treatments immensely depends on the damping capacity of the viscoelastic material applied. Thereby, the determination of its properties represents an important step in the design of viscoelastic treatments.

Accordingly to the objectives proposed, the frequency and temperature dependence of such materials were thoroughly studied even though in the development of the current work isothermal conditions were assumed. The identification of the dynamic properties of a viscoelastic material was carried out using two distinct methods. Both methods were based on a curve-fitting process where the fractional derivative model of four parameters was used to characterise the frequency dependence of the complex modulus of the material.

Since the viscoelastic material exhibits, as stated previously, a great frequency dependence, most constitutive models and dynamic analysis are executed in the frequency domain. Consequently, the time domain response of composite systems with viscoelastic treatments corresponds to a minority of the research on the subject. For that reason, the transient response was determined using a frequency domain analysis and a discrete Fourier Transform (FFT algorithm) to build the time domain response from the frequency domain spectrum.

Identification of the Frequency Dependent Properties

To determine the complex modulus of the viscoelastic material 3M ISD112 as a function of frequency, several composite beams of different lengths were tested. The response was measured in the free end of the beam and the impact load applied to different points. The experimental procedure and set-up developed accurately reproduce the analytical model idealised of a beam with clamped-free boundary conditions and, thereby, consistent FRFs were attained.

In order to identify the fractional derivative model parameters, two identification methods were developed and validated: a two-step method where the FRFs were generated using the modal superposition principle and the other one based on a direct frequency analysis (DFA) for a set of control frequencies.

The two-step identification method proved to be a computationally complex method, where an iterative solution of several eigenproblems is required in order to determine the natural frequencies and eigenvectors of the composite beam whose stiffness matrix is frequency dependent. The division of the method in two steps demonstrated to be of considerable importance as the first step, where only the natural frequencies of both functions are aligned, conducts to values

close to the optimal solution. The second step, which is the most cumbersome step computationally, requires, consequently, a small number of iterations to adjust the amplitudes. The method becomes more efficient, as expected, when a smaller number of parameters are used, as were the case of the bare aluminium beams tested.

The minimisation process was implemented using different functions available in `Matlab`®, which led to the conclusion that evaluating the two steps of the method using gradient-based minimisation functions returns unimpressive results as the equation of the fractional derivative model shows distinct sensitivity for each of the parameters. It is then evidenced that using *fmincon* for the first step and *patternsearch* for the second step conducted to satisfactory results for a reasonable computational time.

A study on the performance of the method was carried out when different sets of parameters were tested and different modes of vibration were considered. A careful selection of the initial parameters must be carried out as the results proved to be quite dependent on the estimation provided. It is declared that increasing the number of modes considered, and therefore increasing the dimension of the problem, does not conduct to improved results. Hence, considering only the lowest order natural mode represents the best option in terms of both storage and quality of the results.

The properties reached using this method were not coincident for all the beams tested and discrepancies are significant for the loss and storage modulus. However, it can be considered that the methodology implemented is validated as good correlation was reached even if for some FRFs tested, the minimisation function failed on finding the global minimum.

The direct frequency response method, as opposed to the two-step identification method, is considerably simpler in terms of the number of function evaluations and mathematical operations computed. For each iteration considered, it only requires the solution of a number of system of equations equal to the number of control frequencies. However, the use of an unconstrained minimisation function makes the method quite susceptible to physically incoherent results: negative values for the parameters or even the non-satisfaction of the thermodynamic constraints.

The method proved to be very efficient when only three control frequencies located in a single mode of vibration are considered. Among these frequencies are the resonance frequency and the ones correspondent to the maximum and minimum values of the imaginary part of the FRF. The identified properties proved to be less disperse than the ones determined with the previous method, nonetheless, small variations are still present which inevitably hinders the selection of the final properties of the material.

Bearing in mind the evaluation of both methods comparatively, a few subjects should be noted. Even though the two-step identification method is more expensive computationally, it provides important information on the natural modes of the system: the natural frequencies, natural shapes and the modal loss factor are identified, whereas such information is not attained when a direct frequency analysis is performed. It is concluded that the two-step identification method responds more efficiently to the presence of experimental noise since the second step is performed using an integral minimisation function, whereas the DFA method requires that the control frequencies are selected using representative and noise-free bandwidths of the experimental FRFs.

Nonetheless, the consistency of the results attained using the direct frequency response method is significantly superior and the iteration time is considerably inferior.

The properties reached were not coincident for both methods implemented. Significant differences were attained for both storage modulus and loss factor. However, the resultant tendency of both properties to frequency variations is the same for both methods.

Transient Response Analysis

A methodology for the determination of the transient response of structures with viscoelastic materials with frequency dependent properties was implemented and validated. The validation of such methodology was performed considering a viscously damped single degree of freedom system with constant properties submitted to a transient load. The result was compared to the one attained using Duhamel's integral formulation. It was verified that the results from the developed methodology were coincident for the damped system, whereas, for the undamped model the responses diverged noticeably. That is a result of the discontinuity present in the frequency response spectrum for an undamped system located on the natural frequency, where the displacement phasor tends to infinity.

As for the implementation of the Fourier transform, a few concerns must be taken into account. An accurate time resolution must be selected so that the reconstructed signal is coherent. The selection of an appropriate time increment must be performed through trial and error as the period of the resultant function is unknown. When recurring to the FFT algorithm present in `Matlab`®, one needs to take into consideration the scaling of the resultant function if the order of magnitude of the resultant spectrum is of interest.

The application of the method on composite structures with viscoelastic layers led to coherent results. The transient response of the system is oscillatory and damped. Different load configurations were tested in order to approximate the analytical transient to one that could be experimentally reproduced and the results were satisfactory.

Viscoelastic Damping Treatments

The efficiency of the viscoelastic damping treatments can be estimated from the analysis of the transient response of the system. Free Layer Damping (FLD) treatments induce in the system a smaller energy dissipation and require higher thicknesses of the viscoelastic layer to conduct to considerable damping levels. In contrast, the application of a Constrained Layer Damping (CLD) treatment configuration induces a considerable change in the transient response of the system. The decay of amplitude is greater for smaller thicknesses of the viscoelastic layer and therefore a higher efficiency is attained. As expected, for Integrated Layer Damping (ILD) treatments, the transient response is still oscillatory but evidences an energy dissipation in each cycle of oscillation superior to both treatments previously referred. Such result is due to the placement of the viscoelastic layer in the neutral plane of bending, that is, the plane where the shear deformation reaches its maximum value.

To evaluate the efficiency of structures with partial damping treatments, the finite element model was changed in order to allow the attribution of different number of degrees of freedom to each element according to the number of layers. Additionally, the logarithmic decrement of the transient response during the load application and the logarithmic decrement of the free response was used as an indicator of the treatment's damping efficiency.

The analysis of the transient response of composite beams with partial damping treatments as well as the logarithmic decrements allows to conclude that such treatments can lead to a greater energy dissipation than the ones where the entire beam in covered with the viscoelastic material. For a clamped-free bending beam, the application of a partial treatment at the clamped end of the beam conducts to the most efficient damping capacity, as it is where the bending deformation of the beam is higher. As such, it is concluded, that the knowledge of the deformation field of the structure is of great importance for the correct application of the dissipative layer. The application of discontinuous viscoelastic treatments leads to considerable energy dissipation if the restraining elastic layer applied is continuous. That is, the coupling terms between the host structure and restraining layers are preserved.

10.2 Future Work

In order to complement and improve the study hereby developed a few suggestions are proposed:

Identification Methods

- Analysis of both methods using transmissibility functions as opposed to receptances;
- Determination of the storage modulus and loss factor for different temperatures in order to construct the reduced frequency nomogram of the material;
- Development of a minimisation function that allows the introduction of analytical gradients and parameter sensitivity in order to more reliably determine the global minimum of the function.

Transient Response Analysis

- Development of an experimental procedure in order to determine the transient response of composite structures with viscoelastic materials, saving the data relative to the various transient impulses applied;
- Application of the current method using the experimental attained transient impulses. Since the transient response requires the averaging of several impulses, such data should be adjusted to a single analytical function using a curve-fitting process;
- Perform a comparison of the transient responses attained from the implemented method with the ones resultant of the application of ADF and GHM models;
- Extension of the transient analysis to plate and shell structures.

Viscoelastic Damping Treatments

- Application of the method on structures with partial damping treatments and different boundary conditions;
- Evaluation of the efficiency of the treatment as a function of the covered length of the beam for viscoelastic materials with different values of stiffness;
- Comparison of the results attained using partial damping treatments with ones gathered experimentally;
- Study of the effects of damping a single mode of vibration on the transient response of a composite beam.

Appendix A

Measured Frequency Response Functions

A.1 Bare Beam Results

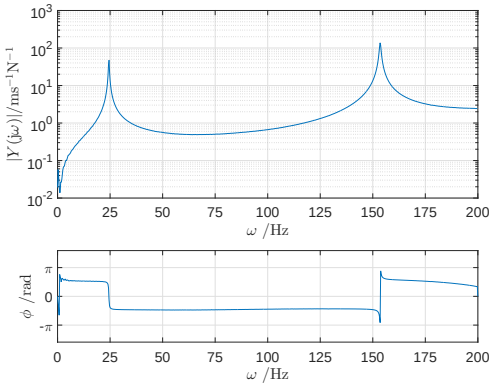

Figure A.1: Mobility measured in the free end of the base beam with excitation in point $x = 44$ mm ($T \approx 18°\mathrm{C}$).

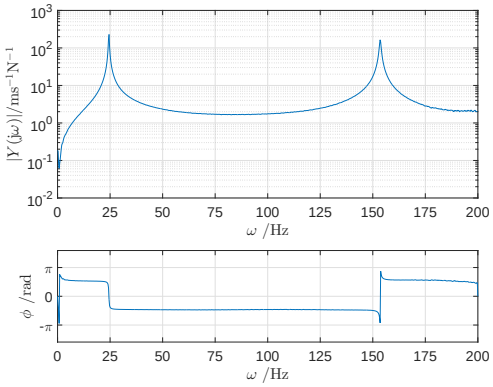

Figure A.2: Mobility measured in the free end of the base beam with excitation in point $x = 108$ mm ($T \approx 18°\mathrm{C}$).

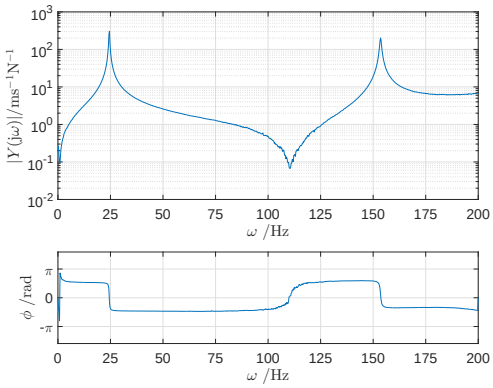

Figure A.3: Mobility of the base beam with excitation and response on the free end of the beam ($T \approx 18°C$).

A.2 Sandwich Beam Results

A.2.1 Beam A

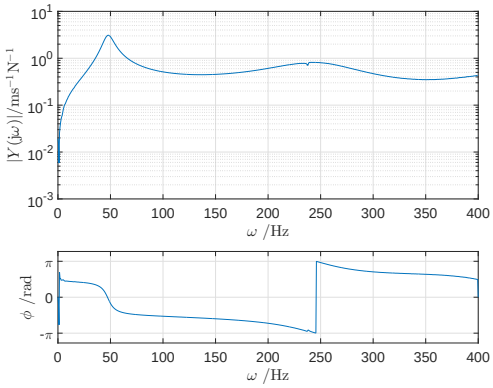

Figure A.4: Mobility measured in the free end of the beam with excitation in the point $x = 80$ mm ($T \approx 18°C$).

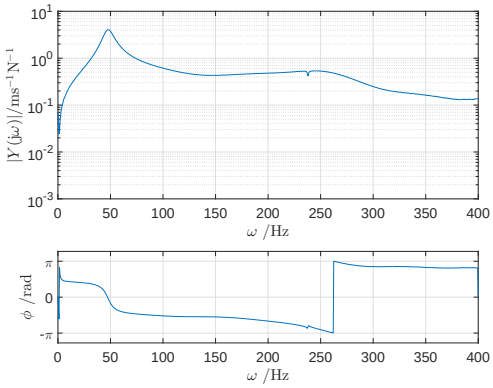

Figure A.5: Mobility measured in the free end of the beam with excitation in the point $x = 108$ mm ($T \approx 18°C$).

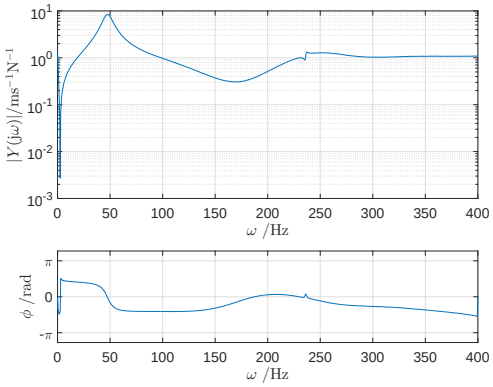

Figure A.6: Mobility measured in the free end of the beam with excitation in the point $x = 180$ mm ($T \approx 14°C$).

A.2.2 Beam B

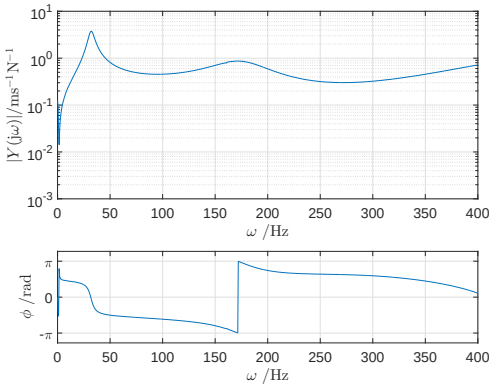

Figure A.7: Mobility measured in the free end of the beam with excitation in the point $x = 88$ mm ($T \approx 16°C$).

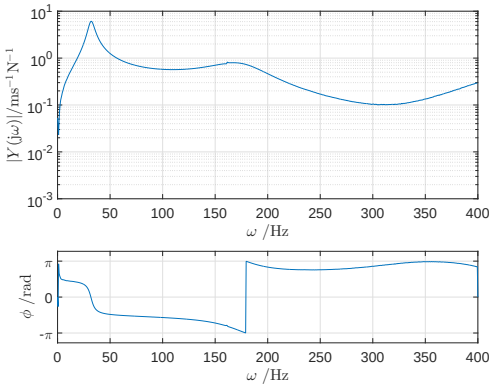

Figure A.8: Mobility measured in the free end of the beam with excitation in the point $x = 128$ mm ($T \approx 16°C$).

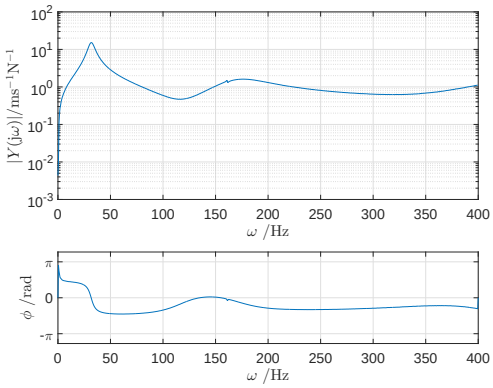

Figure A.9: Mobility measured in the free end of the beam with excitation in the point $x = 220$ mm ($T \approx 21°C$).

A.2.3 Beam C

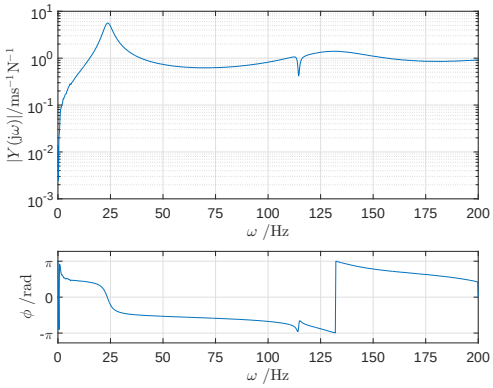

Figure A.10: Mobility measured in the free end of the beam with excitation in the point $x = 108$ mm ($T \approx 15°C$).

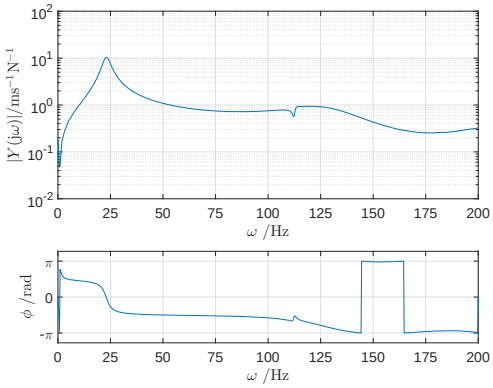

Figure A.11: Mobility measured in the free end of the beam with excitation in the point $x = 172$ mm ($T \approx 18°C$).

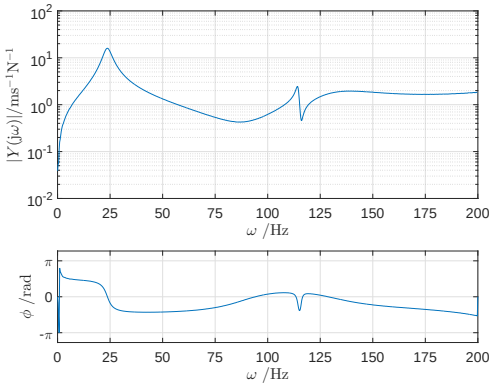

Figure A.12: Mobility measured in the free end of the beam with excitation in the point $x = 260$ mm ($T \approx 15°$C).

Appendix B

Results obtained for the Composite Beams

B.1 1st Step: *fminsearch*, 2nd Step: *fmincon*

B.1.1 Composite Beam B

Table B.1: Identified parameters using minimisation functions *fminsearch* and *fmincon* for the first and second steps, respectively.

FRF	Parameter		First Step	Second Step
$FRF_{220,88}$	E_0	/Pa	1.4691×10^{6}	1.4691×10^{6}
	E_∞	/Pa	5.0921×10^{8}	5.0921×10^{8}
	τ	/s	1.0630×10^{-6}	1.0630×10^{-6}
	α		5.8349×10^{-1}	5.8349×10^{-1}
$FRF_{220,128}$	E_0	/Pa	1.8986×10^{6}	1.8986×10^{6}
	E_∞	/Pa	1.4582×10^{8}	1.4582×10^{8}
	τ	/s	3.6458×10^{-6}	4.7906×10^{-6}
	α		5.3216×10^{-1}	5.3209×10^{-1}
$FRF_{220,220}$	E_0	/Pa	8.9972×10^{5}	8.9972×10^{5}
	E_∞	/Pa	8.9815×10^{8}	8.9815×10^{8}
	τ	/s	9.9409×10^{-7}	6.9708×10^{-9}
	α		6.1197×10^{-1}	4.3218×10^{-1}

B.1.2 Composite Beam C

Table B.2: Identified parameters using minimisation functions *fminsearch* and *fmincon* for the first and second steps, respectively.

FRF	Parameter		First Step	Second Step
$FRF_{260,108}$	E_0	/Pa	1.5546×10^{6}	1.5546×10^{6}
	E_∞	/Pa	2.9803×10^{8}	2.9803×10^{8}
	τ	/s	7.8718×10^{-7}	5.1718×10^{-7}
	α		4.7218×10^{-1}	4.7305×10^{-1}
$FRF_{260,172}$	E_0	/Pa	1.9435×10^{6}	1.9435×10^{6}
	E_∞	/Pa	1.2914×10^{9}	1.2914×10^{9}
	τ	/s	5.4647×10^{-6}	5.9795×10^{-6}
	α		6.9415×10^{-1}	6.9369×10^{-1}
$FRF_{260,260}$	E_0	/Pa	4.2428×10^{6}	4.2428×10^{8}
	E_∞	/Pa	2.3971×10^{9}	2.3971×10^{9}
	τ	/s	4.1596×10^{-9}	8.3192×10^{-9}
	α		5.8247×10^{-1}	4.9133×10^{-1}

References

3M (2012, October). *Technical Data: $3M^{TM}$ Viscoelastic Damping Polymers* $112 - \bullet 113-$.

Amorim, J. (2013, July). Vibroacoustic analysis of plates with viscoelastic damping patches: A layerwise theory and the rayleigh-ritz method. Master's thesis, Faculdade de Engenharia da Universidade do Porto.

ASTM (2010, March). *E756-05: Standard Test Method for Measuring Vibration-Damping Properties of Materials*.

Audet, C. and J. E. Dennis Jr (2006). Mesh adaptive direct search algorithms for constrained optimization. *SIAM Journal on optimization 17*(1), 188–217.

Bagley, R. L. and P. J. Torvik (1986). On the fractional calculus model of viscoelastic behavior. *Journal of Rheology 30*(1), 133–155.

Barkanov, E. (1999). Transient response analysis of structures made from viscoelastic materials. *International journal for numerical methods in engineering 44*(3), 393–403.

Barkanov, E., R. Rikards, C. Holste, and O. Täger (2000). Transient response of sandwich viscoelastic beams, plates and shells under impulse loading. *Mechanics of Composite Materials 36*(3), 215–222.

Bracewell, R. (2000). *The Fourier Transform and Its Applications*. Electrical Engineering Series. McGraw Hill.

Byrd, R. H., M. E. Hribar, and J. Nocedal (1999). An interior point algorithm for large-scale nonlinear programming. *SIAM Journal on Optimization 9*(4), 877–900.

Fernandes, M. (2013, February). Identificação bietápica dos parâmetros do modelo constitutivo de derivadas fracionárias de materiais viscoelásticos. Master's thesis, Faculdade de Engenharia da Universidade do Porto.

Granger, D. and A. Ross (2009). Effects of partial constrained viscoelastic layer damping parameters on the initial transient response of impacted cantilever beams: Experimental and numerical results. *Journal of Sound and Vibration 321*(1), 45 – 64.

Gutierrez-Lemini, D. (2013). *Engineering Viscoelasticity*. SpringerLink : Bücher. Springer.

Hover, F. and H. Chin (2009). *2.017J Design of Electromechanical Robotic Systems*. Massachusetts Institute of Technology.

Johnson, C. D. (1995). Design of passive damping systems. *Transactions - American Society of Mechanical Engineers Journal of Mechanical Design 117*, 171–171.

Jones, D. (2001). *Handbook of Viscoelastic Vibration Damping*. John Wiley & Sons.

Khalfi, B. and A. Ross (2013). Transient response of a plate with partial constrained viscoelastic layer damping. *International Journal of Mechanical Sciences 68*, 304 – 312.

Kim, S. Y. and D. H. Lee (2009). Identification of fractional-derivative-model parameters of viscoelastic materials from measured frfs. *Journal of Sound and Vibration 324*(3), 570–586.

Lagarias, J. C., J. A. Reeds, M. H. Wright, and P. E. Wright (1998). Convergence properties of the nelder–mead simplex method in low dimensions. *SIAM Journal on Optimization 9*(1), 112–147.

Liao, Y. and V. Wells (2008). Estimation of complex young's modulus of non-stiff materials using a modified oberst beam technique. *Journal of Sound and Vibration 316*(1–5), 87 – 100.

Lopes, J. (2008, March). Modeling the dynamic behaviour of laminate structures with cork compounds. Master's thesis, Faculdade de Engenharia da Universidade do Porto.

Martinez-Agirre, M. and M. J. Elejabarrieta (2011). Dynamic characterization of high damping viscoelastic materials from vibration test data. *Journal of Sound and Vibration 330*(16), 3930 – 3943.

Moreira, R. (2004, Novembro). *Modelação e análise de Tratamentos Viscoelásticos Multi-camada para Controlo Passivo de Vibrações*. Ph. D. thesis, Faculdade de Engenharia da Universidade do Porto.

Moreira, R., J. Corte Real, and J. Rodrigues (2010). A generalized frequency-temperature viscoelastic model. *Shock and Vibration 17*, 407–418.

Moreira, R. A. S., J. D. Rodrigues, and A. J. M. Ferreira (2005). A generalized layerwise finite element for multi-layer damping treatments. *Computational Mechanics 37*(5).

Oñate, E. (2013). *Structural Analysis with the Finite Element Method. Linear Statics: Volume 2: Beams, Plates and Shells*. Lecture Notes on Numerical Methods in Engineering and Sciences. Springer Netherlands.

Pritz, T. (1996). Analysis of four-paramrter fractional derivative model of real solid materials. *Journal of Sound and Vibration 195*(1), 103 – 115.

Randall, R. (1987). *Frequency Analysis*. Brüel & Kjaer.

Rao, M. D. (2003). Recent applications of viscoelastic damping for noise control in automobiles and commercial airplanes. *Journal of Sound and Vibration 262*(3), 457 – 474.

Reddy, J. (1996). *Mechanics of Laminated Composite Plates: Theory and Analysis*. CRC-Press.

Thrane, N. (1979). *The Discrete Fourier Transform and FFT Analyzers*. Number 1 in Technical Review. Brüel & Kjaer.

Vasques, C. and L. Cardoso (2011). Viscoelastic damping technologies: Finite element modeling and application to circular saw blades. *Vibration and Structural Acoustics Analysis: Current Research and Related Technologies*, 207–254.

Vasques, C., R. Moreira, and J. Rodrigues (2010a). Viscoelastic damping technologies - part I: Modeling and finite element implementation. *Journal of Advanced Research in Mechanical Engineering 1*, 76–95.

Vasques, C., R. Moreira, and J. Rodrigues (2010b). Viscoelastic damping technologies - part II: Experimental identification procedure and validation. *Journal of Advanced Research in Mechanical Engineering 1*, 96–110.

Wojtowicki, J.-L., L. Jaouen, and R. Panneton (2004). New approach for the measurement of damping properties of materials using the oberst beam. *Review of Scientific Instruments 75*(8), 2569–2574.

Zang, C., H. Grafe, and M. Imregun (2001). Frequency–domain criteria for correlating and updating dynamic finite element models. *Mechanical Systems and Signal Processing 15*(1), 139 – 155.